JOHANNES GUTENBERG UNIVERSITÄT MAINZ

Electricfield driven active colloids moving in complex and crowded media

written by

Venkata Manikantha Sai Ganesh Tanuku

(geb. in Vijayawada, India)

Mainz May 2026

This dissertation is submitted to the Faculty of Physics, Mathematics and Informatics of Johannes Gutenberg University Mainz for the degree of “Doctor of Natural Sciences”

Author's note:

This thesis was carried out from November 2020 to March 2025 in the Institute for Physics (Johannes Gutenberg University).

Supervisor: [redacted]

Co-Supervisor: [redacted]

Date of oral examination: 23.07.2026

Abstract

Active colloids have emerged as versatile model systems for exploring non-equilibrium physics and developing microscale transport technologies. While their behavior in simple Newtonian fluids is well understood, their dynamics in complex and crowded environments remain insufficiently explored due to challenges in controlling both propulsion and environmental conditions. In this thesis, a unified experimental framework is developed to investigate the motion of active Janus particles driven by alternating current (AC) electric fields. This approach enables independent and precise control over propulsion speed, direction, and interparticle interactions through externally tunable parameters such as field strength and frequency. Importantly, it allows simultaneous manipulation of both the active particles and their surrounding environment.

The study systematically explores three classes of tunable environments: viscous polymer solutions, electrohydrodynamically assembled cluster “islands” and dense polycrystalline colloidal monolayers. In polymeric media, the interplay between propulsion and viscosity leads to distinct dynamical regimes, including trapped, jittery, and directed motion. In structured island landscapes, particle obstacle interactions give rise to collision-induced reorientation and backscattering, resembling run and tumble dynamics. In crowded monolayers, externally controlled interactions enable tuning of the structural and mechanical properties of the environment, significantly affecting particle transport and persistence.

Beyond fundamental insights, the work demonstrates functional capabilities such as controlled cargo capture, transport, and release in complex media. By combining externally driven propulsion with programmable environments, this thesis establishes a versatile platform for studying active matter under realistic conditions and paves the way for applications in microrobotics, targeted delivery, and adaptive materials.

Zusammenfassung

Aktive Kolloide haben sich als vielseitige Modellsysteme zur Untersuchung nichtgleichgewichtiger Physik sowie zur Entwicklung von Transportprozessen im Mikromaßstab etabliert. Während ihr Verhalten in einfachen Newtonschen Flüssigkeiten gut verstanden ist, sind ihre Dynamiken in komplexen und dichten Umgebungen bislang nur unzureichend untersucht, insbesondere aufgrund der eingeschränkten Kontrollierbarkeit von Antrieb und Umgebung. In dieser Arbeit wird ein einheitlicher experimenteller Ansatz entwickelt, um die Bewegung aktiver Janus-Partikel zu untersuchen, die durch Wechselstromfelder (AC-Felder) angetrieben werden. Dieser Ansatz ermöglicht eine präzise und unabhängige Kontrolle von Geschwindigkeit, Bewegungsrichtung und Wechselwirkungen der Partikel über extern einstellbare Parameter wie Feldstärke und Frequenz. Gleichzeitig erlaubt er eine gezielte Beeinflussung sowohl der aktiven Partikel als auch ihrer Umgebung.

Es werden systematisch drei Arten von einstellbaren Umgebungen untersucht: viskose Polymerlösungen, elektrohydrodynamisch erzeugte Clusterstrukturen (Inseln) sowie dichte polykristalline kolloidale Monolagen. In polymeren Medien führt das Zusammenspiel von Antrieb und Viskosität zu unterschiedlichen Bewegungsregimen, darunter eingeschränkte, jitterartige und gerichtete Bewegung. In strukturierten Insel-Landschaften verursachen Kollisionen mit Hindernissen Umlenkungen und Rückstreueffekte, die Ähnlichkeiten mit dem Run and Tumble Verhalten biologischer Mikroschwimmer aufweisen. In dichten Monolagen ermöglichen feldgesteuerte Wechselwirkungen eine gezielte Anpassung der strukturellen und mechanischen Eigenschaften der Umgebung, wodurch die Partikeldynamik wesentlich beeinflusst wird und qualitativ verändert.

Neben grundlegenden Erkenntnissen zeigt diese Arbeit auch funktionale Anwendungen, wie den kontrollierten Transport, das Einfangen und die Freisetzung von Partikeln in komplexen Medien. Durch die Kombination von extern gesteuertem Antrieb und programmierbaren Umgebungen stellt diese Arbeit eine vielseitige Plattform zur Untersuchung aktiver Materie unter realistischen Bedingungen bereit und eröffnet Perspektiven für Anwendungen in der Mikrorobotik, gezielten Wirkstoffabgabe und die gezeigten experimentellen Beispiele eröffnen adaptiven Materialien.

Contents

Chapter 1 - **Introduction**

1.1 Motivation

Colloids are microscopic particles, typically on the micrometer scale, and play an important role in both industrial applications and everyday products. For research, a key advantage of colloidal systems is that their organization can be directly visualized at the single-particle level. In contrast to atoms and molecules, colloids are large enough to be observed by optical microscopy, while still being small enough to undergo Brownian motion. This makes them useful model systems for studying phenomena analogous to atomic systems, such as crystallization, melting and epitaxial growth, without relying only on ensemble averaged measurements [1,2,3].

Early studies mainly focused on colloidal particles with isotropic interactions. Later, the development of anisotropic colloids made it possible to investigate systems with directional interactions, where particle shape or surface chemistry can lead to new types of ordering [4,5]. Advances in synthesis techniques have enabled the large-scale production of particles with a wide range of shapes and material compositions, using methods such as electro-jetting [6], phase separation [7], mold imprinting [8], lithography [9], chemical synthesis [10], microfluidic approaches [11], and mechanical stretching [12].

As an important class of anisotropic colloids, Janus particles (JPs) have received increasing attention since their conceptual introduction by Nobel laureate de Gennes [13], who proposed particles with two contrasting faces and highlighted their potential applications [14,15,16]. These particles are characterized by two sides with different surface properties, such as regions carrying opposite electric charges [17,18] or domains with different affinities to the surrounding solvent, for example hydrophobic and hydrophilic hemispheres [19]. While the early idea was primarily related to thermal systems [20], later work established Janus particles as versatile colloidal systems for studying anisotropic interactions, directed assembly and active motion.

Janus colloids can be used in two different ways, as passive anisotropic particles or as active particles. The latter are commonly referred to as artificial microswimmers because they consume energy from their surroundings and convert it into autonomous propulsion and functionality. In particular, micrometer sized spherical Janus particles are useful model systems because their motion can be directly tracked and analyzed using optical microscopy [21]. Their

dynamics can often be described within the framework of active Brownian particles (ABPs) [22], which makes them well suited for connecting experiments with theoretical models.

Janus particles can be synthesized with good control over size, shape and surface properties, and they can be powered by different propulsion mechanisms. Early active Janus systems mostly relied on catalytic surface reactions [23,24,25,], or on laser illumination as an energy source, where the darker hemisphere is preferentially heated. In these systems, propulsion can arise from self-diffusiophoresis after photocatalysis [26,27,], local demixing of a carefully chosen solvent [28], or self-thermophoresis [29]. Magnetic materials can also be incorporated during fabrication, allowing particles to be oriented or guided by external magnetic fields [30,31,32]. More recently, metallodielectric Janus particles driven by AC electric fields have attracted attention as an alternative to catalytic or laser-driven systems [33,34]. Their main conceptual advantage is that the surrounding medium can remain chemically homogeneous during the experiment, rather than being locally heated or depleted of fuel. In addition, the propulsion force can be controlled externally and set to high values, limited mainly by electrode stability. The particle speed depends on the square of the electric-field strength, while the propulsion direction and mutual interactions can be tuned by the applied field frequency [35, 36, 37].

The presence of additives, such as polymer molecules, can modify the behavior of Janus particles, and the particles can in turn perturb their surrounding medium. Although polymer coils are much smaller than the active particles, they can strongly affect microswimmer motion and interactions even at moderate concentrations. For example, the swimming speed of catalytic Janus particles in dilute polymer solutions was found to decrease approximately with the inverse of the viscosity [38,39,]. In a systematic study using different viscosifiers from the dilute to the semidilute entangled regime, it was further shown that the bath rheology can also influence fuel supply, leading to additional slowing and, eventually, trapping of catalytic Janus particles [40]. Non-Newtonian media can affect biological swimmers in similarly nontrivial ways. For sperm cells and some bacteria, the swimming speed shows a non-monotonic dependence on solute concentration. Initially, this speed increase was attributed to the microporous structure of the medium, but later studies related it to local shear thinning caused by the action of the flagella [41,42,43,]. Such local modification of the surrounding fluid may also be relevant for strongly driven artificial microswimmers. Polymeric and viscoelastic media can also alter swimmer orientation dynamics. For flagellated swimmers, viscoelasticity was reported to reduce rotational diffusion [44]. In contrast, for Janus particles, an increase in

rotational diffusion and even a transition to helical swimming were observed and explained by a memory mechanism of the surrounding medium [45, 46, 47, 48,]. Finally, even dilute solutions of high-molecular-weight polyethylene oxide can strongly affect sedimented Janus particles: adsorption of the polymer to the silica side of the particles, and possibly to the substrate, was found to suppress ballistic motion and rotational fluctuations up to complete arrest [49].

Dense baths of passive colloids introduce a different form of complexity for Janus-particle motion. In such crowded environments, the bath structure can influence swimmer trajectories through collisions, excluded-volume interactions, caging, depletion wakes, or long-range interactions between active and passive particles [50, 51]. At the same time, the swimmers can actively modify the passive environment. By injecting energy into an otherwise equilibrium colloidal bath, self-propelled particles can change its microstructure. Their swimming force can locally compress the surrounding passive particles [52], rearrange particles in crystalline lattices [53] ,anneal defects and grain boundaries [54,55,56,], deform particle networks [57], and alter the velocity distribution of passive components [58].

The influence also works in the opposite direction. Passive particles can enhance motility-induced phase separation [59,60,], promote group formation [61, 62,], and induce long-range interactions between active particles [63,64,]. Moreover, a microstructured passive environment can strongly affect the rotational motion of self-propelled particles and therefore their persistence time. Recent experiments in colloidal glasses, for example, reported an enhancement of rotational diffusion by up to two orders of magnitude [65,66,].

In this thesis, I address these issues using AC electric-field-driven Janus particles. I first implement the required experimental platform, including optical observation, positional tracking, an ITO-based sample cell and reproducible Janus-particle synthesis. I then establish AC-driven Janus particles as a controllable model system, where propulsion speed, direction and particle interactions can be tuned externally through the applied field strength and frequency. I combine this swimmer system with three representative environments. First, I study motion in viscosified PEG solutions to test how polymer-induced resistance affects propulsion and persistence. Second, I investigate Janus-particle motion in dynamically assembled passive colloidal structures, where collisions and local crowding influence trajectories. Third, I use dense ordered colloidal backgrounds to examine how active particles move through structured environments and how the environment feeds back on their dynamics.

Together, these experiments are designed to clarify how viscosity, crowding, structure and active passive interactions control Janus particle motion and cargo transport (see Figure 1.1).

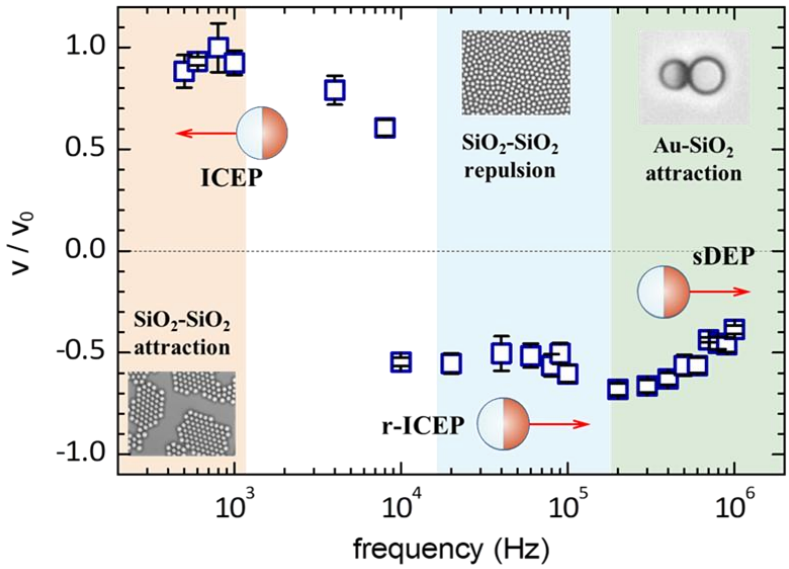

Figure 1.1, Overview of the AC electric-field controlled colloidal systems studied in this thesis. The applied frequency controls Janus-particle propulsion, passive silica–silica interactions, and active–passive coupling, enabling ICEP motion and island formation at low frequency, dipolar repulsion in passive monolayers at intermediate frequency, and sDEP-driven motion with Au–silica attraction at high frequency.

Overall, the experiments reported here are designed to establish AC electric-field-driven Janus particles as a controllable model system for studying active motion in realistic environments. By combining externally tunable propulsion with polymeric, crowded and structured surroundings, this thesis aims to enhance our understanding of how viscosity, local structure and active passive interactions shape microswimmers dynamics. In this way, the work provides a basis for designing active colloidal systems capable of controlled transport, interaction with targets and operation in complex environments.

1.2 Structure of thesis

This thesis proceeds from the development of a controllable experimental platform to its application in progressively more complex environments. After introducing the relevant background in Chapter 2 and the experimental methods in Chapter 3, Chapter 4 establishes AC electric field driven Janus particles as a reproducible and tunable model system. Chapters 5 and 6 investigate JPs motion and cargo transport in PEG polymer solutions, where the viscosity and polymer concentration of the surrounding medium are controlled. Chapter 7 extends the system to heterogeneous crowded environments by studying island hopping between passive colloidal

clusters. Finally, Chapter 8 explores JPs motion in polycrystalline colloidal landscapes, where local order provides structured constraints on active motion. Together, these chapters examine how external driving, polymeric resistance, crowding and passive structure control the dynamics and functionality of Janus particles.

Parts of this thesis were carried out in collaboration with external and internal collaborators. I performed the experimental work presented in this thesis, while selected simulations and rheological measurements were carried out in collaboration with the researchers specified below. Numerical simulations discussed in Chapter 8 were performed by Dr. Isha Malhotra and Dr. Lorenzo Caprini, who worked as postdoctoral researchers in the group of Prof. Dr. Hartmut Löwen at Heinrich-Heine-Universität Düsseldorf. These simulations are included to support and rationalize the experimental findings, while the main focus of the thesis remains on the experimental realization of steering AC field JPs in various crowded environments.

The development and interpretation of the active-colloid experiments were carried out in collaboration with Prof. Dr. Ivo Buttinoni at Heinrich-Heine-Universität Düsseldorf. The rheological characterization of the polymer suspensions was performed in collaboration with Prof. Dr. Regine von Klitzing and Ms. Atehi Razavi at Technische from Universität Darmstadt. Their contribution was essential for determining the rheological properties of the PEG solutions used in the experiments on Janus-particle motion and cargo transport in viscosified media.

Parts of this thesis are based on published and manuscripts in preparation:

1. **Venkata Manikantha Sai Ganesh, T.,** Vogel, P., Palberg, T., and Buttinoni, I. (2023). Island hopping of active colloids**.** *Soft Matter*, 19(29), 5452–5458.
2. **Venkata Manikantha Sai Ganesh, T.,** Malhotra, I., Caprini, L., Löwen, H., Palberg, T., and Buttinoni, I. (2026). Active particle in tunable compressible environments**.** Small Science,6, e202500599.

Two additional manuscripts are in the process of being drafted:

1. **Venkata Manikantha Sai Ganesh, T.,** Razavi, A., von Klitzing, R., and Palberg, T. (2026). AC field driven active colloids dynamics in polymer solutions. (In preparation)
2. **Venkata Manikantha Sai Ganesh, T.,** Razavi, A., Vogel, P., von Klitzing, R., and Palberg, T. (2026). Cargo delivery in viscosified media using AC electric-field driven Janus particles. (In preparation)

Chapter 2 - **Background**

2.1 Introduction

This chapter introduces the theoretical concepts required to understand the behavior of electric-field-driven active colloids in complex and crowded environments. The discussion begins with the basic properties of colloidal particles and the interactions that determine their stability in suspension. It then introduces electrostatic and van der Waals interactions, the electric double layer, and the DLVO framework. These concepts are followed by the phase behavior and dynamics of colloidal suspensions, including Brownian motion, hydrodynamics and diffusion. Finally, the chapter discusses colloids under external electric fields, phoretic transport mechanisms, active Janus particles and the influence of complex or crowded environments on active motion. Together, these concepts provide the physical basis for the experimental platform and results presented in the following chapters.

2.2 Colloidal Particles as Model Systems

The irregular motion of microscopic particles suspended in liquids was first systematically described by Robert Brown in 1827. By observing pollen grains and later inanimate particles such as coal dust, Brown showed that this motion is not related to biological activity, but is a general physical phenomenon. This erratic motion, now known as Brownian motion, originates from thermal fluctuations of the surrounding solvent molecules and is one of the most direct manifestations of microscopic molecular motion.

Colloidal particles provide an experimentally accessible model system for studying such thermal fluctuations. Although they are much larger than atoms or molecules, typically ranging from nanometers to micrometers, they are still strongly affected by thermal energy. At the same time, their size allows them to be directly observed by optical microscopy. This makes colloids particularly useful as “big atoms,” a concept established through the sedimentation experiments of Jean Perrin, which provided quantitative support for the molecular nature of matter. Colloids therefore bridge microscopic molecular physics and directly observable soft-matter dynamics.

In this thesis, colloidal particles are used not only as passive model systems, but also as active particles. Their motion and interactions can be modified by surface charge, external electric fields, polymeric media and passive crowding. Therefore, the following sections introduce the

basic physical concepts required to understand colloidal suspension, Brownian motion, field-induced interactions and active propulsion in complex and crowded environments.

2.3 Interparticle Interactions

2.3.1 **Electrostatic Interactions**

When a charged colloidal surface is brought into contact with an electrolyte solution, the surrounding ions rearrange in response to the surface charge. Counterions accumulate near the surface, while co-ions are depleted. This leads to the formation of an electric double layer (EDL), which describes the charge distribution at the interface between the solid surface and the liquid electrolyte. In the Stern model, the electric double layer consists of two regions [67, 68, 69,]. Close to the particle surface, a compact Stern layer is formed by specifically adsorbed or strongly bound ions. Beyond this layer, the diffuse layer contains mobile ions whose distribution is determined by the competition between electrostatic attraction to the charged surface and thermal diffusion into the bulk solution (see Figure 2.1). The electrostatic potential therefore decreases with increasing distance from the surface. The characteristic length scale over which the electrostatic potential decays is the Debye length, κ^{-1} [70]. The inverse Debye length κ is given by

$$\kappa = \sqrt{\frac{e^2}{\varepsilon_0 \varepsilon_r k_B T} \sum_i n_i z_i^2} \qquad (2.1)$$

where e is the elementary charge, ε_0 is the vacuum permittivity, ε_r is the relative permittivity of the solvent, k_B is the Boltzmann constant, T is the temperature, and z_i, n_i are the valency and number density of ion species *i*, respectively. The Debye length characterizes the range of electrostatic interactions in the electrolyte. Increasing the ion concentration decreases the Debye length and therefore screens electrostatic interactions more strongly.

The inner part of the electric double layer can be regarded as almost immobile, whereas the ions in the diffuse layer remain mobile [71,72,]. During electrophoretic or electroosmotic motion, the hydrodynamic shear plane separates the fluid moving with the particle surface from the surrounding liquid. The electrostatic potential at this shear plane is called the zeta potential, ζ. It is an important experimentally accessible quantity because it determines the electrokinetic response of colloidal particles and strongly influences colloidal stability.

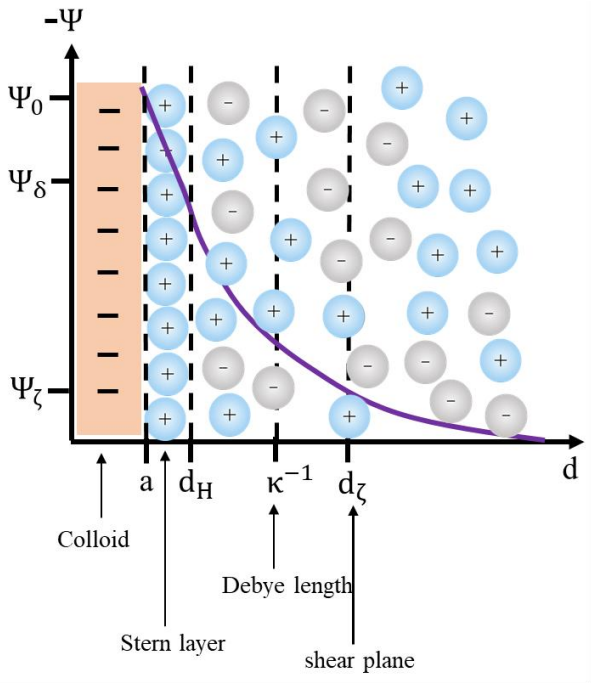

Figure 2.1, Schematic representation of the Stern model of the electric double layer. The electrostatic potential Ψ of a negatively charged colloids is shown as function of the distance d from the colloid surface. The electric double layer consists of a compact Stern layer and an adjoining diffuse layer. The Stern layer comprises the inner and outer Helmholtz layers. The inner Helmholtz layer is located at the colloid surface, while the outer Helmholtz layer coincides with the distance of closest approach of hydrated ions. Within the Stern layer, the potential decreases approximately linearly. Beyond the Stern layer, the diffuse layer begins, where the potential decreases approximately exponentially with distance. The Debye length characterizes the distance over which the potential decays to $\Psi = \Psi_0 e^{-1}$. The zeta potential ζ is defined at the shear plane, located at a distance d_ζ from the colloid surface, where the hydrodynamic boundary condition applies. The potentials at the outer Helmholtz layer and at the shear plane are denoted by Ψ_δ and Ψ_ζ respectively. Figure is adapted from Ref [67].

2.3.2 **van der Waals Interactions**

In addition to electrostatic repulsion, colloidal particles experience attractive van der Waals interactions. These interactions originate from correlations between fluctuating and induced dipoles in the particles and the surrounding medium [73, 74,]. They are generally always present and become particularly important at short particle separations [75]. For two spherical particles with radii r_1 and r_2, the van der Waals attraction can be approximated using Derjaguin's approximation as

$$V_{vdW} = -\frac{A_H}{6x}\frac{r_1 r_2}{r_1 + r_2} \qquad (2.2)$$

Where A_H is the Hamaker constant and x is the surface-to-surface distance between the particles. The Hamaker constant contains the material dependent information of the interacting particles and the surrounding medium. This expression shows that the attraction becomes stronger as the particle separation decreases. Van der Waals therefore promotes aggregation if it is not balanced by repulsive interactions, such as electrostatic double layer repulsion [76, 77]. Together, these two contributions form the basis of DLVO theory.

2.3.3 **DLVO Theory**

DLVO theory is named after Derjaguin, Landau, Verwey and Overbeek, who independently developed the theory in the 1940s [78]. It describes the stability of colloidal dispersions by considering the balance between attractive van der Waals forces and repulsive electrostatic double-layer forces. The total interaction potential between two colloidal particles can be written as

$$V_{DLVO}(x) = V_{\mathrm{vdW}}(x) + V_{el}(x) \tag{2.3}$$

Where V_{vdW} is the attractive van der Waals potential, V_{el} is the electrostatic repulsion, and x is the surface-to-surface distance between the particles.

This balance is illustrated schematically in Figure 2.2. The van der Waals contribution is attractive and becomes dominant at very short separation distances. In contrast, the electrostatic double-layer interaction is repulsive and can create an energy barrier when two similarly charged particles approach each other [79]. If this barrier is sufficiently high compared to the thermal energy $k_B T$, the particles remain dispersed and the suspension is stable.

At very small separations, however, the attractive van der Waals interaction can dominate, leading to a deep primary minimum in the total potential. Particles reaching this minimum typically coagulate irreversibly. At intermediate distances, the total DLVO potential may also exhibit a shallow secondary minimum, where particles can form weak and reversible aggregates. Thus, as shown in Figure 2.2, the shape of the total interaction potential determines whether a colloidal suspension remains stable, flocculates reversibly, or coagulates irreversibly.

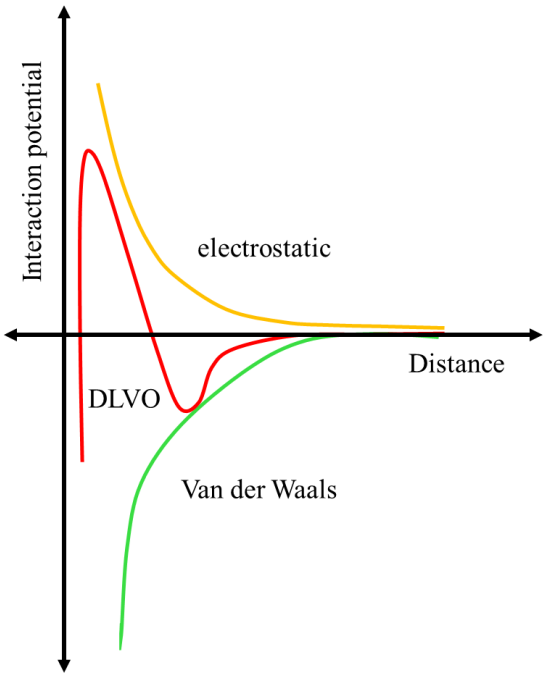

Figure 2.2, Schematic DLVO interaction potential between two charged colloidal particles as a function of separation distance. The attractive van der Waals contribution is shown together with the repulsive electrostatic double-layer interaction. Their sum gives the total DLVO potential, which determines whether particles remain dispersed, form weak reversible aggregates, or coagulate irreversibly. Figure is adapted from Ref [79].

2.3.4 **Phase Behavior of Colloidal Suspensions**

Colloidal phase behaviour is strongly governed by interparticle interactions. A fundamental interaction is hard-core repulsion, which prevents particles from overlapping. For hard-sphere like colloids, this repulsion defines the excluded volume available to neighbouring particles and gives rise to entropic contributions to the Gibbs free energy. As a result, phase transitions such as crystallization, melting, and glass formation can occur even in the absence of attractive interactions. In this case, the phase behaviour is mainly controlled by the particle volume fraction, ϕ and by the entropy associated with the available configurational space [80]. While temperature controls the phase behavior of molecular liquids, colloidal systems are often controlled by particle volume fraction ϕ, interaction range and interaction strength.

Hard-sphere colloids represent an important limiting case because their phase behavior is governed mainly by excluded-volume interactions and the volume fraction ϕ. They therefore provide a simple reference system for comparing experiments, simulations and theory. However, they are not the only useful model system. Charged colloids, whose interactions are governed by electrostatic repulsion, were investigated extensively nearly hard-sphere colloids

became experimentally available. More generally, colloids are valuable their micrometre-size size allows to use optical techniques such as light scattering [81,82,83] and confocal microscopy [84, 85,] and direct particle resolved tracking [86,87,88,89,] without requiring large scale facilities such as synchrotrons. Colloidal hard spheres are therefore widely regarded as model systems.

Figure 2.3, Phase behavior of colloidal hard spheres. Suspension of PMMA particles in a range of densities (increasing from left to right). The suspensions were shone by white light and they exhibited different diffraction patterns in the next few days indicating the crystallization and glass formation at different densities. Figure is adapted from Ref. [91].

Hard-sphere-like colloids provide an important reference system for studying phase behavior. In their classical experiments, Pusey and van Megen used sterically stabilized PMMA particles in a refractive index matched solvent to realize nearly hard-sphere suspensions [90, 91,]. By varying the effective volume fraction, they observed the sequence from fluid to fluid-crystal coexistence, crystalline order and, at sufficiently high-volume fraction, glassy arrest, see Figure 2.3. This established hard sphere colloids as a useful experimental model for comparing phase behavior with simulations and theory [92, 93,]. Typically, close packed crystal structures are formed (fcc, hcp) through stacking faults mixtures thereof [94, 95,]. In 2D, hexagonally close packed sheets form. In 3D, it has been observed in simulations and experiments on colloidal hard spheres that the melting transition is first order. Nevertheless, the situation is more complex in two-dimensional systems.

In three dimensions, hard-sphere crystallization typically leads to close-packed structures such as fcc, hcp, or mixtures containing stacking faults. In two dimensions, the corresponding dense ordered state consists of hexagonally arranged particles. However, melting in two-dimensional systems is more subtle than in three dimensions. Due to thermal fluctuations, true long-range translational order is suppressed in 2D, as described by the Mermin and Wagner argument [96]. Nevertheless, two-dimensional systems can still exhibit quasi long-range order and undergo transitions between liquid, hexatic and crystalline states. The nature of 2D melting has long been debated [97]. One scenario predicts a direct first-order transition between liquid and crystal, while the Kosterlitz-Thouless-Halperin-Nelson-Young (KTHNY) theory predicts two continuous transitions with an intermediate hexatic phase [98, 99, 100]. Numerical work by Bernard and Krauth showed that hard disks melt through a continuous liquid-hexatic transition followed by a first order hexatic crystal transition [101, 102]. This picture was later supported experimentally in quasi two dimensional colloidal hard-sphere monolayers.

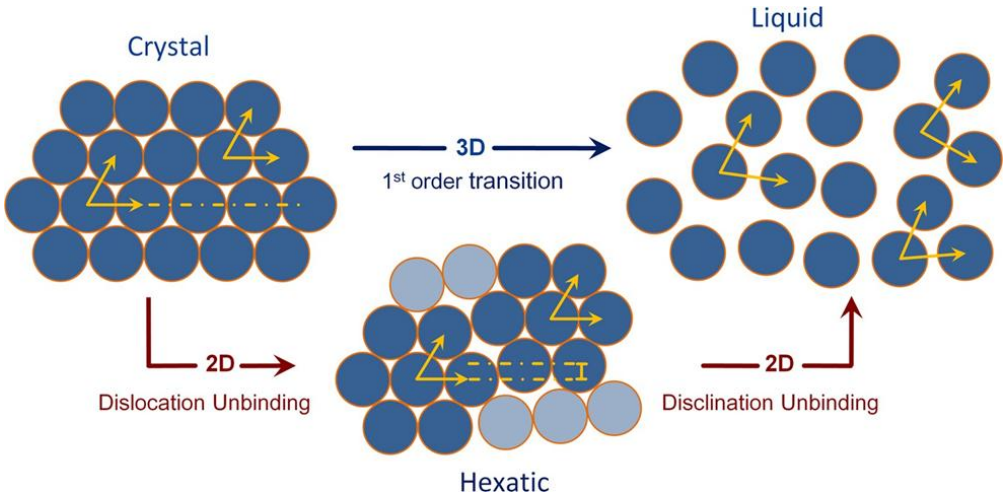

Figure 2.4, Schematic representation of the melting pathway from a crystalline phase to an isotropic liquid phase. In three dimensions, melting occurs through a single first-order transition, whereas in two dimensions it can proceed through a two-step process involving an intermediate hexatic phase, as described by the KTHNY theory. In the crystalline phase, both translational order and bond-orientational order are long-ranged. In the liquid phase, both orders are short-ranged. In the hexatic phase, translational order becomes short-ranged while bond-orientational order remains long-ranged. Figure is adapted from Ref. [104].

Figure 2.4 schematically summarizes the difference between the 3D and 2D transition scenarios. In a crystal, particles are arranged on a periodic lattice and exhibit both positional and bond orientational order [103, 104]. In 2D, the hexatic phase is characterized by the loss of long-range positional order while bond-orientational order remains quasi long-ranged. Upon transition to the liquid phase, orientational correlations are also lost. In real colloidal samples,

ordered states often contain defects. Instead of forming a single crystal, the system may become polycrystalline, consisting of multiple crystalline grains with different orientations. Defects tend to accumulate at grain boundaries, which separate neighboring domains [105, 106,]. This distinction is relevant for the experiments in this thesis, where passive colloidal monolayers are tuned into polycrystalline structures by external AC electric fields.

2.4 Dynamics of Colloidal Suspensions

2.4.1 **Colloidal Hydrodynamics**

The study of colloidal systems requires a thorough understanding of their behaviour under various conditions, including hydrodynamics. Colloidal particles are subject to Brownian motion, thermal fluctuations, and hydro dynamic interactions. Colloidal particle moves at very small length scales and typically at low Reynolds numbers [107, 108]. Under these conditions, viscous forces dominate over inertial forces, and the surrounding fluid responds almost instantaneously to particle motion. This regime is described by stokes flow [109]. A direct consequence is that the hydrodynamic drag force on a spherical particle moving with velocity u relative to a Newtonian fluid is [110],

$$F_d = -6\pi\eta a_H \vec{u} \tag{2.4}$$

Where η is the fluid viscosity and a_H is the hydrodynamic radius of the particle. The hydrodynamic radius is the effective radius that determines viscous drag. It can differ from the geometric radius because of surface roughness, adsorbed polymer or surfactant layers, or modified boundary conditions at the particle surface. This distinction is important in the present thesis because particle motion is studied close to solid boundaries, in polymer solutions, and in crowded colloidal environments, where hydrodynamic drag can deviate from the ideal bulk value.

At low Reynolds number, the time-reversibility of Stokes flow also has important consequences for microswimming [107, 111,]. Reciprocal motion cannot generate net propulsion, as expressed by Purcell's scallop theorem. Therefore, active colloids and microswimmers require non-reciprocal shape changes, surface flows, or phoretic mechanisms to generate directed motion.

2.4.2 **Brownian Motion and Diffusion**

Brownian motion describes the random displacement of suspended particles caused by thermal fluctuations of the surrounding solvent. For an isolated particle in a homogeneous fluid, this motion leads to diffusion. The mean squared displacement (MSD) grows linearly with time,

$$MSD(t) = 2dDt, \tag{2.5}$$

Where D is the diffusion coefficient and d are the spatial dimension. For a spherical colloidal particle in a Newtonian fluid, the diffusion coefficient is related to hydrodynamic drag by the Stokes-Einstein relation [112],

$$D = \frac{k_B T}{6\pi\eta a_H} \tag{2.6}$$

This expression shows that diffusion decreases with increasing viscosity and increasing hydrodynamic radius. It provides an important reference for interpretating passive particle motion and for estimating how polymer solutions or nearby boundaries modify particle mobility [113, 114, 115,]. In the experiments presented in this thesis, the ideal Stokes–Einstein description is mainly used as a reference case for dilute suspensions far from strong confinement. Deviations are expected near solid boundaries, in crowded colloidal environments, and in polymer solutions. In these cases, hydrodynamic interactions, caging by neighbouring particles, and viscoelastic or polymer-mediated stresses can modify the apparent diffusion coefficient.

This distinction is illustrated in Figure 2.5. At very short times, particle motion is affected by inertia and hydrodynamic coupling. At intermediate times, the particle explores the local cage formed by neighbouring particles, leading to a short-time self-diffusion coefficient D_S^{short}. At longer times, structural rearrangements of the surrounding particles become important, and the motion is described by a long-time self-diffusion coefficient D_S^{Long}, which is generally smaller than the free diffusion coefficient D_0 ($D_0 < D_S^{Short} < D_S^{Long}$) [116, 117,]. This figure is therefore relevant for the later analysis of active and passive particles in crowded environments, where the measured MSD does not only reflect single-particle diffusion but also the influence of the surrounding microstructure.

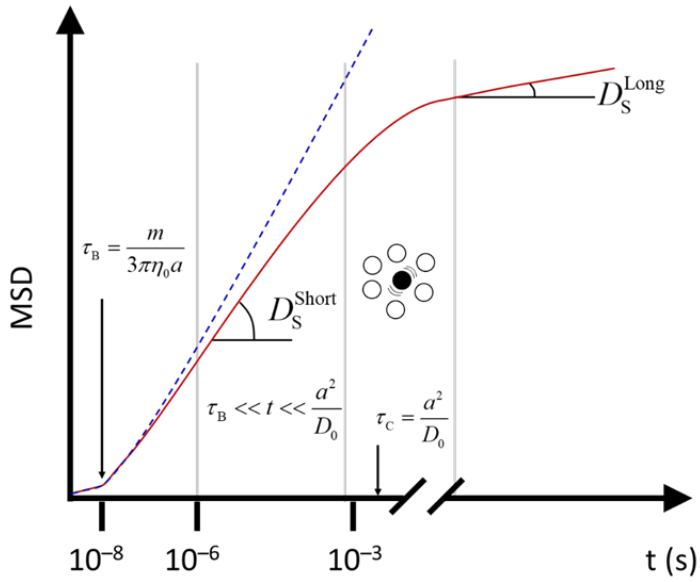

Figure 2.5, Schematic mean squared displacement of colloidal particles in dilute and concentrated suspensions. The blue dashed line represents free diffusion of an isolated particle with diffusion coefficient D_0. The red curve represents the MSD of a particle in a dense suspension. At short times, motion is reduced by hydrodynamic interactions and local caging, giving a short-time self-diffusion coefficient D_s^{short}. At longer times, rearrangements of the surrounding particles allow further displacement, described by the long-time self-diffusion coefficient D_s^{long}. Both axes are shown on logarithmic scales. Figure is adapted from Ref. [116].

2.5 Colloids under External Fields

2.5.1 **Gravitational Fields**

Besides solvent-mediated and interparticle interactions, external fields can also influence colloidal phase behavior. Gravity is the simplest example. In a colloidal suspension, gravitational settling competes with Brownian diffusion. At equilibrium, this competition leads to a height-dependent particle concentration: particles are more concentrated near the bottom of the sample, while the concentration decreases with height.

This sedimentation-diffusion equilibrium was central to Perrin's experiments on colloids [118]. By measuring the vertical concentration profile of colloidal particles, Perrin provided experimental evidence for statistical physics and enabled an independent determination of Avogadro's number. These experiments established colloids as observable model systems for molecular-scale thermal motion. Since Perrin's experiments, colloid science has advanced from manual particle counting to quantitative optical methods. Light scattering provides ensemble

information on colloidal structure and dynamics [119], while modern microscopy and particle-tracking methods allow individual particle trajectories to be measured directly [120].

2.5.2 **Electric-Field-Driven Interactions**

When a colloidal particle is placed in an external electric field, charges and ions redistribute at the particle electrolyte interface. If the particle and the surrounding medium have different dielectric properties or conductivities, this redistribution induces a dipole moment in the particle. The induced dipole is oriented parallel to the applied electric field, and its magnitude depends on the field strength, particle size, frequency, and dielectric contrast between particle and medium.

For a spherical particle, the induced dipole moment can be written as [121],

$$p = 4\pi\varepsilon_m R^3 KE \tag{2.7}$$

Where R is the particle radius, ε_m is the permittivity of the medium, E is the electricfield strength, and K is the Clausis-Mossotti factor. The factor K describes the polarizability contrast between the particle and the surrounding medium. The factor K contains the dielectric and conductive contrast between the particle and the medium and is therefore sensitive to particle material, solvent properties, salt concentration and field frequency [122, 123]. Different theoretical descriptions exist depending on the relevant frequency range and double-layer properties. The Maxwell Wagner model describes polarization due to conductivity and permittivity contrast, while extensions such as the Maxwell Wagner O'Konski model include surface conduction by charges in the electric double layer [124]. At lower frequencies, ion diffusion within the double layer becomes important and can be described by the Dukhin–Shilov approach [125, 126].

For thin double layers, the induced dipoles of two particles can be approximated by a point-dipole interaction. The resulting interaction depend not only on the interparticle distance r_{ij}, but also on the angle θ_{ij} between the center-to-center vector and the applied field as following [127, 128],

$$U_{ij}(r_{ij}, \theta_{ij}) = \frac{p_i p_j}{4\pi\varepsilon_m r_{ij}^3} (1 - 3\cos^2\theta_{ij}) \tag{2.8}$$

This expression shows that the interaction is orientation dependent. Particles aligned head-to-tail with the electric field attract each other, whereas particles arranged side-by-side repel each

other [129,130]. Since $p \propto$ E, the interaction strength scales approximately with E^2. Such field-tunable dipolar interactions are widely used to control colloidal assembly and are relevant in this thesis for the formation of passive colloidal structures.

Electric fields can be used to tune colloidal interactions and generate ordered structures that are not accessible by thermal motion alone. The resulting assembly depends not only on the particle material, but also on field type, field frequency, field direction, salt concentration and confinement geometry [131, 132, 133, 134].

Figure 2.6 summarizes several representative examples. In charged colloidal suspensions, Yethiraj et al. [135] discovered the combination of long-range electrostatic repulsion and field-induced dipolar interactions can generate different three-dimensional crystal symmetries, such as FCC, BCC, BCO and BCT structures, see Figure 2.6(a). The effective electrostatic repulsion can be tuned by particle charge, salt concentration and solvent properties, while the dipolar interaction is controlled by the applied electric field.

The combined action of Dielectrophoretic (DEP) and chaining forces can be used as a tool for AC field driven assembly of particle structures. For particles placed between planar electrodes, alternating electric fields can also drive two-dimensional assembly. As shown in Figure 2.6(b), particles may first form chains along the field direction due to dipole-dipole attraction [136, 137,]. These chains can then be attracted toward the electrode surface and reorganize laterally into a two-dimensional colloidal crystal. Thus, both the direction of the applied field and the interaction with the confining electrodes are essential for the final structure.

Gong et al. [138] found that confinement provides an additional control parameter. Figure 2.6(c) illustrates that changing the plate separation modifies the balance between dipolar repulsion and electrohydrodynamic attraction. Depending on this balance, the same type of particles can form compact triangular crystals, chains, honeycomb-like patterns or more disordered structures.

Finally, the particle polarizability is sensitively dependent on both field frequency and zeta potential. By tuning these parameters, Ristenpart et al. [139] observed new structures formed by a mixture of silica and polystyrene spheres As shown in Figure 2.6(d), this can lead to different superlattice structures depending on frequency and mixing ratio. These examples demonstrate that electric fields provide a versatile route to control colloidal assembly through particle polarization, electrohydrodynamic flows and confinement effects.

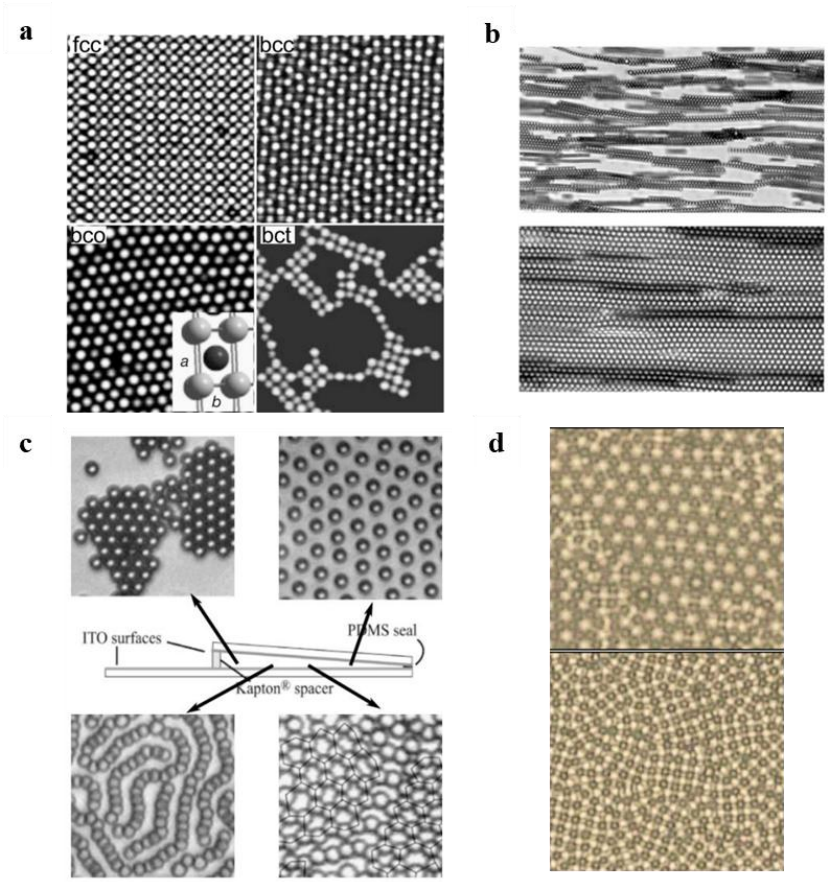

Figure 2.6, Examples of electric-field-induced colloidal assembly under different particle, field and confinement conditions. (a) colloidal crystals formed from charged isotropic spheres under an applied electric field. Depending on the balance between electrostatic repulsion and field-induced dipolar interactions, different crystal symmetries such as FCC, BCC, BCO and BCT can be obtained. Figure is adapted from Ref. [135]. (b) Two-stage assembly of latex spheres between planar electrodes under an alternating electric field. In the first stage, dipolar interactions align the particles into chains along the field direction. In the second stage, dielectrophoretic attraction to the electrode surface and lateral interactions between chains lead to a two-dimensional colloidal crystal. Figure is adapted from Ref. [136]. (c) Assembly of spherical particles under confinement between two plates. Depending on the plate separation, the competition between dipolar repulsion and electrohydrodynamic attraction produces close-packed triangular crystals, chain-like structures, honeycomb patterns or disordered colloidal crystals. Figure is adapted from Ref. [138]. (d) Binary colloidal superlattices assembled from silica and polystyrene particles under AC electric fields. Because the two particle types polarize differently, the field-induced dipolar interactions can be tuned by frequency and particle composition, leading to triangular superlattices for a 2:1 polystyrene: silica ratio and square-packed superlattices for a 1:1 ratio. Figure is adapted from Ref. [139].

2.5.3 **Dielectrophoretic (DEP) force of Colloids**

In addition to dipolar interactions between particles, non-uniform electric fields can also exert a net force on individual polarizable particles. This effect is known as dielectrophoresis (DEP) [140]. In contrast to electrophoresis, DEP does not require a net particle charge it arises from the interaction between an induced dipole and a spatial gradient of the electric field [141]. Therefore, DEP can occur for neutral as well as charged particles, provided that their polarizability differs from that of the surrounding medium.

The direction of dielectrophoretic motion depends on the relative polarizability of the particle and the medium. If the particle is more polarizable than the surrounding solution, it experiences positive dielectrophoresis (pDEP) and migrates toward regions of higher electric field strength [141]. If the particle is less polarizable than the medium, it experiences negative dielectrophoresis (nDEP) and migrates toward regions of lower electric field strength [142, 143,]. This distinction is controlled by the real part of the Clausius–Mossotti factor, which depends on particle material, medium conductivity, permittivity and field frequency [144].

DEP is relevant for the island-hopping experiments because local field gradients can arise near particle clusters, electrodes and Janus particles. These gradients influence how active particles approach, interact with, or are redirected by passive colloidal structures. Thus, DEP provides an important additional mechanism, beyond dipolar pair interactions, for understanding electrically driven motion in structured colloidal environments.

2.6 Dilute and semi dilute polymer suspensions

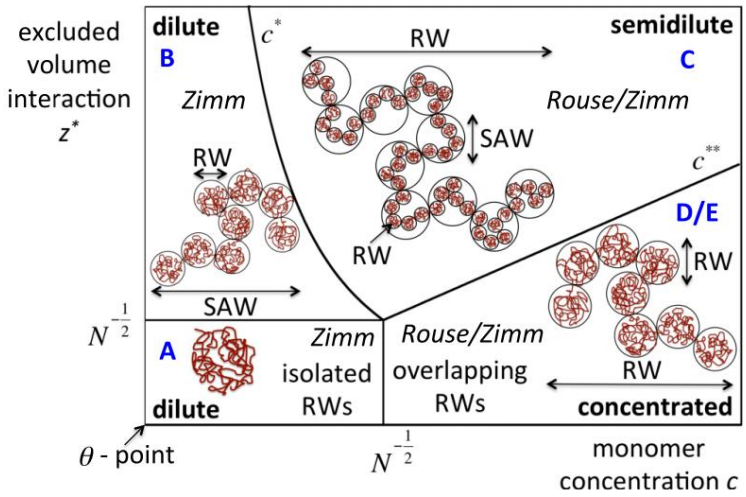

Figure 2.7, Phase diagram of a polymer solution plotted in terms of monomer concentration (c) and excluded-volume strength (z), as described by the standard blob picture. For small values of $z \lesssim N^{-1/2}$, the system lies in the θ-regime, while for $z \gtrsim N^{-1/2}$ it corresponds to the good solvent regime. The overlap concentration c^* marks the boundary between dilute and semi dilute solutions, and for concentrations well above c^{**}, excluded-volume interactions are completely screened. Figure adapted from Ref. [145].

Before discussing microswimmers in complex media, it is useful to clarify the terminology used in this thesis. A viscous environment mainly refers to increased resistance to motion, described by the viscosity η. A complex fluid, such as a polymer solution, contains additional microstructure and relaxation processes. A crowded environment contains suspended obstacles or passive particles that restrict and modify swimmer motion. A heterogeneous environment is spatially non-uniform, meaning that the local density, structure or resistance varies from one region to another.

Polymer solutions provide a useful example of how these descriptions are connected. Depending on concentration, polymer chains can behave as isolated coils in the dilute regime or as overlapping chains in the semidilute regime [145]. Thus, increasing polymer concentration does not only increase the viscosity, but can also introduce a microstructural background that modifies the motion of active particles. Figure 2.7 summarizes this idea using the standard polymer-solution phase diagram, where the crossover from dilute to semidilute solutions occurs at the overlap concentration c^*.

In the dilute regime, $c < c^*$, polymer coils are well separated and behave approximately as isolated chains. In the semidilute regime, $c > c^*$, the coils overlap and inter-chain interactions

become important, although the solution is still far from a melt or highly concentrated polymer system [146, 147]. The excluded volume strength z describes solvent quality near the θ condition, excluded volume interactions are weak and chains approach random-walk statistics, while in good solvent conditions, excluded volume interactions lead to self-avoiding walk conformations. In semidilute solutions, these interactions are screened beyond a characteristic blob size, so the chain behaves differently on local and large length scales.

This distinction is important for the present thesis because the first set of experiments uses PEG solutions to tune the surrounding medium of electrically driven Janus particles. These polymer solutions are therefore not only viscous backgrounds, but may also represent complex and, depending on concentration, microstructured environments. This framework also prepares the discussion of later experiments, where passive colloids introduce crowding and spatial heterogeneity.

2.7 Phoretic Motion of Active Colloids

2.7.1 **Self-Phoretic Swimmers**

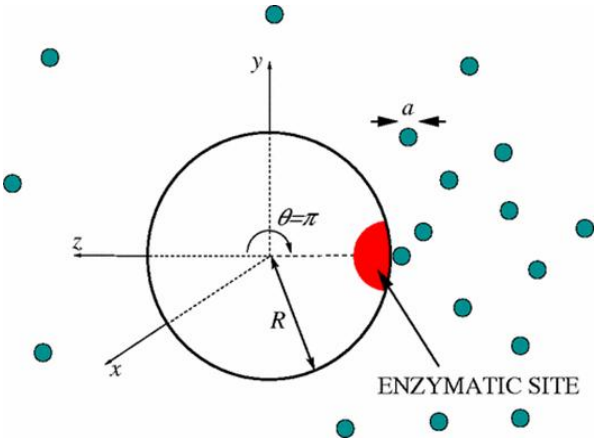

Figure 2.8, Schematic illustration of a self-diffusiophoretic Janus swimmer. A spherical colloid of radius R carries an enzymatic or catalytic patch on one side of its surface. The patch produces or consumes solute molecules asymmetrically, generating a non-uniform concentration field around the particle. The resulting concentration gradient drives interfacial slip and leads to self-diffusiophoretic propulsion. Figure is adapted from Ref. [149]

Phoresis describes the motion of a colloidal particle in response to a gradient, such as a solute concentration gradient, an electric field, or a temperature gradient. The gradient acts within a thin interfacial layer close to the particle surface and generates an effective slip velocity. Since colloidal particles move at low Reynolds number, such surface slip provides a possible route to

directed motion without relying on inertia. Self-phoretic swimmers use the same principle, but generate the required gradient themselves [148]. A homogeneous particle cannot sustain directed propulsion because the field generated around it remains symmetric. Net motion therefore requires broken spatial symmetry. This is commonly achieved by using patchy or Janus particles, where different regions of the surface have different chemical or physical properties.

Figure 2.8 illustrates this idea for a self-diffusiophoretic swimmer. The particle carries an enzymatic or catalytic patch on one side of its surface. This patch produces or consumes solute molecules locally and therefore generates an asymmetric concentration field around the particle. The resulting concentration gradient drives phoretic slip along the surface and leads to propulsion [149]. If the product molecules are neutral, the motion is self-diffusiophoretic and arises from osmotic stresses within the interfacial layer. Similar symmetry-breaking principles apply to other self-phoretic mechanisms, including self-electrophoresis and self-thermophoresis, depending on whether the particle generates ionic, electric, or thermal gradients. In all cases, directed motion results from the conversion of a locally generated asymmetric field into interfacial flow.

The active colloids used in this thesis are also Janus particles, but their propulsion is not chemically fuelled. Instead, the asymmetry between the metallic and dielectric hemispheres allows an external AC electric field to generate asymmetric electrohydrodynamic responses. Thus, the general concept remains the same, i.e., broken surface symmetry converts local gradients or field-induced flows into directed motion. This principle provides the basis for using electrically driven Janus particles as controllable active colloids in polymeric and crowded environments.

2.7.2 **Propulsion Mechanisms of Synthetic Microswimmers**

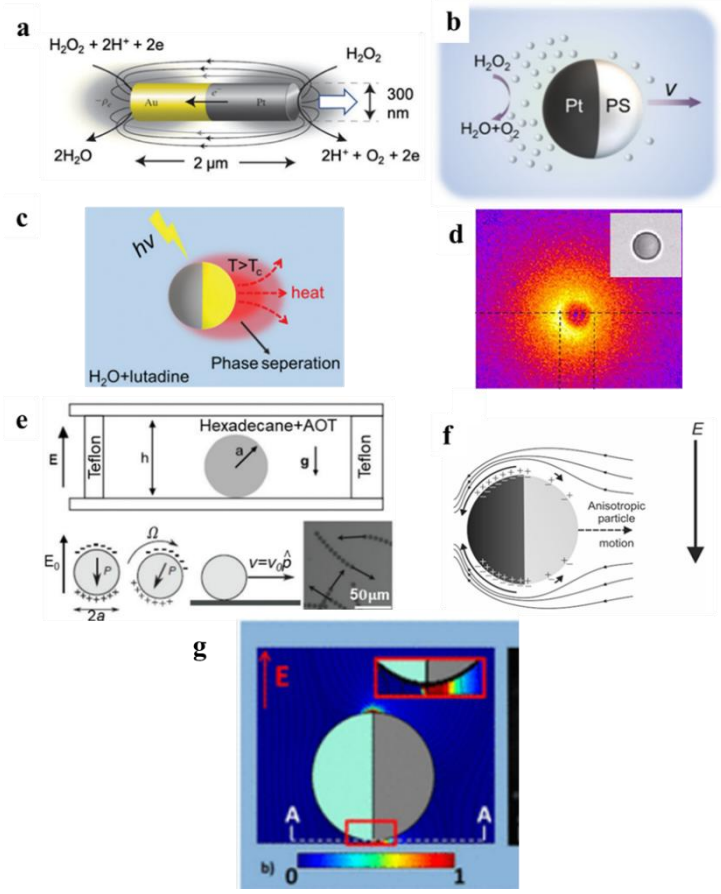

Figure 2.9, Overview of different propulsion mechanisms of synthetic microswimmers. (a) Au–Pt microrods move in H_2O_2 by generating and maintaining an ionic/proton gradient along the rod axis. Figure is adapted from Ref. [150]. (b) Pt-coated spherical Janus microswimmers propel by asymmetrically catalyzing the decomposition of H_2O_2 into water and oxygen. Figure is adapted from Ref. [166]. (c) Light-activated Janus microswimmers locally heat a near-critical water–lutidine mixture, causing asymmetric demixing around the particle. Figure is adapted from Ref. [173]. (d) Temperature distribution around a tethered 3 μm Au–PS Janus particle under laser irradiation, illustrating the asymmetric thermal field generated by optical heating. Figure is adapted from Ref. [174]. (e) Quincke rollers: uniform dielectric microspheres spontaneously roll under a DC electric field once the electrohydrodynamic instability threshold is exceeded. The panel shows the experimental setup and operating mechanism. Figure is adapted from Ref. [179]. (f) Induced-charge electrophoresis (ICEP) of an Au–PS Janus particle during one half-cycle of an AC electric field. The electric double layer near the gold hemisphere is more strongly polarized than near the polystyrene hemisphere, producing asymmetric ICEO slip flows and propulsion toward the dielectric side. Figure is adapted from Ref. [186]. (g) Self-dielectrophoresis (sDEP) of a metallodielectric Janus particle near an electrode. The different polarizabilities of the metallic and dielectric hemispheres distort the applied AC electric field, producing asymmetric field gradients enhanced by the nearby wall. These gradients generate a self-dielectrophoretic force that propels the particle toward the metallic hemisphere. The color scale denotes the normalized electric-field strength. Figure is adapted from Ref. [188].

Self-electrophoresis: Bimetallic microrods in hydrogen peroxide (H_2O_2) were among the first synthetic active colloids. They were reported around 2004–2005 by Sen, Mallouk and co-workers at Penn State [150] and by Ozin and co-workers at the University of Toronto [151]. These swimmers were initially fabricated as microrods with typical lengths of about $2\mu m$ and diameters of 200-300nm. Later, similar propulsion concepts were also realized with bimetallic Janus spheres [152]. Since then, bimetallic colloids have become an important model system for studying chemically driven microswimmers [153, 154, 155]. Their propulsion is generally explained by self-electrophoresis, as shown schematically in Figure 2.9(a). The two metals catalyze different electrochemical reactions of (H_2O_2), oxidation occurs mainly at the Pt side, while reduction occurs at the Au side. This asymmetric reaction creates unequal proton fluxes along the particle and generates a self-produced electric field from Pt to Au. Since the metallic swimmer is typically negatively charged, it moves electrophoretically in this internally generated field [156,157]. Thus, the particle does not require an externally applied electric field; instead, it creates the field needed for propulsion by its own surface chemistry. Although Pt Au is the most widely studied material combination, other bimetallic pairs can also swim by the same principle [158]. In some cases, additional mechanisms such as diffusiophoresis may contribute to the [159, 160], but self-electrophoresis is generally considered the dominant mechanism for these bimetallic H_2O_2 powered swimmers. A major limitation of this class of swimmers is the required use of H_2O_2 as fuel [161]. Besides possibly toxicity, H_2O_2 decomposition can generate oxygen bubbles, which disturb the experiment and reduce propulsion efficiency. This problem is particularly relevant for Pt-coated colloids, because Pt catalyzes the demoposition of H_2O_2 very efficiently [162, 163]. These limitations motivate the development of alternative propulsion strategies, including the fuel-free electrically driven Janus particles used in this thesis.

Self-diffusiophoresis: Another common route to self-propulsion is self-diffusiophoresis. In this mechanism, an asymmetric particle generates a local concentration gradient by producing or consuming solute molecules at one part of its surface. The resulting gradient creates an interfacial slip flow and drives particle motion. A typical example is the Pt-coated latex Janus particle introduced by Howse et al. [164]. Here, the Pt hemisphere catalyzes the decomposition of H_2O_2, producing an asymmetric chemical environment around the particle (Figure 2.9(b)) [165, 166]. The particle therefore moves persistently, while its swimming direction slowly changes due to Brownian rotational diffusion. Similar concentration gradient driven propulsion has also been realized using photocatalytic materials. For example, hematite-based swimmers

can decompose H_2O_2 under blue light illumination [167, 168,]. while TiO_2 coated silica particles generate chemical gradients under UV light [169]. In these systems, the activity can be controlled by the illumination intensity, which provides an additional experimental control parameter. A general limitation of fuel-based self-diffusiophoretic swimmers is that propulsion depends on the continuous availability of chemical fuel. Once the reactant is depleted, gradient production stops and the particles return to passive Brownian motion. This limitation becomes especially relevant for highly catalytic or large particles, where fuel consumption and bubble formation can become significant [170, 171,]. Related gradient-driven propulsion can also be induced without chemical fuel by using light and a critical binary mixture. Volpe et al. [172] and Buttinoni et al. [173] showed that half-metal Janus particles in a near critical water–lutidine mixture can self-propel under homogeneous illumination (see Figure 2.9(c)). In this case, local heating of the metal cap causes asymmetric demixing of the surrounding fluid, producing the gradient required for motion.

Self-thermophoresis: Self-thermophoresis is propulsion driven by a temperature gradient generated by the particle itself. If one side of a Janus particle absorbs light more strongly than the other, local heating creates an asymmetric temperature field around the particle. This temperature gradient can generate interfacial slip and drive particle motion. This mechanism was demonstrated by Jiang et al. [174, 175], who used half-metal-coated Janus microspheres suspended in water or dilute surfactant solution and illuminated them with a defocused laser beam (Figure 2.9(d)). The metal coated hemisphere absorbs the light and heats the surrounding liquid locally. As a result, a temperature gradient forms around the particle, leading to thermophoretic self-propulsion. The direction of thermophoretic motion is not universal. Depending on particle surface properties, solvent composition and solute or surfactant concentration, particles may move either away from or toward the heated region. Therefore, self-thermophoresis provides a light-controlled propulsion mechanism, but its direction and strength depend sensitively on the particle fluid interface.

Quincke rolling: Quincke rolling provides another route to active motion. In this case, the particles are not chemically asymmetric. Instead, dielectric spheres are suspended in a weakly conducting liquid and exposed to a uniform DC electric field. Above a critical field strength, the induced electric dipole becomes unstable and the particle starts to rotate spontaneously. If the particle is close to a solid substrate, this rotation is converted into rolling motion along the surface [176]. This mechanism was demonstrated by Bricard et al. [177, 178,] , using micron-sized dielectric spheres sedimented near the bottom surface (Figure 2.9(e)). Once the applied

electric field exceeds the Quincke threshold, the spheres begin to rotate in randomly selected directions and thereby self-propel along the substrate. The resulting propulsion can dominate over Brownian translational and rotational diffusion [179,]. Quincke rollers are useful model systems for studying collective active matter, especially polar flocking and large-scale organization in dense active suspensions [180, 181]. Compared to chemically driven swimmers, they do not require fuel-consuming surface reactions. However, they require relatively high DC voltages and carefully controlled electric fields, since field inhomogeneities can introduce additional effects such as dielectrophoresis.

Induced-charge electroosmosis (ICEO) and electrophoresis (ICEP): Induced-charge electro-osmosis (ICEO) describes electro-osmotic flow generated when an applied electric field acts on charge that it has induced near a polarizable surface [182, 183]. Around a homogeneous polarizable sphere this flow is symmetric, so no net particle motion occurs [184, 185]. Directed motion requires broken symmetry. This can be achieved with a metallodielectric Janus particle, where one hemisphere is metallic and the other is dielectric. For Janus particles in a low-frequency AC electric field, the metallic hemisphere polarizes more strongly than the dielectric hemisphere. This produces stronger induced-charge electro-osmotic slip near the metallic side, while the flow near the dielectric side is weaker. The resulting asymmetric flow field drives induced-charge electrophoresis (ICEP), causing the particle to move with the dielectric hemisphere forward [186, 187], as illustrated in Figure 2.9(f). ICEP typically occurs at low AC frequencies, on the order of a few kHz, where the electric double layer has enough time to charge during each field cycle. At much higher frequencies, the field oscillates too rapidly for the induced double-layer charge to follow, and the ICEP contribution decreases. At very low frequencies, additional electrohydrodynamic flows near the electrodes can become important and may lead to particle assembly or large-scale convection. This mechanism is particularly useful for active-colloid experiments because it is fuel-free and controlled externally. The propulsion speed and interactions can be tuned by the applied electric field, no chemical reaction is required, and the system can remain stable for long observation times. These properties make ICEP-driven Janus particles suitable model swimmers for studying active motion and collective behavior in well-controlled environments.

Self-Dielectrophoresis: At high AC frequencies, metallodielectric Janus particles can move by self-dielectrophoresis (sDEP), see Figure 2.9(g). This mechanism differs from both ICEO and ICEP. In ICEO, the applied field acts on induced charge in the electric double layer and generates electro-osmotic slip flow. In ICEP, this slip flow becomes asymmetric around a Janus

particle and produces propulsion, typically toward the dielectric hemisphere at low frequencies. In sDEP, the dominant effect is different. Here, the metallic and dielectric hemispheres polarize differently and distort the applied electric field. When the particle is close to a conducting wall, the wall introduces an additional symmetry breaking [188]. The combined asymmetry of the Janus particle and the nearby wall creates a localized non-uniform electric field around the particle. This field gradient acts on the induced dipole of the particle and generates a dielectrophoretic force. The important difference from conventional DEP is that the field gradient is not imposed externally by electrode geometry. Instead, it is generated locally by the particle itself in the presence of the wall. Therefore, sDEP-driven particles are not simply trapped in predefined high- or low-field regions, as in positive or negative DEP [189]. They can translate along individual trajectories and behave as active colloids, even though the energy input still comes from the external AC field. In contrast to low-frequency ICEP, sDEP drives the particle toward the metallic hemisphere. The crossover between ICEP and sDEP motion occurs at a characteristic frequency where the competing electrokinetic and dielectrophoretic contributions balance. This switching frequency depends on parameters such as electrolyte concentration and particle size.

2.8 Steering of active colloids

Propulsion alone does not make an active colloid fully functional. For applications such as transport, navigation through structured environments, or approaching a target, the swimmer must also be steered. Steering means that the direction or mode of motion can be controlled, not only the propulsion speed.

For many propulsion mechanisms discussed above, such as chemically powered self-electrophoresis, self-diffusiophoresis, self-thermophoresis or Quincke rolling, propulsion and steering often require different control strategies. For example, chemical swimmers are powered by fuel gradients or surface reactions, while light-activated and Quincke systems require optical or DC-field conditions. Achieving propulsion, direction reversal and interaction control with a single energy source is therefore not always straightforward.

Electrically driven Janus particles offer a useful route to combine propulsion and steering within one control parameter. Their motion depends on the frequency-dependent polarization of the metallic and dielectric hemispheres. At low frequencies, ICEP motion is typically directed toward the dielectric hemisphere [186, 187], whereas at higher frequencies sDEP motion [189] can occur toward the metallic hemisphere. Thus, changing the AC frequency can switch the

preferred direction of motion. In addition to such frequency-controlled motion reversal, deliberate steering along predefined paths can be achieved by adding a magnetic layer, such as nickel, to the metallic hemisphere and guiding the particle orientation with an external magnetic field. This strategy was demonstrated for Janus colloidal shuttles, where the AC electric field powered propulsion and cargo attachment, while the magnetic field controlled the direction of motion. This makes electric-field-based steering especially useful for the experiments in this thesis, where motion and interactions with targets or passive structures are controlled within the same experimental platform.

2.9 Self-Phoretic microswimmers moving in various environments

The previous sections introduced how self-phoretic and electrically driven colloids generate propulsion. In real applications, however, microswimmers rarely move in simple Newtonian fluids without obstacles. Instead, they often encounter complex or crowded environments, where viscosity, viscoelasticity, confinement, passive obstacles and spatial heterogeneity can strongly modify their motion.

In the following section, several representative cases are introduced. First, swimmers in viscous or viscoelastic polymer solutions are discussed, where the surrounding medium can slow down propulsion, alter rotational diffusion or introduce memory effects. Secondly, swimmers in crowded environments are considered, where passive particles or obstacles can lead to collisions, trapping, clustering or guided motion. Finally, systems combining polymeric and crowded environments are relevant, because they more closely resemble realistic transport settings in which microswimmers must move through structured and resistive media.

These examples provide the background for the experiments in this thesis, where electrically driven Janus particles are studied in PEG solutions, passive colloidal structures and cargo-transport configurations

2.9.1 **Microswimmer Dynamics in Polymeric and Viscoelastic Media**

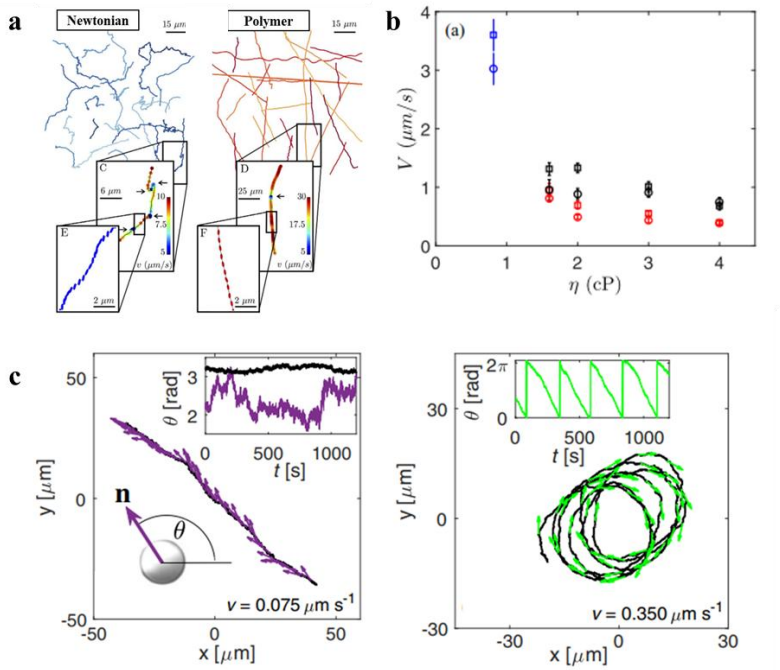

Figure 2.10, Representative examples of microswimmer dynamics in polymeric and viscous media. (a) Run-and-tumble trajectories of *E. coli* in a Newtonian buffer (η=1.0 mPa s) and in a dilute polymer solution of carboxy-methyl cellulose, CMC (MW=7.0×10^5, c=500ppm, η=19mPas. n the polymer solution, the cell trajectories become straighter, tumbling events are suppressed, and body wobbling is reduced. Figure adapted from Ref. [190]. (b) Propulsion velocity of catalytic silica–Pt Janus spheres in hydrogen peroxide solutions with varying viscosity. The particles are approximately 0.96μm silica microspheres half-coated with Pt and suspended in 3 M or 4 M H_2O_2, the viscosity is adjusted using glycerol. Increasing viscosity reduces the propulsion velocity, showing the strong role of viscous drag and fuel viscosifiers interactions in chemically driven swimmers. Figure adapted from Ref. [191]. (c) Light-activated spherical microswimmers in a viscoelastic fluid. The swimmers are silica particles (a=3.88μm) half-coated with carbon and suspended in water propylene glycol n-propyl ether mixture containing semidilute polyacrylamide (PAAm). At $v_0 = 0.075\ \mu m s^{-1}$, the particles show persistent random walk motion, whereas above a critical speed $v_c = 0.24 \mu m s^{-1}$ for 0.05 wt% PAAm, they switch to persistent circular motion. A representative circular trajectory is shown at $0.350 \mu m s^{-1}$. Figure adapted from Ref. [192].

One might expect that adding molecular solutes to an otherwise homogeneous suspension is a relatively simple way of making the environment more complex. However, several studies show that polymeric and viscosified media can modify microswimmer motion in qualitatively different ways, depending on whether the dominant effect is viscosity, elasticity, fuel transport, or fluid memory.

Patteson et al. [190] studied the run-and-tumble motion of *E. coli* in polymeric solutions, mainly using dilute carboxy-methyl cellulose CMC (MW=7.0×10^5, c=500ppm, η=19mPas), well below the overlap concentration. As shown in Figure 2.10(a), cells in Newtonian buffer frequently change direction, whereas cells in the CMC solution move along straighter trajectories. The polymer suppresses tumbling and reduces body wobbling. Their analysis showed that viscosity mainly suppresses tumbles, while elasticity enhances swimming speed by reducing wobbling of the cell body. This example demonstrates that even dilute polymer additives can affect swimmer trajectories, not only by increasing viscosity but also through elastic feedback from the medium.

A different response is observed for chemically driven catalytic Janus particles. Chatterjee et al. investigated silica–Pt Janus spheres of approximately 0.96μm diameter in 3M and 4M H_2O_2, with viscosity adjusted using sucrose or glycerol [191]. As shown in Figure 2.10(b), the propulsion velocity decreases with increasing viscosity. However, the viscosifier does not only increase hydrodynamic drag; it can also modify the local chemical environment of the motor, for example by changing fuel transport and interactions between H_2O_2, reaction products and the Pt surface. Thus, for catalytic swimmers, polymeric or molecular additives may influence both the medium resistance and the chemical processes that generate propulsion.

Narinder et al. showed that viscoelasticity can even change the type of trajectory [192]. They studied light-activated silica particles (a=3.88μm) half-coated with carbon in a water–propylene glycol n-propyl ether mixture containing semidilute polyacrylamide (PAAm). At $v_0 = 0.075\ \mu m s^{-1}$ the particles show persistent random walk like motion (see Figure 2.10(c)), whereas above a critical velocity $0.24\ \mu m s^{-1}$ for 0.05wt% PAAm, they switch to persistent circular motion as shown in Figure 2.10(d). This transition was attributed to the delayed response, or memory, of the viscoelastic fluid.

Together, these examples show that polymeric environments cannot be described by viscosity alone. Depending on the swimmer and medium, polymers can slow propulsion, suppress rotational motion, enhance persistence, or generate new trajectory modes. This motivates the experiments in this thesis, where electrically driven Janus particles are studied in PEG solutions to determine how polymer-induced resistance and field-controlled activity together govern active motion.

2.9.2 **Active passive interactions in Crowded colloidal systems**

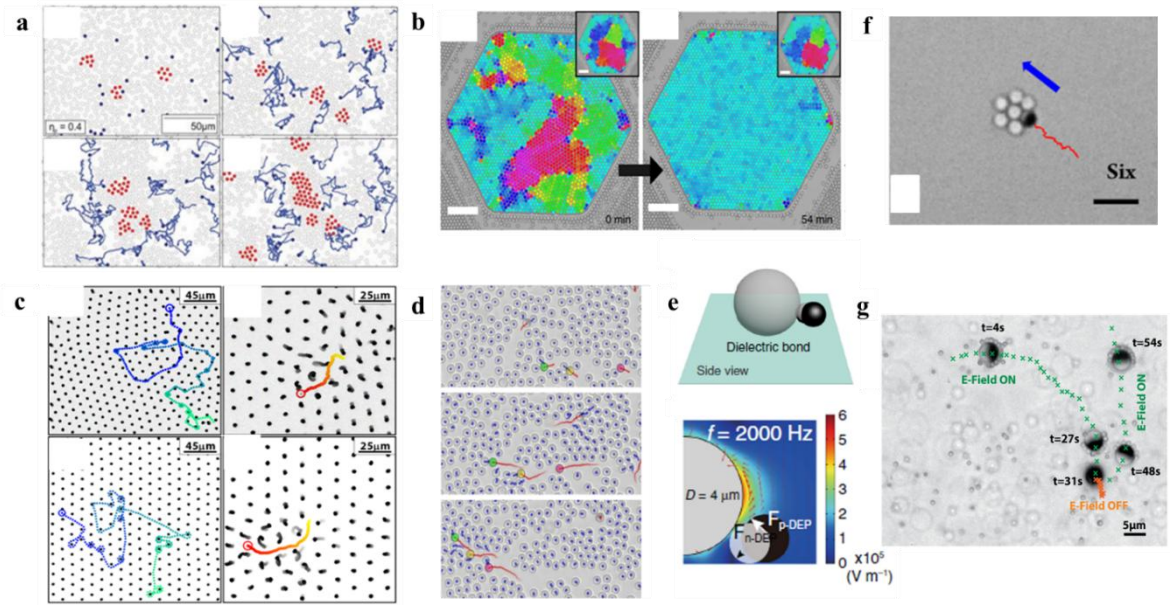

Figure 2.11, (a) Snapshots showing the time evolution of a mixture of passive (Z_p = 0.40) and active ($Z_a \approx 0.01$) particles at t = 0, 600, 900, and 1200s for Pe ≈ 20. Passive particles in clusters are shown as red circles, isolated passive particles as open circles, and active particles as blue dots with their 300 s trajectories indicated by blue lines. Figure adapted from Ref. [193]. (b) Activity-assisted annealing of a polycrystalline colloidal monolayer. An initially quenched polycrystalline structure relaxes into a more ordered monolayer after activation of self-propelled particles. Figure adapted from Ref. [194] (c) Active particles in a colloidal crystal. Active interstitials remain mobile and move in a run and tumble like manner, with passive colloids acting as scattering sites that randomize the direction of motion. Active particles incorporated into the lattice show intermittent motion due to the combined effect of self-propulsion and the periodic potential landscape. Figure adapted from Ref. [195]. (d) Collective path formation by Janus particles in a dense passive medium. A leading particle opens a path through the passive background, which is then followed by other particles; this leads to channel formation and clustering of the active particles. Figure adapted from Ref. [196]. (e) Dielectrophoretic binding in an active–passive colloidal molecule. A metallodielectric patchy particle attaches to a dielectric sphere through field-induced pDEP and nDEP contributions. The finite-element calculation shows that the bond is stabilized by negative dielectrophoretic attraction of the dielectric lobe, assisted by positive dielectrophoresis of the metallic lobe. Red arrows indicate electric-field lines, and the color scale denotes electric-field strength. Figure adapted from Ref. [197]. (f) Organized cargo loading by an active motor assembly transporting six passive non-motor spheres. The track lines show the motion over 2 s. Scale bar is 5 μm. Figure adapted from Ref. [198]. (g) Cargo transport by a Janus colloidal shuttle under an external electric field. The shuttle traps and transports passive cargo while the field is on and releases the cargo when the field is switched off. The shuttle trajectory is shown in green during field-driven transport and in orange after field removal. Figure adapted from Ref. [199].

Crowded colloidal environments do more than restrict swimmer motion. When active and passive particles are mixed, the swimmers can continuously perturb, rearrange and sometimes organize the passive phase. At the same time, the passive particles modify the swimmer trajectories through collisions, confinement and local structural barriers. Active–passive mixtures therefore provide a useful model system for understanding how activity and crowding influence each other.

A clear experimental example is provided by Kümmel et al., who studied mixtures of equally sized active and passive silica colloids with diameter 4.23μm [193]. A small fraction of particles was half-coated with a 10nm carbon layer and became active under illumination in a near-critical water–2,6-lutidine mixture. The active area fraction was kept low, Z_a≈0.01, while the passive area fraction was varied between Z_p≈0.10 and 0.90. The motion was confined to two dimensions in cells of about 6μm height, and the activity corresponded to Pe ≈ 20. Figure 2.11(a) shows the case Z_p= 0.40. After illumination, active particles swim through the passive suspension and generate local density variations. This leads to the formation of passive clusters, shown in red, while active particles are shown in blue with their trajectories. The active particles tend to localize at cluster boundaries, where they continue to compress and reshape the aggregates. The observed behavior depends strongly on Z_p, low passive density shows little structural change, intermediate density leads to cluster formation and compression, and high density leads to local melting of crystalline regions by active particles at grain boundaries. This example is relevant for this thesis because it shows that passive colloids are not merely obstacles, their structure can be modified by active motion and, in turn, can influence swimmer trajectories.

Ramananarivo et al. [194] used active particles as internal dopants to accelerate the annealing of passive colloidal monolayers. Their system consisted of 5μm silica beads sedimented into a dense quasi two-dimensional monolayer with surface fraction Φ_S≈0.68. The passive particles were confined in shallow hexagonal wells, where rapid sedimentation initially produced a polycrystalline structure with grain boundaries. A small fraction of 2μm light activated hematite-based swimmers was added as active intruders. Under UV illumination (λ = 390-480nm), the hematite decomposed H_2O_2, leading to phoretic propulsion of the active particles. As shown in Figure 2.11(b), activation of the swimmers strongly accelerates the relaxation of the initially polycrystalline monolayer. Within 54min, the system evolves toward a more ordered state, whereas the purely thermal system changes only weakly over the same time. The active intruders collide with passive beads and generate additional fluctuations inside the

monolayer. These fluctuations help the system overcome kinetic barriers at grain boundaries and promote defect removal. This example shows that active particles can be used not only to disturb passive structures, but also to anneal and improve the order of colloidal materials.

Dietrich et al. studied active particles moving inside loosely packed two-dimensional colloidal crystals at a flat water–hexadecane interface [195]. The system consisted of fluorescent polystyrene particles with radius R=1.4μm, where about 1% of the particles were half-coated with a 2nm Pt layer. In the presence of $H_2\,O_2$, the Pt-coated particles become self-phoretically active, while the uncoated particles formed a passive crystalline monolayer through long ranged electrostatic dipolar repulsion at the interface. As shown in Figure 2.11(c), two different types of active motion were observed, depending on the coupling between the active particle and the passive lattice. Weakly coupled active particles behaved as active interstitials: they moved through the crystal, collided with passive colloids, and reoriented in a run and tumble like manner. Strongly coupled active particles behaved as active atoms: they became part of the lattice and showed intermittent motion governed by the competition between self-propulsion and the periodic potential landscape of the crystal. This example shows that passive crystalline order can either scatter active particles or incorporate them into the lattice, depending on particle lattice coupling.

Dias et al. studied group formation of active Janus particles in a dense passive colloidal environment [196]. Their system consisted of 4.77μm silica Janus particles half-coated with a 60nm carbon layer and suspended in a near-critical water–2,6-lutidine mixture. Under green laser illumination (λ=532nm), local heating at the carbon cap produced self-propulsion with a speed of about $v \approx 1.9\mu m\, s^{-1}$. The active particles were mixed with freely diffusing passive silica colloids of the same size, with active area fraction $0.5\% \leq \rho_a \leq 75\%$. As shown in Figure 2.11(d), active particles moving through the passive background displace surrounding colloids and create transient open paths. These paths persist for a finite time before closing by Brownian motion of the passive particles. Other active particles can reuse these lower-resistance paths instead of digging new ones. This path reuse leads to collective path formation and promotes clustering of the active particles. The mechanism is an example of environmental memory: the passive medium stores information about the earlier passage of active particles and feeds back on later swimmer motion.

Wang et al. used AC electric fields to assemble active colloidal molecules with selective and directional bonds [197]. Their system consisted of a central dielectric sphere and metallodielectric patchy particles containing a dielectric polymer lobe and a metallic gold lobe.

The particles were suspended in deionized water between two ITO-coated glass electrodes, and an AC electric field was applied perpendicular to the substrate. The field frequency was varied between 300 and 4000Hz, with example in Figure 2.11(e) shown at f=2000Hz. As shown in Figure 2.18(e), the patchy particle attaches to a 4μm dielectric sphere through a dielectric bond. The dielectric lobe is trapped by negative dielectrophoresis in the low-field region near the central sphere, while the metallic lobe contributes through positive dielectrophoresis. The finite-element calculation shows the asymmetric electric-field distribution around the contact region; red arrows indicate the field lines and the color scale represents the electric-field strength. This example demonstrates how field induced pDEP and nDEP can be combined to create directional active passive binding.

Gao et al. demonstrated organized cargo loading using chemically powered Janus micromotors and passive non-motor particles [198]. The Janus motors were silica microspheres modified with hydrophobic octadecyltrichlorosilane (OTS) on one side and coated with a catalytic Pt hemisphere on the other side. In 5% H_2O_2, the Pt cap decomposes the fuel and drives autonomous motion, while hydrophobic interactions between OTS modified regions guide the attachment of passive cargo particles. As shown in Figure 2.11(f), a single Janus motor can transport multiple passive spheres in an organized motor–cargo assembly. For the case of six non-motor spheres, the cargo forms a packed "flower-like" arrangement around the motor. The motor speed decreases as the cargo load increases, from about $15\mu m\ s^{-1}$ for a free motor to about $3\mu m\ s^{-1}$ when carrying six passive particles. This example shows how specific motor cargo interactions can enable controlled loading and collective transport at the microscale.

Demirörs et al. demonstrated cargo transport using electrically driven Janus colloids as programmable shuttles [199]. The Janus particles were 4.64μm silica spheres with one hemisphere coated by a metallic layer. In the cargo-transport experiments, the shuttles were mixed with polystyrene cargo particles in deionized water and placed between transparent ITO electrodes. An AC electric field in the high-frequency range 0.5-2.5 MHz induced both self-dielectrophoretic motion of the Janus shuttle and dipolar attraction between the shuttle and cargo. As shown in Figure 2.11(g), cargo particles attach mainly to the metallic hemisphere while the electric field is on. The shuttle then transports the cargo along its field-driven trajectory. When the electric field is switched off, the induced dipolar attraction vanishes, the Janus particle stops, and the cargo is released. The trajectory is shown in green during field-driven transport and in orange after field removal.

Finally, the examples summarized in Figure 2.11 show that active–passive colloidal systems can exhibit a wide range of functions depending on the nature of the interaction between swimmers and their environment. Active particles can cluster passive colloids, anneal crystalline defects, move through or become incorporated into ordered lattices, create collective paths, form directional bonds, and transport passive cargo. These studies demonstrate that passive particles are not merely obstacles for active motion, but can act as dynamic components that are reorganized, transported, or used as functional elements. This provides the motivation for the experiments in this thesis, where electrically driven Janus particles are studied in passive colloidal and polymeric environments to understand how activity, crowding, and field-induced interactions together control microscale transport and organization.

2.10 Summary and motivation for the present thesis

The literature discussed in this chapter shows that active colloids are powerful model systems for studying transport, self-organization and interaction with structured environments. At the same time, it also reveals several challenges that motivate the present thesis. First, many active-particle systems are difficult to control independently. Chemical swimmers, for example, often couple propulsion to fuel concentration, reaction products and local gradients. As a result, changing the activity can also change the surrounding medium. For systematic experiments in complex environments, however, it is desirable to have a swimmer whose speed, direction and interactions can be tuned externally without modifying the chemical composition of the suspension.

A second challenge concerns the environment itself. Complex, viscous, crowded and heterogeneous media are often treated separately, although in experiments they may be strongly connected. Polymer solutions can increase viscosity and introduce microstructural relaxation, while passive colloidal particles can generate crowding, obstacles and spatial heterogeneity. This raises the question of whether one can design experimental environments whose structure and mechanical properties are controllable, while the swimmer activity is controlled independently.

A third challenge is transport functionality. Many active colloids can pick up or interact with passive particles, but controlled cargo pickup, transport and release require more than propulsion. A useful swimmer should allow directed motion, reversible binding and, ideally, a load-free return after release. This motivates the use of electrically driven Janus particles, where

the propulsion direction and particle cargo interaction can be changed by the applied AC frequency.

Finally, these considerations define the strategy of this thesis. First, reproducible Janus particle and passive-colloid systems must be prepared and characterized. This is addressed in Chapter 3. Next, the individual components and selected experimental conditions must be tested in simple environments before more complex situations are studied. This is developed in Chapter 4. The following chapters then address how electrically driven Janus particles move in polymer solutions, how they interact with structured passive colloidal environments, and how frequency-dependent propulsion and dielectrophoretic interactions can be used for cargo pickup, transport and release.

The central motivation is therefore not only to study active motion in complex and crowded media, but to establish a controllable experimental platform in which swimmer activity, environmental structure and active passive interactions can be tuned systematically. This provides the basis for investigating how active colloids behave in viscous, polymeric, crowded and heterogeneous environments, and how these interactions can be used to design functional microscale transport.

Chapter 3 - **Materials and Methods**

3.1 Introduction

The previous chapter identified the need for a controllable active colloid platform in which swimmer properties, environmental conditions and active passive interactions can be tuned reproducibly. Before such experiments can be interpreted, the individual components of the system must first be prepared in a controlled way and characterized independently. This chapter therefore describes the experimental basis of the thesis.

The chapter first introduces the materials used for the preparation of Janus particles, passive colloids, polymer solutions and sample chambers. Particular emphasis is placed on the fabrication and characterization of gold coated Janus particles, since their geometry and reproducibility determine the reliability of the later propulsion experiments. The preparation of the surrounding environments is then described, including viscous polymer solutions, passive colloidal suspensions and structured colloidal assemblies.

The chapter also introduces the experimental setup used to apply AC electric fields and to image particle motion. Finally, the methods for particle tracking, trajectory reconstruction and quantitative analysis are presented. Together, these procedures establish the reproducibility of the swimmer system and provide the technical foundation for the experiments discussed in the following chapters.

3.2 Sample preparation and Experimental setup

3.2.1 **Preparation of polymer environment**

Aqueous polyethylene glycol solutions were used to prepare viscosified polymer environments for the Janus-particle experiments. Polyethylene glycol powder (PEG 6000, Sigma-Aldrich, Germany) was dissolved in deionized water at room temperature. Solutions with PEG concentrations between 20 to 200 $\mathrm{mgmL^{-1}}$ were prepared. The mixtures were gently stirred until the polymer was fully dissolved and the solutions appeared homogeneous.

PEG 6000 was chosen because it is a non-ionic, water-soluble polymer that increases the viscosity of the suspending medium without introducing strong additional electrostatic interactions. Its molar mass, $M_w = 6000$ $\mathrm{gmol^{-1}}$ provides an experimentally accessible dilute

to semidilute crossover while keeping the solutions transparent and suitable for optical microscopy. The overlap concentration c^* at which polymer coils begin to overlap, depends on the polymer molar mass through the coil size. For PEG 6000 in water, literature values and scaling estimates give $R_g = 3 - 4\text{nm}$, corresponding to c^* on the order of 80 mg mL^{-1}. Thus, the chosen concentration range covers dilute conditions (20 mg mL^{-1}), the cross over region around c^*, and semidilute polymer solutions ($100 - 200$ mg mL^{-1}).

The density and viscosity of the prepared PEG solutions were measured before their use in the experiments. Solution densities were determined using a densimeter (DM 40, Mettler Toledo), yielding values between $1.0000\ and\ 1.0144$ g cm^{-2}. Dynamic viscosities were measured with a rolling-ball microviscometer (Lovis 2000M, Anton Paar), giving viscosities in the range of $\eta_{PEG} = 1.44$ to 8.00 mPas , depending on PEG concentration.

Finally, to characterize the rheological response of the polymer solutions in more detail, additional measurements were performed with a rheometer (MCR 702, Anton Paar, Germany). Frequency dependent measurements of the storage modulus G' and loss modulus G'' were carried out at $T = 22^0C$ using a DIN 54453 compliant double-gap measuring system (DG26, Anton Paar, Germany). Frequency sweeps were performed from $0.0\ to\ 100$ $rads^{-1}$ in 1 $rads^{-1}$ steps at a constant strain amplitude of $\gamma = 5\%$, within the linear viscoelastic regime. Shear-rate-dependent viscosity measurements were conducted between $1\ to\ 100$ s^{-1} at 22^0C using the standard measuring system DG26.7/T200/SS.

3.2.2 **Preparation of passive colloidal particles**

Passive colloidal environments were prepared using uncoated dielectric microspheres. These particles were not self-propelled, but their arrangement and interactions could be tuned by the applied AC electric field. Two types of passive environments were used in this thesis: island-like crowded obstacle landscapes and polycrystalline colloidal matrices.

For island-like crowded environments, passive silica microspheres with radius $R_p = 1.15\mu m$ (microparticles, GmbH, Germany) were dispersed in the sample chamber together with the Janus particles. At low AC frequencies, f~1kHz, the electricfield induces electrohydrodynamic flows along the conductive substrate. These flows are directed toward the silica particles and change the effective interaction between uncoated spheres from repulsive to attractive [200, 201, 202,]. As a result, the passive particles assemble into compact island-like clusters. These

clusters provide spatially heterogeneous crowded environments through which the Janus particles move.

For polycrystalline environments, untreated polystyrene particles with radius $R_p = 1.43\mu m$ (microparticles, GmbH, Germany) were used. The particle suspension was confined to a quasi-two-dimensional sample chamber and subjected to an AC electric field applied normal to the conductive substrate. The field frequency was set to $f \sim 20kHz$ and the field amplitude was increased up to $E = 108\ Vmm^{-1}$. Under these conditions, the electric field polarizes the dielectric particles and induces long range repulsive pair interactions [203, 139,]. The interaction strength increases with field amplitude, allowing the passive particles to organize into ordered or polycrystalline monolayers.

Thus, by changing the passive particle type and the applied electric-field conditions, two different passive environments could be prepared, i.e., (a) attractive, heterogeneous island-like clusters and (b) repulsive, tunable polycrystalline structures. These environments were used to study how active Janus particles move in crowded, structured and field-controlled passive colloidal landscapes.

3.2.3 **Preparation of Janus particles**

Janus particles were fabricated using a protocol adapted from Yan et al. [37], in collaboration with the group of Prof. H. J. Butt group at the Max Planck Institute for Polymer Research, Mainz. The same general procedure was used for both silica and polystyrene particles. Silica particles (SiO_2 , $R_a = 2.50 \pm 0.09\mu m$, Bangs Lab, USA, Lot: 16595) were purchased from Bangs laboratories, while polystyrene particles (Ps, $R_a = 2.17 \pm 0.04\mu m$, microparticles, GmbH, Germany, Lot: PS-R-4.4-L1237) are purchased from microparticles. Glass substrates were first cleaned by sequential sonication in Hellmanex cleaning solution (1wt.%) to remove surface contaminants. A dilute aqueous suspension of particles was then spread onto the cleaned glass substrates and allowed to dry slowly by evaporation. During drying, the particles formed close-packed monolayers on the substrate surface.

The exposed upper hemispheres of the particles were subsequently coated by thermal evaporation using an Edwards BOC Auto 306 multi-system evaporator. First, a thin chromium adhesion layer (3 nm) was deposited, followed by a gold layer (15nm). The deposition was performed under vacuum at a pressure of approximately $8.2 \times 10^{-5} mbar$. During coating, the substrates were rotated to improve the uniformity of the deposited metal layer over the exposed particle hemispheres. The layer thickness was controlled in situ using the quartz-crystal

microbalance thickness monitor integrated in the evaporation system. Therefore, the reported chromium and gold thicknesses correspond to the nominal deposited film thicknesses measured during evaporation. No separate thickness measurement was performed on every Janus-particle batch after deposition.

After metal deposition, the coated particles were detached from the substrate by sonication in ultrapure water. The resulting suspension was allowed to sediment, and the Janus particles were collected and stored in water for later experiments. This procedure produced metallodielectric Janus particles with one gold-coated hemisphere and one uncoated dielectric hemisphere.

3.2.4 **Experimental Setup**

Electrically driven Janus-particle experiments were performed on a Leica inverted optical microscope, as shown in Figure 3.1(a). The microscope was equipped with a Basler CMOS camera for image acquisition and a function generator for applying AC electric fields to the sample chamber.The sample cells consisted of two transparent indium tin oxide (ITO)-coated glass slides with a surface resistivity of $25 - 30\ \Omega\ \mathrm{sq}^{-1}$ ((Solems S.A, France). The two ITO-coated glasses were arranged parallel to each other, with the conductive sides facing inward, and separated by a circular adhesive spacer of thickness 120 μm (Grace Bio-Labs SecureSeal). The particle suspension was introduced into the chamber before sealing. This geometry allowed an AC electric field to be applied perpendicular to the glass substrates while particle motion was observed in the horizontal plane.

Particle motion was recorded using a Basler acA640-750um USB3 Vision camera from the ace U series. The camera contains a $1/4''$ ON Semiconductor Python 300 monochrome CMOS sensor with a resolution of 640×480 pixels, a pixel size of $4.8 \times 4.8\mu\mathrm{m}^2$ and a maximum frame rate of 750fps. The camera was mounted via a C mount adapter and operated using the Basler acquisition software, shown on the monitor in Figure 3.1(a). Sinusoidal AC voltages were applied to the ITO electrodes using a Siglent SDG1032X function/arbitrary waveform generator, labelled in Figure 3.1(a). The generator provides two output channels, a maximum sine-wave frequency of 30MHz, a 14-bit vertical resolution, and a maximum output amplitude of $20\mathrm{V_{pp}}$. The voltage amplitude and frequency were adjusted according to the experimental condition required for Janus-particle propulsion or passive-particle assembly. Figure 3.1(b) schematically shows the sample cell geometry. Janus particles were confined between the two ITO-coated glass slides and moved close to the lower electrode. The electric field was applied

normal to the substrates, while the two-dimensional particle trajectories were recorded in the x-y plane.

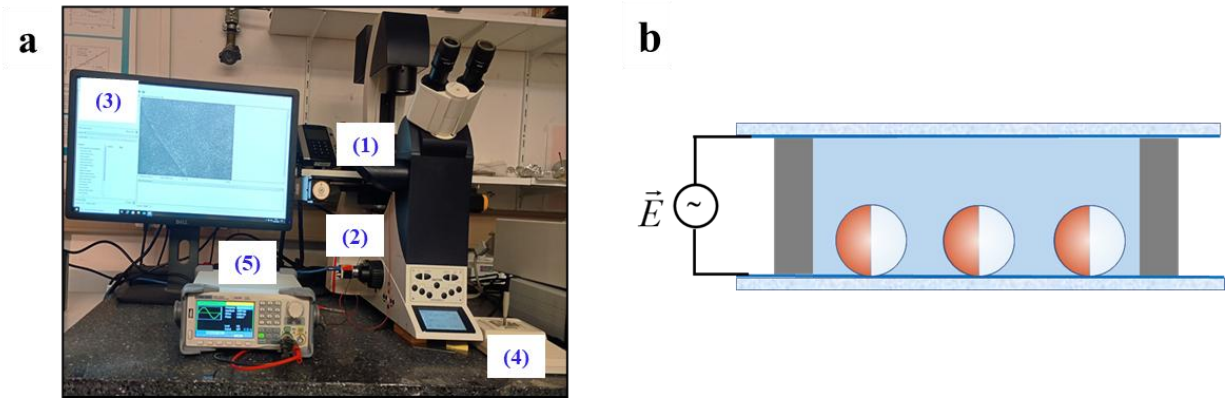

Figure 3.1, (a) Experimental setup used to realize the Janus particles (JPs) driven by alternating electric fields (1) motor stage (2) Basler CMOS camera observes the 2D motion of the JPs (3) software interface from basler to record the 2D motion of the JPs (4) Joy stick allows us to move the motor stage (5) Function generator used to apply the alternating electric field. (b) We sandwich Janus particle between two transparent ITO glasses kept onto a stage.

3.3 Imaging and particle tracking

Particle motion was recorded using a Leica DMI 4000B inverted optical microscope. Depending on the experiment, 10×, 20×, or 40× objectives were used. The 10×objective provided a large field of view of approximately $750\ \mu m \times 750\ \mu m$, which was mainly used for dilute active-particle experiments. The 20× objective provided a smaller field of view of approximately $120\ \mu m \times 120\ \mu m$, which was used for dense or closely packed passive-particle systems. Under such conditions, up to approximately 1080 particles could be observed within one field of view. Images and videos were recorded using a Basler camera and acquired with the Pylon software.

Particle positions were obtained by positional tracking of the recorded image sequences. The tracking procedure followed the established particle-tracking approach introduced by Crocker and Grier [18] and implemented in the TrackPy Python library [204]. This method is widely used for colloidal microscopy because it allows particle centers to be determined with subpixel accuracy from intensity-based image features. Before tracking, raw images were pre-processed by background subtraction and smoothing to improve particle contrast and reduce noise. Particles were then detected based on their apparent size and intensity distribution. Spurious

detections were removed by filtering using parameters such as integrated intensity, particle size and eccentricity.

The detected particle positions were linked into trajectories using the Crocker–Grier linking algorithm. The linking radius was chosen according to the maximum expected displacement between consecutive frames, so that real particle motion was connected while false links were avoided. Only trajectories longer than 250 frames were retained for further analysis, which reduced the influence of short-lived noise detections and particles entering or leaving the field of view.

For dense passive-particle systems, the tracking parameters were optimized separately because particle images were closer together and their intensities were less uniform. In particular, the intensity threshold, particle diameter and minimum separation parameters were adjusted to minimize missed particles and false detections. Dark-field microscopy was used when necessary to enhance contrast and improve tracking reliability in crowded environments. The same general positional-tracking workflow was applied to both active Janus particles and passive colloids. The resulting trajectories were exported as text files and analyzed further using custom MATLAB scripts.

3.3.1 **Particle Orientation and Displacement Direction Extraction**

The displacement direction angle Θ(t), was calculated from the particle trajectory obtained by tracking the particle centroid over time using open-source library TrackPy Python library [204]. For two consecutive particle positions (x_t, y_t) and $(x_{t+\Delta t}, y_{t+\Delta t})$, the displacement vector was defined as,

$$\Delta r(t) = (x_{t+\Delta t} - x_t, y_{t+\Delta t} - y_t) \tag{3.1}$$

and the corresponding displacement direction angle was computed using,

$$\Theta(t) = \tan^{-1}\left(\frac{y_{t+\Delta t} - y_t}{x_{t+\Delta t} - x_t}\right) \tag{3.2}$$

Thus, Θ(t) described the instantaneous direction of translational motion.

Finally, the JPs orientation was determined from recorded microscopy videos using a custom image processing routine implemented in python with the OpenCV library [205]. For each frame, the particle was first identified using blob detection after Gaussian smoothing of the grayscale image. The centroid of the detected blob was used as the particle position.

To determine the particle orientation, a small region surrounding the particle center was cropped from each frame, and the local image gradients were calculated using Sobel operators. The orientation angle was then obtained from the principal axis of the structure tensor as following,

$$\varphi(t) = \frac{1}{2}\tan^{-1}\left(\frac{2S_{xy}}{S_{xx} - S_{yy}}\right) \quad (3.3)$$

Where S_{xx} , S_{yy} , and S_{xy} are the components of the structure tensor constructed from the image gradients. This procedure provides the instantaneous particle orientation angle $\varphi(t)$. The extracted angular time series were subsequently used to calculate the directional and orientational correlation functions described in the following section.

3.4 Janus particle motion characterization

3.4.1 **Mean Square displacement of Janus particle**

Here we extract two key parameters by using mean square displacement (MSD) of the active particles i.e., (1) velocity and (2) Rotational diffusion. It is particularly useful for analysing both passive Brownian motion and active particle behaviour, providing access to key parameters like diffusion coefficients, particle velocity, and reorientation time [22, 28]. We use here use an open-source module Trackpy to compute MSD of the Brownian as well as active Brownian particles [204]. For active particles such as JPs, motion is influenced by both translational and rotational diffusion. Rotational diffusion randomizes the direction of propulsion, affecting their overall trajectory and directional persistence [22]. To make the context consistent with the content of the present thesis, we take the MSD data related to AC field driven Janus particles (JPs). Silica-gold JP (SiO_2-Au) respond to the applied electric field. They sediment onto the bottom wall and self-propel in 2D due to induced-charge electrophoresis (ICEP) [186]. JPs undergo a free two-dimensional active Brownian motion, i.e., they swim at constant velocity v_0 with the SiO_2 hemisphere heading and reorient in 2D with a characteristic timescale τ_R [28]. The free-swimming velocity, v_0, is extracted by calculating MSD from the short-time mean squared displacement and fitting it according to the following Equation 3.4:

$$\mathrm{MSD}(\Delta t) = 4D\Delta t + v_0^2\,\Delta t^2 \quad (3.4)$$

here Δt is the delay time and D is the translational diffusion coefficient of the particles assumed to be 0.089 $\mu m^2/s$ according to the Stokes-Einstein relation. Conversely, the reorientation time, τ_R, is deduced from the full MSD of JPs according to following Equation 3.5:

$$\mathrm{MSD}(\Delta t) = 4D\Delta t + 2v_0^2\,{\tau_R}^2\left(\frac{\Delta t}{\tau_R} - 1 + e^{-\Delta t/\tau_R}\right) \quad (3.5)$$

3.4.2 **Velocity autocorrelation and reorientation time**

The persistence of Janus-particle motion was quantified using the velocity autocorrelation function. From the tracked particle positions, the instantaneous velocity of particle i was calculated as,

$$v_i(t) = \frac{r_i\,(t+\Delta t) - r_i\,(t)}{\Delta t} \quad (3.6)$$

Where Δt is the time interval between two consecutive frames, the velocity autocorrelation is then calculated as,

$$C_{v,i}(\Delta t) = \langle v_i(t+\Delta t).\, v_i(\Delta t)\rangle_t \quad (3.7)$$

Here, the dot denotes the scalar product of the velocity vectors, and $\langle \dots \rangle_t$ denotes averaging over time. This correlation function measures how long the particle keeps memory of its swimming direction. For an ideal active Brownian particle moving with approximately constant speed v_i, the velocity autocorrelation decays as,

$$C_{v,i}(\Delta t) = v_i^2 \exp\left(-\frac{\Delta t}{\tau_i}\right) \quad (3.8)$$

Where τ_i is the reorientation or persistence time of particle i. At short delay times, $\Delta t \ll \tau_i$ this expression is approximated by [206],

$$C_{v,i}(\Delta t) \approx v_i^2\left(1 - \frac{\Delta t}{\tau_i}\right) \quad (3.9)$$

This reorientation time τ_i was obtained from the initial decay of the measured velocity autocorrelation. For each experimental condition, the mean reorientation time τ was calculated by averaging τ_i over approximately 15 active particle trajectories. This approach is useful for comparing how rapidly Janus particles lose directional persistence in different environments. In crowded systems, τ can reduce because of collisions with passive colloids and interactions with local structures, whereas more persistent trajectories correspond to a slower decay of the velocity autocorrelation.

3.4.3 **Directional and Orientational Correlation and Cross correlation Functions to characterize various mode of motion of Janus particles.**

To quantify the temporal persistence of particle motion and orientational dynamics, angular auto-correlation and cross-correlation functions were calculated from the displacement direction angle Θ(t) and particles orientation angle $\varphi(t)$. The displacement direction angle was obtained from the instantaneous trajectory of the particle, while the orientation was extracted independently from image analysis. To characterize the trajectories of JPs in polymer solutions we employed autocorrelation and the cross correlations in the present thesis.

The directional auto correlation function was defined as,

$$C_{\Theta}(\tau) = \langle \cos[\Theta(t+\tau) - \Theta(t)] \rangle \qquad (3.10)$$

Where $\langle \dots \rangle$ Denotes averaging over all time origins t. This function will characterize the persistence of the displacement direction over time. Values close to unity indicate strong directional persistence, whereas values approaching zero correspond to a loss of directional memory.

Similarly, the orientation auto-correlation was calculated as following,

$$C_{\varphi}(\tau) = \langle \cos[\varphi(t+\tau) - \varphi(t)] \rangle \qquad (3.11)$$

Which quantifies the temporal persistence of the particle orientation.

For an ideal active Brownian particle (ABP), the propulsion direction is set by the particle orientation. Therefore, in the absence of strong translational noise, trapping, or external torques, the instantaneous displacement direction is expected to be aligned with the particle orientation at short times. In two dimensions, the orientation correlation decays as $e^{-D_R\tau}$, where D_R is the rotational diffusion coefficient.

However, in the experiments used in this present thesis, the deviations from this ideal ABP expectation are important. In trapped or jittery trajectories, the displacement direction can fluctuate independently of the particle orientation, leading to a weaker or faster decaying cross correlation. Thus, the cross-correlation function is useful for distinguishing persistent propulsion, where displacement and orientation remain coupled, from hindered or jittery motion, where this coupling is partially lost.

The cross-correlation function measures the extent to which the displacement direction remains aligned with the particle orientation over time. The correlation analysis was performed

independently for trapped, jittery and straight-line motion trajectories to characterize the JP's behaviour in polymer suspensions at different activities.

Finally, to examine the coupling between translational motion and particle orientation, the directional orientation cross-correlation function was computed as following,

$$C_{\Theta,\varphi}(\tau) = \langle \cos[\Theta(t+\tau) - \varphi(t)] \rangle \quad (3.12)$$

The cross-correlation function defined here in equation (3.12) measures the extent to which the displacement direction is correlated with the particle orientation in different time regimes. For an ideal freely swimming active Brownian particle, the displacement direction is expected to be aligned with the particle orientation at short times. In contrast, for trapped or jittery trajectories, the displacement direction can fluctuate independently of the particle orientation, leading to a weaker or more rapidly decaying cross-correlation. The correlation analysis was therefore performed separately from trapped, jittery and straight-line trajectories to characterize how the coupling between particle orientation and translation motion changes with activity in polymer suspensions.

3.5 Polymer solutions characterization

The viscosity of the polymer medium was tuned by varying the mass concentration of PEG 6000 in deionized water. Figure 3.2 compares the measured viscosities of the PEG 6000 solutions used in this thesis with literature data reported by Hou et al. for PEG 6000, PEG 8M and glycerol solutions. The data obtained in this work follow the same concentration-dependent trend as the literature values for PEG 6000, confirming that the prepared polymer solutions lie within the expected viscosity range. The observed viscosity increase with increased PEG concentration is found in excellent agreement with the results from the falling ball viscosimeter. Figure 3.2 (a) presents the frequency sweep data for G' and G''. For all concentrations, G'' consistently exceeds G', indicating predominantly viscous behaviour irrespective of frequency. The dynamic viscosity of PEG solutions in Figure 3.2 (b) shows a Newtonian behaviour with constant viscosity at large applied shear rates. The limiting values are 1.44mPas to 8.23mPas for 20mg/mL, to 200mg/mL, respectively. The scatter and upward turn seen towards low applied shear rates is an artifact of the viscosimeter occurring at very low viscosities and resulting from an insufficient torque under these conditions.

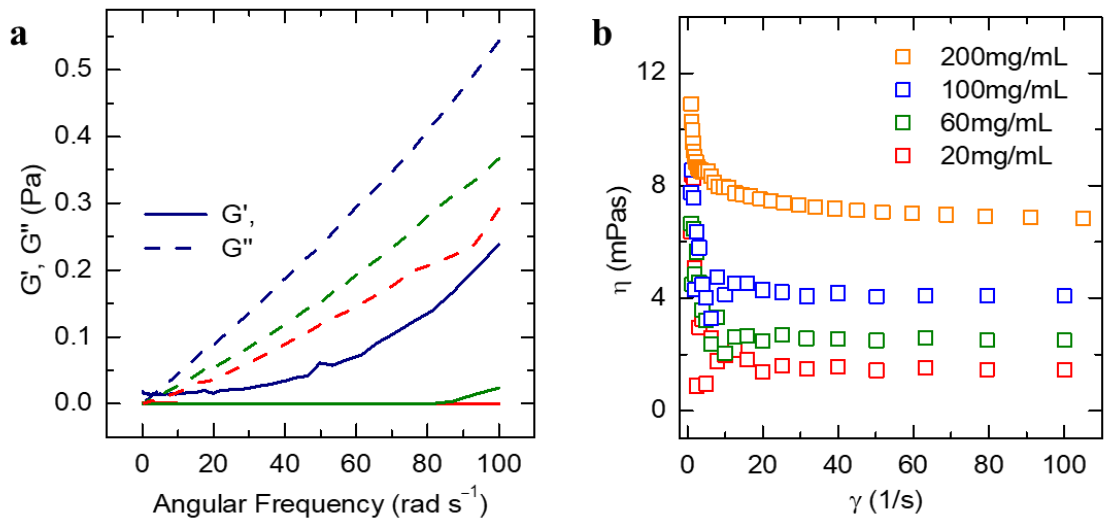

Figure 3.2, (a) Dynamic viscosity, η_{PEG}, of Polyethylene glycol (PEG 6000) dissolved in DI water in dependence on the shear rate. Experiments were performed for different polymer concentrations, as indicated by the key. Obtained results for pure water are included as reference. (b) Loss (G'') and storage moduli (G') of PEG 6000 dissolved in DI water as function of the applied angular frequency. Experiments were performed for different polymer concentrations, as indicated by the key. We consistently observed G'' being greater than G' within the measured frequency range for lower PEG concentrations 20, 60 mg ml^{-1} whereas for 100 mg ml^{-1} values G' dominated G'' at very low angular frequency. Here, we reach the sol-gel transition.

3.6 Passive colloids characterization techniques

3.6.1 **Radia pair correlation function g(r)**

Radial-pair correlation function g(r) is related to the probability of finding other particles at a given distance from a particle of interest. The shape of g(r) can roughly tell us whether our system is in a gas, liquid or solid phase. In the dilute fluid (gas) phase of a hard sphere system, there is no internal structure and all distances are equally possible except below the particle diameter σ_0. The g(r) is zero for $r < \sigma_0$ and equal to one for $r > \sigma_0$. By contrast, for a solid phase in which particles are located only at several possible distances, g(r) shows peaks at those distances and valleys at distances where particles are rarely located [207, 208,]. The definition of g(r) is in the following,

$$g(r) = \frac{1}{\rho N}\frac{1}{2\pi r dr}\sum_i^N \sum_{j\neq 1} \delta(r_{ij}), \qquad (3.13)$$

where ρ is the number density, N is the number of particles in the area of interest, dr is the bin size, r_{ij} is the distance between particle *i* and *j*, *and* δ is a rectangular impulse function such that,

$$\delta\,(r_{ij}) = f(x) = \begin{cases} 1, & \text{if } r < r_{ij} < r + dr \\ 0, & \text{otherwise.} \end{cases} \qquad (3.14)$$

To calculate g(r) from the particle trajectories, we first have to specify a cut-off distance (we use $\sim 2\sigma_0$). For each particle, we search for its nearest neighbours within the specified cut-off distance. Then, we bin the neighbouring distance and normalize each bin by a corresponding area, which is a circumference of a circle of radius r. Finally, we apply the same algorithm for every particle and every frame to obtain the average g(r) at the end (see Figure 3.3).

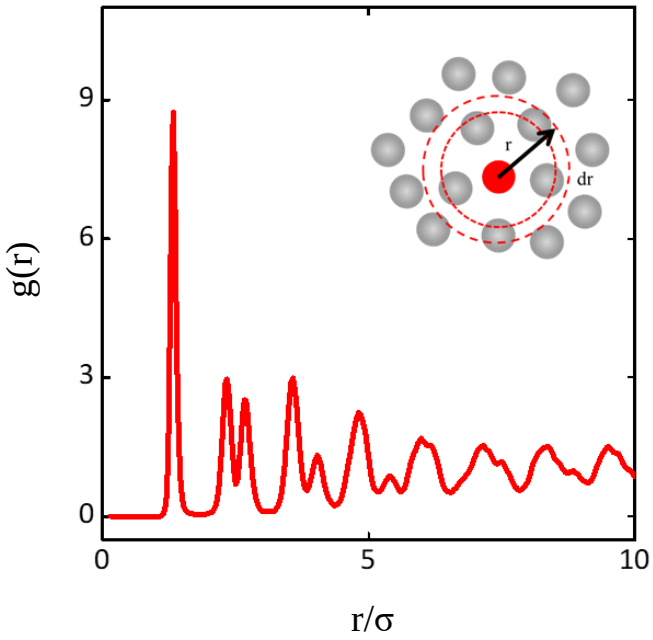

Figure 3.3, Typical example of the pair correlation function g(r) of our dense system of passive colloids. The red curves in figure shows for example the pair correlation functions, g(r), for a monolayer at $\phi = 0.48$ subjected to electric fields at E =108 V/mm, the peaks of g(r) become more pronounced until the second peak between $4R_p$ and $6R_p$ splits, as reported for hexagonal structures. Insect shows Schematic representation of g(r) in simple terms as a measure of probability of finding a particle at a distance of r away from a given reference particle, showed in red colour here for clarity.

3.6.2 **Hexagonal Order parameter**

To understand and quantify the appearance of solid domains in our system, we introduce a parameter called the local hexagonal orientation order parameter, represented as $|\Psi_{6,n}|$. This parameter measures the extent to which the local arrangement of particles around a given particles resembles a perfect hexagonal lattice. The calculation of $|\Psi_{6,n}|$ involves summing contributions from all the neighbouring particles of a given particle n. we consider the absolute value of the orientation hexagonal order parameter per particle and it is mathematically derived as the following [207],

$$|\Psi_{6,\mathrm{n}}| = \frac{1}{\mathrm{N_n}} \left|\sum_{\mathrm{k}} \mathrm{e}^{(\mathrm{i}6\theta_{\mathrm{nk}})}\right| \qquad (3.15)$$

Where N_n is the number of neighbouring particles around the n^{th} particle, the angle θ_{nk} is the angle formed by the bond connecting the n^{th} particles to its k^{th} neighbour relative to a fixed reference direction. Essentially, the values of $|\Psi_{6,n}|$ reflects how well the surrounding neighbours of particles align to form a hexagonal configuration. When the local arrangement is perfectly hexagonal, $|\Psi_{6,n}|$ takes on its maximum value of 1. In contrast, if the arrangement deviates from hexagonal symmetry, the value of $|\Psi_{6,n}|$ decreases accordingly.

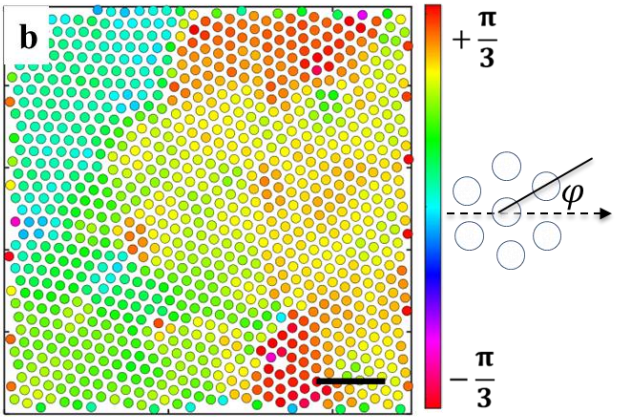

Figure 3.4, Spatial map of particle orientation, illustrating the formation of domains with different orientational alignment. Color bar represents the orientation angle.

We further present the map of the phase φ of $|\Psi_{6,n}|$ for the electric field strength of E=108 V/mm. This map illustrates the orientation of crystalline domains at the highest field strength used in the study. At E=108 V/mm the system achieves a highly ordered state with large, continuous hexagonal domains, as indicated by the uniformity in the orientation represented by the phase φ [298]. The colour map show in Figure 3.4 highlights the alignment

of these domains, where different colours correspond to different orientations. This single field strength was chosen for clarity and because it represents the state of maximum ordering achieved in the system.

3.6.3 **Orientational order correlation**

We employed the dynamical orientational correlation function $g_6(\Delta t)$ to distinguish between loosely packed crystal structures and solid polycrystalline structures, providing a detailed and robust means to analyze and characterize their structural dynamics. This approach allows us to capture the transition from disordered or partially ordered phases to highly ordered and dense polycrystalline phases, offering valuable insights into the underlying dynamics and the degree of order present in the system.

In analogy to how a liquid is differentiated from the hexatic phase in thermal equilibrium, this method enables a quantitative description of the subtle differences in structural organization. For solid polycrystalline structures, complete correlation is consistently observed across the analysed timescales, signifying a high degree of order and stability. Loosely packed crystal structures, however, display a slower decay in correlation, often exhibiting algebraic behaviour. This behaviour indicates intermediate dynamics, where the system demonstrates features of both liquid-like motion and crystalline structure, reflecting a partially ordered or transitioning phase. The correlation function is expressed as following [209],

$$g_6(\Delta t) = \mathrm{Re}\,\langle \frac{\Psi 6(t+\Delta t)\cdot \Psi 6^*(t)}{|\Psi 6^*(t)|^2} \rangle \qquad (3.16)$$

As shown in Figure 3.5, $g_6(\Delta t)$ is presented for voltages ranging from 5 V to 13 V in 2 V increments. At 5 V, the structures exhibit liquid-like characteristics, characterized by weak correlation and rapid decay, reflecting a disordered phase. In contrast, at 13 V, the structures transition to solid polycrystalline, evidenced by strong correlation without decay, signifying a highly ordered and stable phase [208]. This progression illustrates the system's evolution as it responds to external conditions, such as the applied electric field, and transitions between different structural organizations. These observations highlight the role of particle interactions and external conditions in influencing the structural evolution of the system. The correlation function, therefore, serves as a powerful tool for tracing these changes and elucidating the factors driving the transition from loosely packed arrangements to densely packed, solid polycrystalline structures. Through this analysis, we gain a deeper understanding of the interplay between dynamics and structure in such systems.

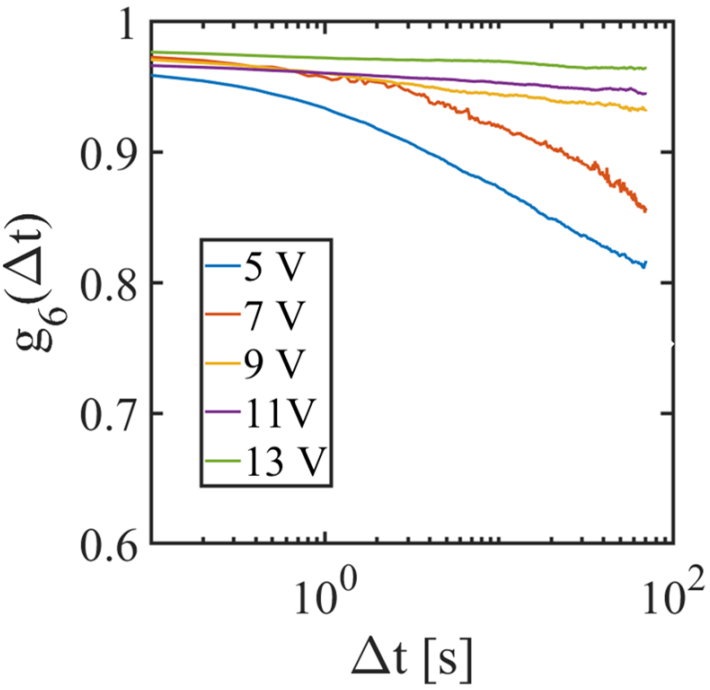

Figure 3.5, Experimental dynamical orientational correlation $g_6(\Delta t)$ as a function of the normalized delay time. Data is presented for voltages ranging from 5 V to 13 V in 2 V increments, as indicated in the legend. At 5 V, the structures exhibit liquid-like characteristics with weak correlation and rapid decay, reflecting a disordered phase. In contrast, at 13 V, the structures are solid polycrystalline, characterized by strong correlation without decay, indicating a highly ordered and stable phase.

3.7 Summary and conclusions

The motivation developed in Chapter 2 requires an experimental platform in which active particles, passive environments and external driving conditions can be controlled reproducibly. This chapter established the technical basis for such a platform. The preparation of PEG 6000 solutions, passive colloidal particles and metallodielectric Janus particles was described, together with the sample cell geometry and AC electric-field setup used for the experiments.

A central requirement is that each component of the system can be characterized independently before combined experiments are performed. The rheological characterization of PEG solutions defines the viscosity range and polymer regimes used to study Janus-particle motion in viscosified polymer environments. The preparation of passive colloidal suspensions provides access to crowded, clustered and ordered environments. The fabrication protocol for gold-coated Janus particles establishes the active component used throughout the thesis.

The chapter also introduced the analysis methods needed to quantify both motion and structure. Positional tracking provides particle trajectories from microscopy videos. Mean-square displacement analysis, velocity autocorrelation and orientational correlations are used to characterize Janus-particle dynamics, while radial pair correlation functions and hexatic order parameters quantify the structure of passive colloidal arrangements. Together, these methods provide the foundation for the following experimental chapters. They define how the relevant control parameters are prepared, measured and analyzed, and therefore make it possible to ask whether electrically driven Janus particles can be used as a reproducible platform for studying active motion in polymeric, crowded and structured environments.

Chapter 4 - **Development of a versatile experimental platform**

4.1 Introduction

This chapter establishes the experimental model system used in the following chapters. The system consists of three components: electrically driven Janus particles, PEG polymer solutions and passive colloidal spheres. Before analysing their combined behavior, each component is characterized separately to demonstrate its suitability and tunability. First, the propulsion behavior of the Janus particles is quantified in the absence of polymer and passive particles. Secondly, the PEG solutions are characterized by their concentration-dependent viscosity and compared with literature expectations. Thirdly, the passive colloidal system is investigated under AC electric fields to determine how its structure can be tuned from clustered island-like arrangements to homogeneous distributions. Finally, the combined active-polymer-passive system is introduced.

4.2 Two-dimensional motion of Janus particles (JPs) without obstacles

4.2.1 **Frequency-Dependent Propulsion and Directional Response**

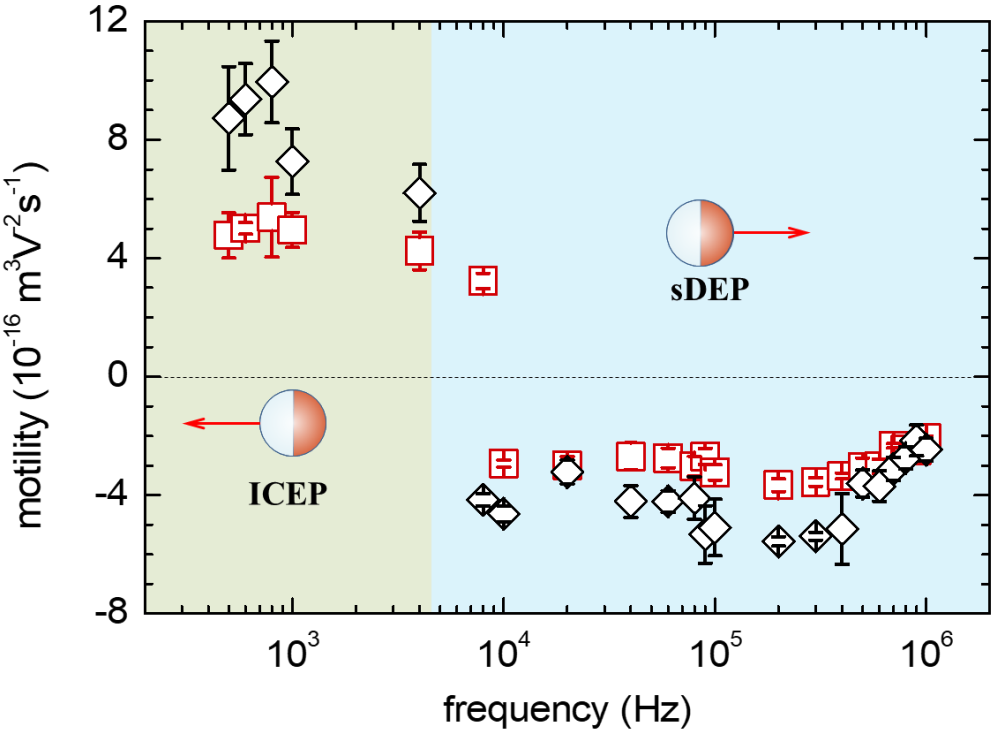

Figure 4.1, The Frequency dependent ICEP mobility of SiO_2-JPs and PS-JPs is characterized in a parallel plate electrode cell with a spacer height of 120µm. The particles are confined between the two electrodes and driven by an AC electricfield of constant amplitude $E = 0.041\ V\mu m^{-1}$, while the frequency is varied. The mobility is defined as v/E^2 and expressed as $m^3V^{-2}s^{-1}$. The light green region indicates the low-frequency ICEP regime, where the particles propel towards the dielectric hemisphere. The cyan region indicates the high-frequency regime where sDEP dominates and the propulsion direction is reversed towards the metal-coated hemisphere. Both particle types show the same general frequency-dependent trend, with slightly different transition frequencies and mobilities. PS-JPs exhibit moderately higher mobilities than SiO_2-JPs over the investigated frequency range, indicating that particle material and surface properties affect the quantitative propulsion response.

The frequency dependent propulsion of SiO_2-JPs and PS-JPs is characterized in a parallel plate electrode cell with a spacer height of 120 µm. The particles are confined between the two electrodes and driven by an AC electricfield of constant amplitude, E=0.041V/µm while the frequency is varied. As shown in Figure 4.1, both 5 µm SiO_2-JPs and 4.5 µm PS-JPs show the same qualitative frequency response, indicating that the observed behaviour is governed primarily by the field induced polarization of the JPs and its interaction with the nearby electrode. However, the transition frequencies and absolute mobilities differ slightly between

the two particle materials, reflecting differences in particle size, dielectric properties, surface charge and near wall interactions.

Two main frequency-dependent propulsion regions are identified, as indicated by the coloured regions in Figure 4.1. In the light green region, corresponding to low frequencies around 1 kHz, the particles move by induced-charge electrophoresis (ICEP). In this regime, the AC field charges the metallic hemisphere and generates asymmetric electro-osmotic flow around the particle, resulting in propulsion towards the dielectric side [182, 184, 186, 187, 210,].

At higher frequencies, shown by the cyan region, the propulsion direction reverses and the particles move towards the metal coated side. Historically, this reversal was first discussed in terms of reversed ICEP (r-ICEP) [35, 37,]. However, following more recent interpretations, the high-frequency motion is more consistent assigned to self-dielectrophoretic propulsion (sDEP), where the metallic and dielectric hemispheres polarize differently and generate local electricfield gradients near the electrode [188,189].

In this interpretation, sDEP becomes dominant in the frequency range where the ICEP contribution weakens and the field induced dielectrophoretic interaction takes over [188, 189, 211,]. The interaction with these self-generated electric-field gradients drives the particle towards the metal-coated side. Overall, the observed transition from low-frequency ICEP to high-frequency sDEP is consistent with previously reported frequency-dependent propulsion behaviour of metallo-dielectric Janus particles. Therefore, Figure 4.1 provides the operating frequency windows used to select the propulsion mode in the following experiments.

4.2.2 **Field-Strength-Dependent Propulsion at Fixed AC Frequency.**

As SiO_2 based JPs are the main active component used in this thesis, their free-swimming behavior is first characterized in the absence of passive obstacles. SiO_2-JPs sediment close to the bottom electrode and move quasi two dimensionally under an applied AC electric field. In this frequency range, propulsion is driven by induced-charge electrophoresis (ICEP) [186, 187,], while dielectrophoretic interactions keep the particle orientation approximately parallel to the substrate. Under these conditions, the particles perform active Brownian particle-type motion, characterized by a propulsion velocity v_0 and a reorientation time τ_R.

The propulsion velocity is extracted from the short time mean square displacement (MSD), shown in Figure 4.2(a), by fitting the active Brownian model introduced in Chapter 3 (§3.4.1). As shown in Figure 4.2(b), v_0 increases linearly with the squared electric field strength, E^2,

consistent with the ICEP propulsion mechanism. From a linear fit, a mobility of $7 \times 10^{-2} V^{-2}\,\mu m^3 s^{-1}$ is obtained. The reorientation time τ_R of JPs is determined from the full MSD is shown in Figure 4.2(c). The reorientation is independent of v_0 and remains close to to $D_R^{-1} = 95$ s, as expected from the Stokes-Einstein rotational diffusion coefficient. We obtain swimming velocities between 1 and 5 μm/s, which correspond to persistence lengths ($L_R = v_0 \cdot \tau_R$ – the typical length of straight paths) between 100 and 500 μm.

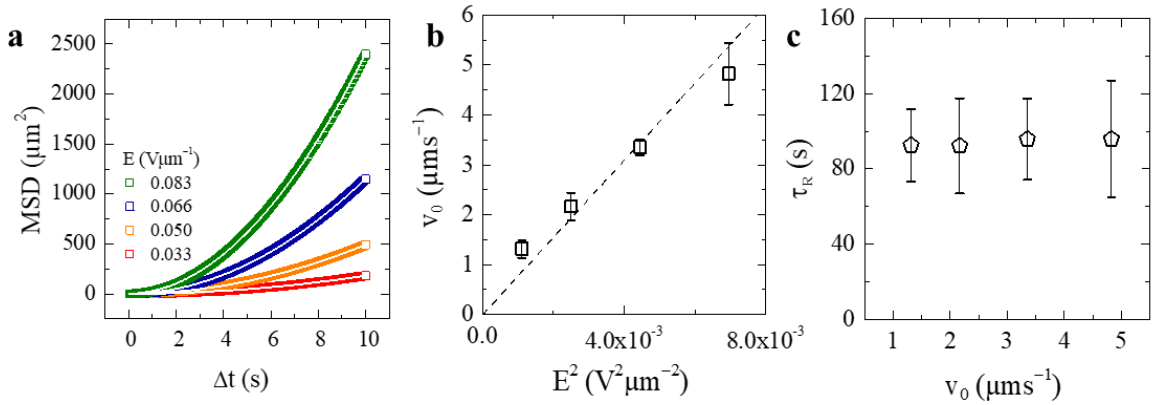

Figure 4.2, Two-dimensional active Brownian motion of silica-gold JPs without obstacles. (a) Short time mean squared displacement (MSD) of JP for increasing values of electric field (indicated in the legend) and frequency f = 1.5 kHz. The solid lines are least-squares fits of the data based on Equation (3.1). (b) Corresponding particle velocity, v_0, plotted against the squared electric-field strength. The dashed line is a least-squares linear fit to the data with a slope of approximately 7×10^{-2} $V^{-2}\mu m^3 s^{-1}$. (c) Characteristic reorientation time, τ_R, of JP moving in 2D as a function of v_0. The data are an average over 9 – 10 individual particles. The error bars denote the standard deviation.

4.3 Tuning Complex and Crowded Environments: Polymer viscosity and passive colloidal structure

4.3.1 **Complex environment tuning using polymer concentration**

he polymer medium used in this work is characterized by measuring the viscosity of PEG6000 solutions as a function of polymer mass concentration. Figure 4.3 compares these measurements with literature data from Hou *et al.* [212]. The pink data points show the PEG6000 solutions prepared in this work, while the blue curve corresponds to the reported PEG6000 data. Water is included as a reference baseline, corresponding to the polymer-free solvent. The agreement between the present measurements and the literature values confirms that the prepared PEG6000 solutions follow the expected concentration-dependent viscosity trend.

The comparison with glycerol and high-molecular-weight PEG further illustrates why PEG6000 is suitable for this study. Glycerol produces only a weak increase in viscosity over the same concentration range because it is a small-molecule viscosifier. In contrast, PEG 8M shows a much stronger viscosity increase already at very low concentrations, reflecting the strong molecular-weight dependence of polymer solution viscosity. Here, PEG 8M refers to a very high molecular weight PEG and should not be confused with PEG8000. PEG6000 lies between these two limiting cases and therefore provides a convenient viscosity range for tuning the polymeric environment without reaching extremely high viscosities.

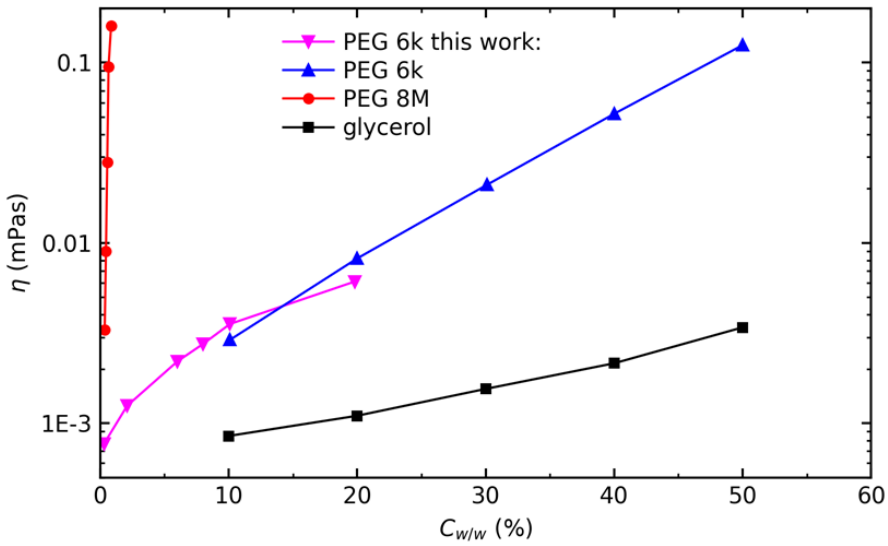

Figure 4.3, Concentration dependent viscosity of Poly Ethylene Glycol (PEG) 6000 solutions used in this work compared with literature data from Hou et al. for PEG 6000, PEG 8M and glycerol solutions. The viscosity η is plotted as a function of polymer or solute mass concentration $c_{w/w}$. The PEG 6000 measurements from the present work follows the same trend as the reported PEG6000 data, conforming that the prepared polymer solutions lie within the expected viscosity range. Compared with glycerol, PEG 6000 produces stronger viscosity at comparable mass concentration, while PEG 8M shows a much steeper increase due to its higher molecular weight. This comparison establishes PEG 6000 as a suitable polymeric medium for systematically tuning viscosity in the active-particle experiments.

The viscosity is plotted on a logarithmic scale to highlight the large differences between small-molecule and polymeric viscosity modifiers. Overall, Figure 4.3 shows that the PEG6000 solutions used in this work are reproducible and consistent with literature expectations. The selected PEG6000 concentrations provide viscosities that are sufficiently different to influence particle motion, while still allowing electrically driven Janus particles to remain mobile under appropriate field conditions.

4.3.2 **Formation of Island Structures by AC fields.**

The passive colloidal samples are prepared according to the protocol described in Section 3.2.1. Here, uncoated silica particles with radius $R_p = 1.15\mu m$ are used as passive obstacles for $5.02\mu m$ silica gold Janus particles. Figure 4.4 first establishes how these passive particles behave in the absence and presence of an applied AC electric field.

In the absence of an electric field, the passive silica particles remain dispersed and undergo Brownian motion, as shown in Figure 4.4(b). This dispersed state is also reflected in the radial distribution function, g(r), shown in Figure 4.4(d). For E=0, the first peak of g(r) appears at interparticle distances larger than $2R_p$, indicating that the particles do not remain in direct contact and that the effective interaction between the passive silica colloids is predominantly repulsive. This behaviour is consistent with a stable Brownian suspension in which electrostatic repulsion prevents close packing.

When a vertical AC electric field is applied, $f = 1.5kHz$ and $E = 0.083\,V\,\mu m^{-1}$, the same particles assemble into close packed islands at and area fraction $\phi = 0.42$, as shown in Figure 4.4(c). Under the applied field, the radial distribution function develops sharp and regularly spaced peaks, indicating the emergence of local crystalline order within the islands. In particular, the first maximum g(r) shifts close to $r \approx 2R_p$, showing that the particles are brought into near contact. This confirms that the field induced attraction overcomes the electrostatic repulsion present in the free state without any field being applied (**see supplementary video 1**).

The formation of these colloidal islands is attributed to electrohydrodynamic interactions induced by the AC electric field. The applied field polarizes the silica particles and drives electroosmotic flows along the conductive substrate through the electric double layer. These flows generate effective long-range particle-particle attractions, leading to the formation of dense, locally ordered colloidal islands [200,201,202] (see Figure4.4(a)). If the field is switched off, the islands 'dissolve' and the fluid phase is slowly recovered by thermal diffusion (**see supplementary video 2**)

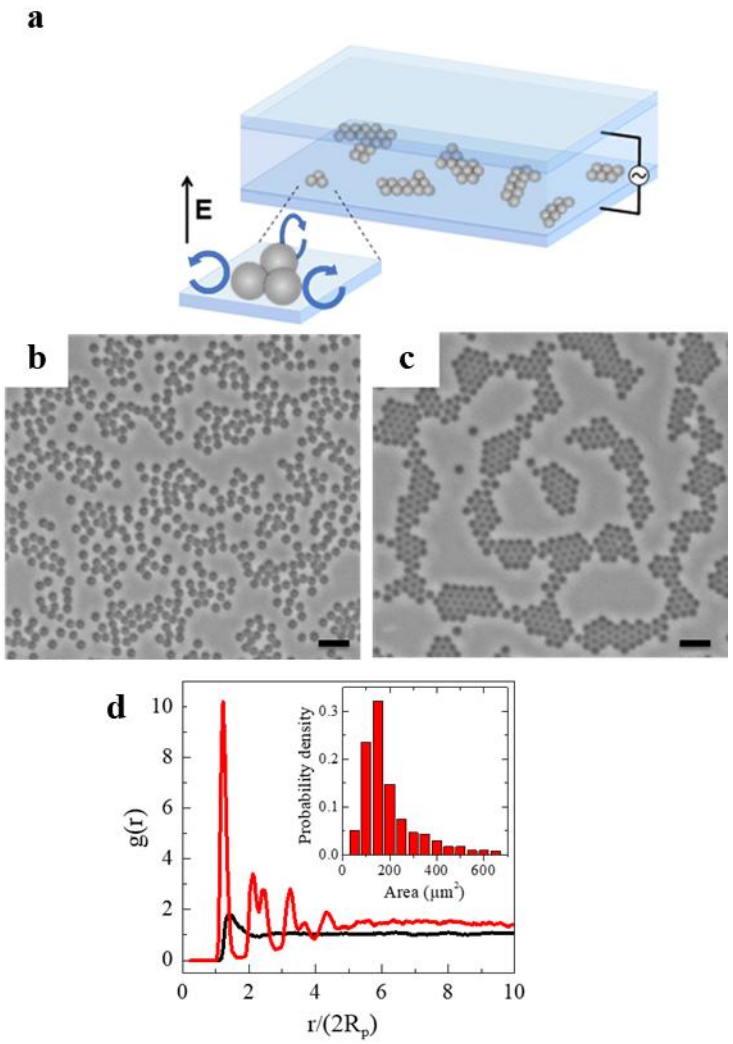

Figure 4.4, Assembly of 'passive' silica microspheres under AC electric fields. (a) Schematic of the experimental setup, showing silica particles confined between two electrodes and the electrohydrodynamic flows that lead to mutual particle attraction. (b) Microscopic image of silica passive particles (R_p=1.15 μm) in an aqueous medium without electricfield, where the particles undergo Brownian motion and remain dispersed. (c) Microscopic image of the same particles under a vertically applied AC electricfield (f =1.5kHz, E=0.083 V/ μm). Under these conditions, field-induced electrodynamic attractions lead to the formation of the close packed particle islands. The scale bar corresponds to 10 μm. (d) Radial distribution function g(r) plotted as a function of the normalized interparticle distance for E = 0 (black solid line) and E = 0.083 V/μm (red solid line). Inset: Probability density distribution of the area of the islands for E = 0.083 V/μm.

Overall, Figure 4.4 demonstrates that the passive silica suspension can be reversibly switched from a dispersed Brownian state to a clustered, locally ordered state by applying an AC electric field. As ϕ increases, the passive phase changes continuously from isolated compact islands at

low packing fraction, to connected structures with fjord-like voids at intermediate packing fraction, and finally to dense networks in which only isolated holes remain. These field-induced colloidal islands provide a tunable passive obstacle matrix for studying the interaction between active Janus particles and structured colloidal environments in the following chapter.

4.3.3 **Tuning the structure of the polycrystalline environment**

Here, the passive colloidal environment is characterized as a tunable polycrystalline component of the experimental platform. The samples consist of silica microsphere ($R_P = 1.46\,\mu m$) dispersed in water and sedimented onto a planar electrode. The packing fraction ϕ, is defined as the relative area occupied by the particles in the observed plane, is varied between $\phi = 0.15$ and $\phi = 0.64$. An AC electricfield is applied perpendicular to the observation plane at a fixed frequency f = 20kHz, with field strength between E=0 and 108V/mm. These field strengths are chosen such that the particles remain confined to a monolayer and do not form a second layer.

In the absence of an electric field, the silica particles are weakly repulsive due to their negatively charged surfaces and undergo Brownian motion within the monolayer. When the AC electricfield is applied, the particles become polarized and interact through a long-range dipole-dipole repulsion [139,203]. At $f = 20$kHz, this interaction scales approximately with E^2 and decays with the interparticle distance as r^{-3}. The electricfield therefore increases the effective particle size and provides a way to tune the microstructure of the passive colloidal environment without changing the packing fraction.

To compare the experiments with simulations, the passive matrix is modelled as a two-dimensional Brownian system with negligible hydrodynamic interactions. The particles interact through excluded-volume interactions, represented by a WCA potential, and a long-range dipolar repulsion that mimics the field-induced interactions between silica microspheres. The potential parameters are chosen by matching the peaks of the experimental and numerical pair correlation function g(r), calculated as described in Chapter 3, for each value of E and ϕ. The structural evolution is first illustrated for ϕ =0.48. Figure 4.5(a) shows the experimental pair correlation function together with the numerical results for different electric field strengths. With increasing E, the peaks in g(r) become more pronounced, indicating enhanced positional order. At the largest field strength, E=108V/mm, the second peak between $4R_P$ and $6R_P$ splits, which is characteristic of hexagonal ordering. This field induced ordering is quantified by the global bond-orientational parameter $|\Psi_6|$, shown in Figure 4.5(b). The monotonic increase of $|\Psi_6|$ with E confirms that the applied field promotes the formation of locally ordered domains.

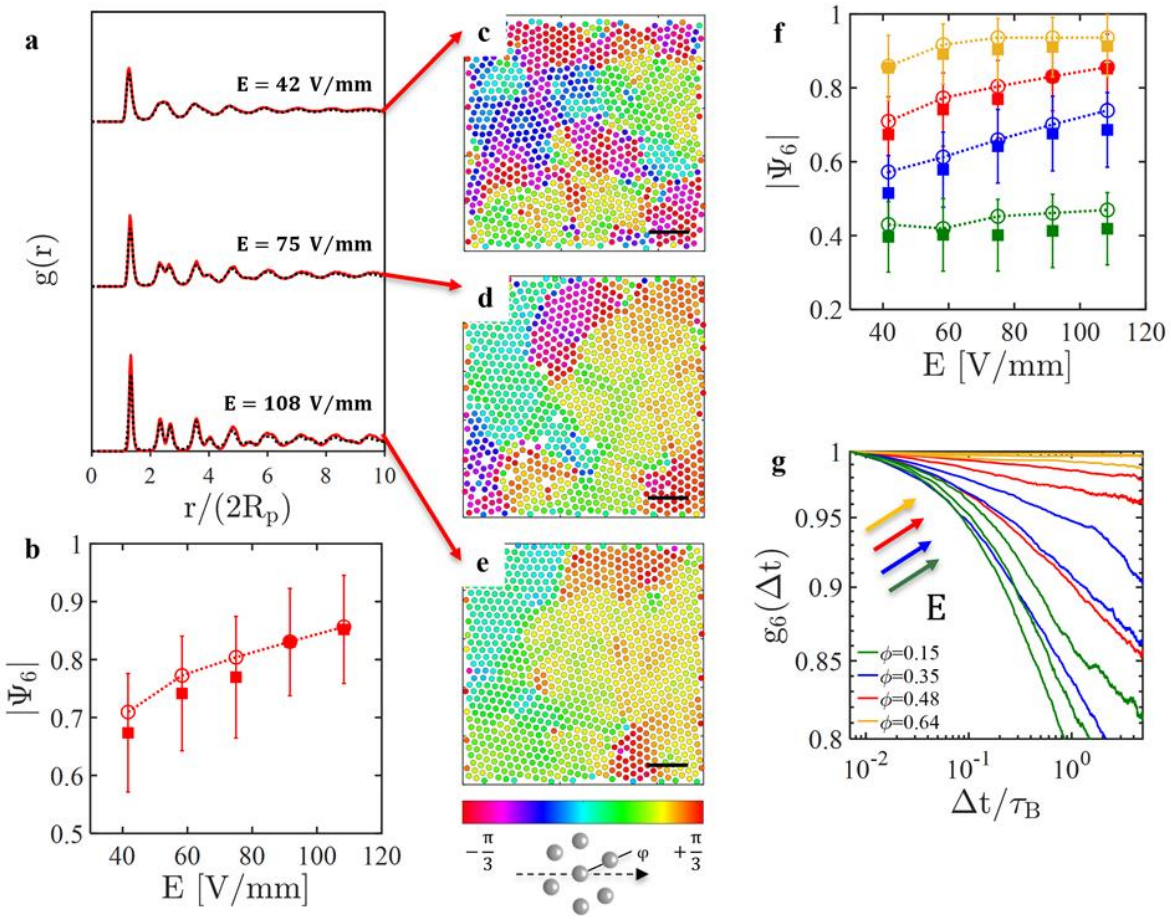

Figure 4.5, Tuning the structure of the environment. (a) Experimental pair correlation functions g(r) (red solid line) and numerical (black dashed line) at ϕ = 0.48 for different electric fields. (b) Mean hexagonal order parameter $|\Psi_6|$ versus field strength in experiments (solid symbols) and simulations (empty symbols and dashed connecting line) at ϕ = 0.48. (c–e) Experimental maps of the phase φ of $\Psi_{6,n}$ at E = 42 V/mm, E = 75 V/mm, and E = 108 V/mm. The scale bar is 20 µm and the colours denote the crystalline orientations as sketched in the bottom-right inset. (f) $|\Psi_6|$ plotted as a function of the electric-field strength E for colloidal monolayers with packing fractions ϕ = 0.15 (green), ϕ = 0.35 (blue), ϕ = 0.48 (red), and ϕ = 0.64 (orange). Filled and empty symbols correspond to experimental and numerical results, respectively. (g) Experimental dynamical orientational correlation $g_6(\Delta t)$ as a function of the normalized delay time $\Delta t/\tau_B$ for different packing fractions (according to same colour code as in (f)) and electric fields. For clarity, only the curves at E = 48 V/mm, E = 75 V/mm, and E = 108 V/mm are shown. At all ϕ, the decay of $g_6(\Delta t)$ becomes slower for larger electric fields, as indicated schematically by the arrows.

The spatial development of these domains is shown in Figure 4.5(c-e), where the phase φ of the local order parameter $\Psi_{6,n}$ represent the orientation of local crystalline regions. At lower field strength, only small ordered regions are visible. With increasing E, these regions merge into

larger hexagonal domains, demonstrating that the electric field can quench the monolayer into more ordered configurations. The same evolution is shown dynamically in **supplementary video 3,** where the electricfield is progressively increased from E=0 to 108V/mm.

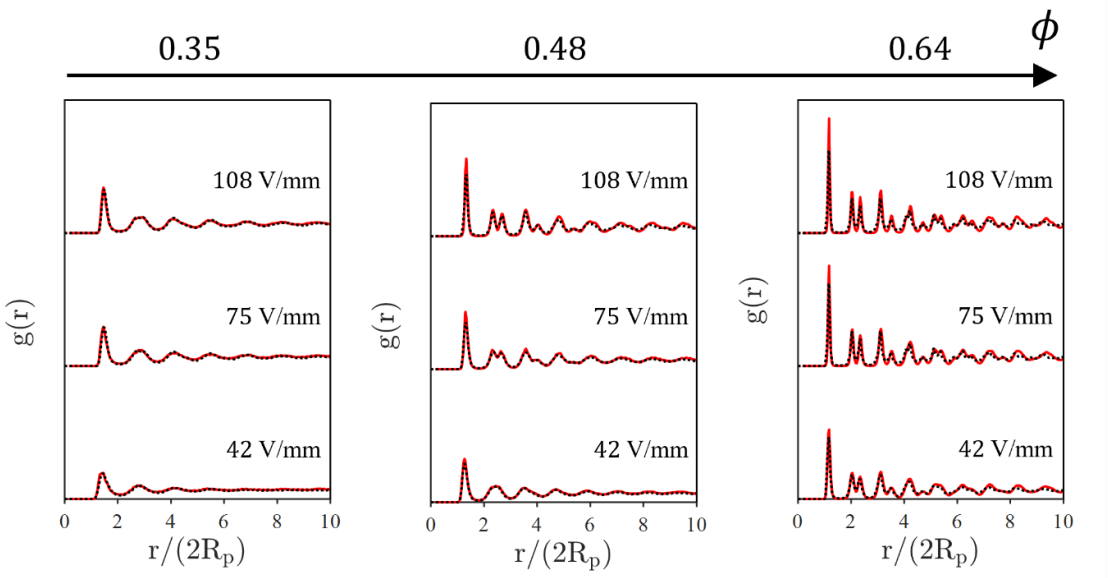

Figure 4.6, Experimental (red curves) and numerical (dashed black lines) pair correlation functions, g(r) of passive colloidal monolayers at different area fraction (ϕ, see arrow) and subjected to various electricfields (E, indicated in the graphs). The radial distance is normalized

The field-induced structural tuning is observed over a broad range of packing fractions. Figure 4.5(f) shows $|\Psi_6|$ as a function of E for ϕ = 0.15, 0.35, 0.48, and 0.64. In all cases, the orientational order increases with field strength, although the response depends on ϕ. t low packing fraction, stronger fields are required to induce pronounced ordering because the particles are farther apart. At the highest packing fraction, the increase of $|\Psi_6|$ saturates, indicating that the monolayer is already close to a highly ordered configuration. As a further conformation, Figure 4.5(g) shows the dynamical orientational correlation as function of delay time normalized by Brownian diffusion time. At $\phi = 0.64$ (orange data), $g_6(\Delta t)$ decays at a rate that depends on both E and ϕ. Interestingly, similar decays are recovered with different packing fractions and electric fields, in agreement with the measurement of $|\Psi_6|$. This demonstrates that the electricfield can be used as a tool to create optimally ordered configurations without changing the packing fraction.

The corresponding pair correlation functions and local phase maps are provided in Figure 4.6 and Figure 4.7, respectively. Figure 4.6 shows the pair correlation function, g(r), for different area fractions and electric field strengths. At low field strength, the peaks in g(r) are weak and

broad, indicating that the particles remain relatively disordered and that only short-range positional correlations are present. As the electric field strength increases, the peaks become sharper and more pronounced. This indicates that the particles develop stronger positional order and that the average interparticle spacing becomes better defined. The effect is particularly clear at higher area fractions, where the particles are already close enough for field-induced dipolar interactions to efficiently reorganize the monolayer. Therefore, Figure 4.6 provides a quantitative measure of how the applied electric field controls the positional structure of the passive matrix.

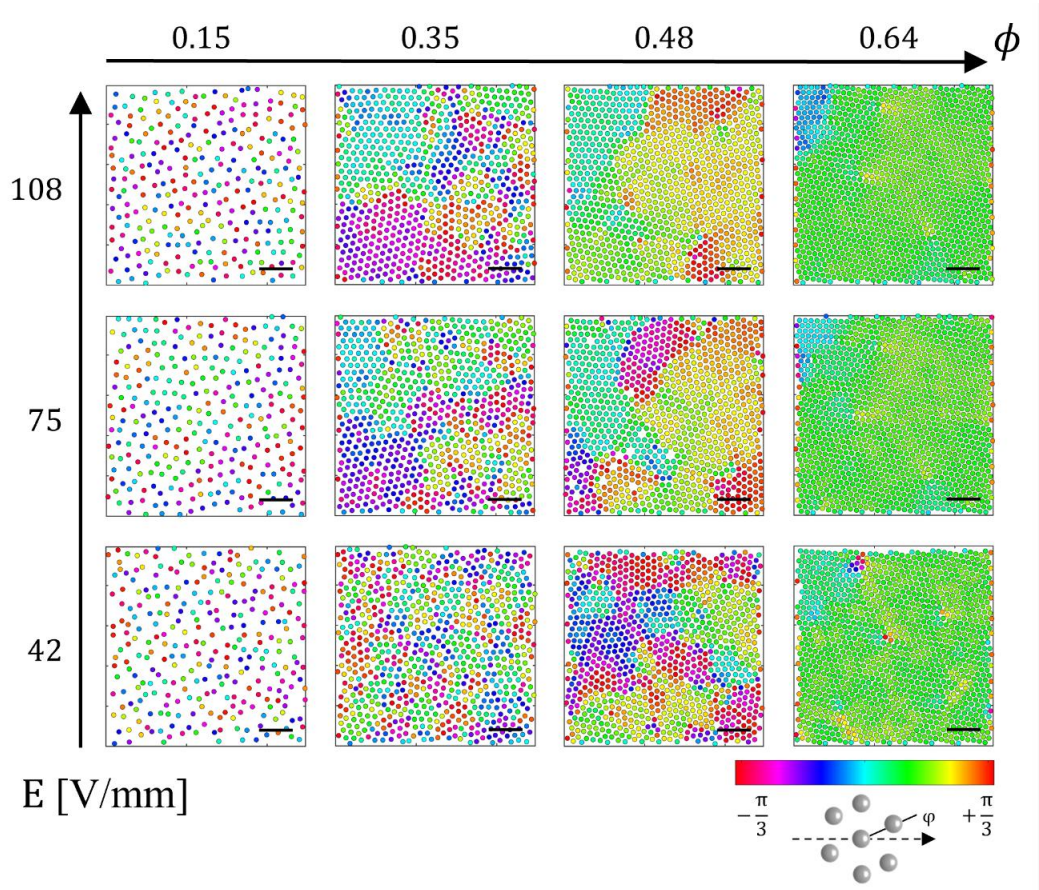

Figure 4.7, Maps of the phase φ of the local hexagonal order parameter $\Psi_{6,n}$ (where n is the particle label) corresponding to the last experimental frame of videos of passive colloidal monolayers at different area fraction (ϕ, see horizontal arrow) and subjected to various electric fields (E, see vertical arrow). The scale bar is 20 µm.

Figure 4.7 complements this analysis by showing maps of the local hexagonal bond-orientational order parameter, $\Psi_{6,n}$. The colours represent the local orientation of hexagonally ordered domains. At low area fraction and low field strength, only small and randomly oriented ordered regions are observed, indicating a mostly disordered monolayer. With increasing field strength and packing fraction, these ordered regions grow and merge into larger domains. This

shows that the electric field not only increases local particle correlations, but also promotes the formation of extended polycrystalline regions. The colour variations between neighbouring domains indicate that the matrix is not a single crystal, but a polycrystalline structure composed of locally ordered grains with different orientations.

4.3.4 **Frequency dependent active–passive interactions**

In addition to controlling the propulsion mode of individual Janus particles and the structure of passive silica monolayers, the applied AC electric field also controls the interaction between active Janus particles and passive silica particles. This frequency-dependent active–passive interaction is important for the experiments discussed in later chapters, because it provides the basis for cargo pickup and release, load-free return, and reorientation events at passive silica islands.

The interaction depends on frequency because the silica hemisphere, the metallic cap, and the passive silica particles polarize differently under the applied AC field. Passive silica particles polarize under the field and can interact with each other through induced dipole–dipole repulsion, which helps define the spacing and structure of the passive monolayer. At high frequencies, where sDEP dominates, passive silica particles can be attracted towards the metallic side of the JP, enabling cargo attachment and transport [199]. Thus, the same applied field can generate repulsive interactions between passive silica particles, while also producing an asymmetric attractive interaction between a passive particle and the metallic cap of a JP.

The same frequency dependent interaction is also relevant when JPs collide with passive silica islands. Local electric-field gradients near the island boundary can generate torques on the JP, especially through interactions involving the metallic cap. These torques can reorient the particle during contact and lead to undocking or backscattering. However, the outcome depends on the local island geometry and the orientation of the JP. Therefore, the JP may either reorient and escape, glide along the island boundary, or become temporarily trapped.

Thus, the AC field does not only tune JP propulsion and passive-particle assembly, but also controls how active and passive components interact with one another. This coupling completes the characterization of the experimental platform and motivates the cargo transport and island-hopping studies presented in the following chapters.

4.4 Demonstration of Active Colloid Motion in Tunable Complex Environments

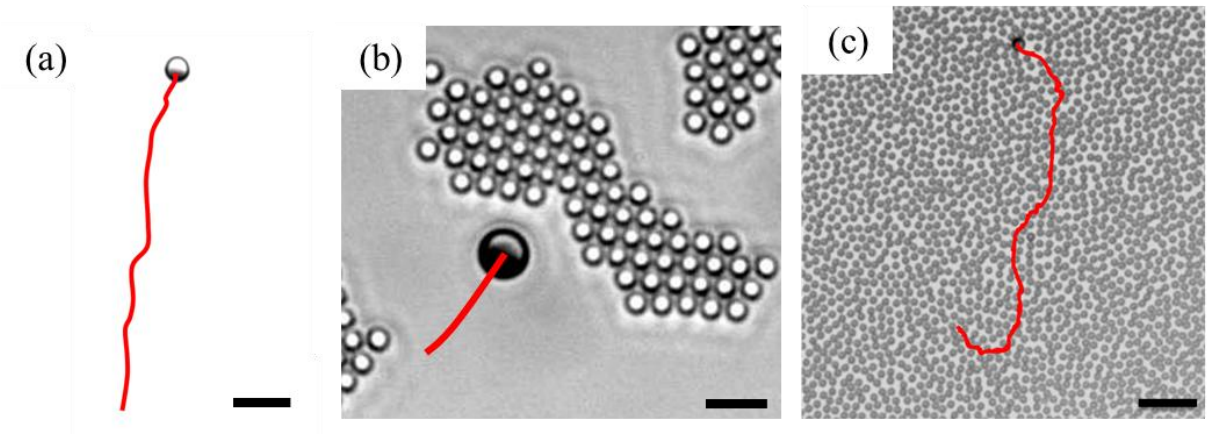

Figure 4.8, Demonstration of active colloid motion in the tunable experimental environments established in this chapter. Representative trajectories show electrically driven Janus particles moving in three different model systems: (a) viscosified polymer medium consisting of PEG 6000 solution with $\eta = 4\text{mPas}$, driven at $f = 4\text{kHz}$ and $E = 0.133\ \text{V}\mu m^{-1}$. (b) JPs moving in the presence of passive silica spheres assembled into field induced clusters, with $E = 0.083\ \text{V}\mu m^{-1}$, and (c) JPs cruising through a colloidal monolayer of Brownian microspheres driven at $f = 20\text{kHz}$ and $E = 0.042\ \text{V}\mu m^{-1}$. These examples demonstrate how the individually characterized components, namely JPs, PEG polymer solutions, and passive silica colloids, can be combined to generate complex and crowded environments for active passive experiments. The figure summarizes the versatility of the experimental platform and motivates the detailed studies presented in the following chapters. The scale bar is 10µm (a, b) and 30 µm in (c).

Having characterized the individual components of the experimental platform, the next step is to demonstrate how they can be combined to generate different complex and crowded environments for Janus particles (JPs) motion. Figure 4.8 summarizes three representative configurations that will be investigated in detail in the following chapters. The purpose of this figure is not to provide a complete analysis of each system, but to show that electrically driven Janus particles can be operated in viscosified polymeric media, field-induced island-like structures, and polycrystalline passive environments.

First, active SiO_2 Janus particles with a diameter 5µm are introduced into viscosified PEG 6000 solutions of controlled viscosity $\eta = 4\text{mPas}$, see Figure 4.8(a). In this case, the polymer concentration sets the viscous and polymer-mediated resistance experienced by the swimmer. The applied AC electric field of $E = 0.133\ \text{V}\mu m^{-1}, f = 4\text{kHZ}$ provides an external control parameter for the activity of the JPs. This configuration forms the basis of Chapter 5, where the

interplay between field-driven propulsion and PEG-induced hindrance is analyzed systematically.

Secondly, SiO_2-JPs with a diameter 5µm are placed into passive colloidal environments where silica particles with a diameter 2.31µm assemble into island-like structures under AC fields, see Figure 4.8(b). This combines two field-induced processes: the electrohydrodynamic assembly of passive silica spheres into dense islands and the ICEP-driven propulsion of the active JP. The resulting system provides a controlled obstacle landscape, in which the active particle moves through free regions and interacts with the boundaries of passive clusters. This configuration is used later to study active motion in crowded island-like environments.

Finally, SiO_2-JPs with a diameter 5µm are introduced into tunable polycrystalline passive matrices of diameter 2.82µm, see Figure 4.8(c). In contrast to isolated islands, these matrices provide a more continuous crowded environment whose structure and temporal persistence can be tuned by the applied electric field and packing fraction. This makes it possible to study how active particles move through passive environments with controlled structural order and effective resistance, as demonstrated in detail in the following chapter**.**

Together, Figure 4.8 demonstrates the versatility of the developed experimental platform. The Janus particles provide externally tunable activity, the PEG solutions provide a controllable polymeric medium, and the passive silica colloids provide adjustable crowded structures. By combining these components, the system enables systematic studies of active colloid dynamics in environments of increasing complexity, which are addressed in the following chapters.

4.5 Selection of Representative Experimental Conditions

The results presented above show that the experimental platform provides several independent control parameters. The activity of the Janus particle can be tuned by electric field strength and frequency, the PEG concentration controls the viscosity of the polymeric medium, and passive silica particles can be assembled into different crowded structures using AC electric fields. In principle, this creates a large parameter space involving swimmer type, propulsion mode, polymer concentration, passive particle density and field parameters. However, the aim of the following experiments is not to exhaustively explore this entire parameter space. Instead, three representative frequency regimes are selected because they correspond to qualitatively different physical situations for the motion of Janus particles in complex environments.

First, the low-frequency regime 1 kHz is chosen because the Janus particles move by induced-charge electrophoresis (ICEP) toward the dielectric hemisphere. In this regime, passive silica particles can form island-like structures, providing a crowded but spatially heterogeneous obstacle landscape for active motion. Second, the intermediate-frequency regime around 20 kHz is selected because it allows the passive colloidal environment to be tuned into polycrystalline structures. This regime is therefore useful for studying JPs motion in a more continuous crowded matrix with adjustable structural order and persistence. Third, the high-frequency regime around 250kHz is chosen because Janus particles operate in the self-dielectrophoretic (sDEP) regime. This frequency is particularly relevant for cargo transport, since the same AC field can drive JP motion and induce attractive dipolar interactions between the JP and passive cargo particles.

The selected conditions are therefore not arbitrary. They represent experimentally accessible and physically distinct situations that build on each other. First, JPs dynamics in PEG solutions are studied to understand how polymer induced viscosity and surface interactions affect active motion of JPs. This knowledge is then used to identify field conditions under which directed propulsion is recovered in polymeric media. These high-field conditions provide the basis for developing a cargo pickup, transport, and release mechanism in polymer suspensions. In parallel, JPs motion is also demonstrated in island like colloidal clusters and tunable polycrystalline matrices, which represent two controlled crowded environments. Together, this reduced set of cases captures the main functionalities of the versatile experimental platform developed here while keeping the experiments systematic and interpretable.

4.6 Conclusion

This chapter established the experimental platform used to investigate electric-field-driven active colloids in complex and crowded environments. The platform consists of three independently tunable components: active Janus particles (JPs), PEG polymer solutions and passive silica colloids. Each component was characterized separately before demonstrating how they can be combined to create controlled model environments for the experiments presented in the following chapters**.**

First, the motion of Janus particles in pure solvent was characterized. Both SiO_2 and PS-based JPs exhibit field-driven propulsion under AC electric fields, with mobilities that depend on field strength and frequency. The frequency-dependent measurements identified the relevant

propulsion regimes, including ICEP, rICEP and sDEP. This establishes the Janus particles as externally tunable swimmers, for which both propulsion strength and direction can be controlled by the applied electric field**.** Second, PEG6000 solutions were characterized as tunable polymeric environments. The measured concentration dependent viscosities agree with literature expectations and confirm that PEG6000 provides a reproducible way to adjust the viscous resistance experienced by the particles. This polymeric component is therefore suitable for investigating how active motion changes in complex media with controlled viscosity. Third, passive silica colloids were established as tunable crowded environments. Under AC electric fields, passive particles can form island-like structures or more homogeneous polycrystalline matrices, depending on field conditions and packing fraction. The structural and dynamical analysis shows that the passive matrix can be tuned from a more fluid-like dispersed state to a more ordered and persistent environment.

Finally, representative combined systems were demonstrated. JPs were demonstrated to move in PEG solutions, through island-like passive structures and within polycrystalline colloidal matrices. These demonstrations show that the three components can be combined in a controlled way to generate different model environments. The selected cases are therefore not arbitrary, but represent experimentally accessible situations that address different aspects of active motion: polymer-induced hindrance, obstacle-mediated dynamics, and motion in crowded structured matrices.

Overall, this chapter provides the necessary foundation for the following results chapters. Chapter 5 uses the PEG-based platform to study how polymer concentration and electric field strength affect Janus particle motion. The knowledge gained from these experiments is then used to develop a cargo transport strategy based on the self-dielectrophoretic mechanism. The crowded passive-particle environments introduced here further provide controlled systems for studying active motion in structured obstacle landscapes.

Chapter 5 - **Ac field driven active colloids dynamics in polymer solution**

5.1 Introduction

Polymer solutions provide a controlled way to modify the environment of active colloids. Depending on polymer concentration and molar mass, they can increase the viscosity of the suspending medium, introduce polymer-induced interactions, and, at higher concentrations, create microstructural constraints or viscoelastic effects. Previous studies have shown that polymeric media can strongly influence microswimmer dynamics, including propulsion speed, orientational persistence, rotational diffusion, and even the onset or suppression of active motion [190,191,192,]. However, most studies have focused on chemically or light-driven swimmers, where changes in the medium may also affect fuel supply, reaction rates, or local gradients. This makes it difficult to separate the influence of the polymer environment from changes in the propulsion mechanism itself.

In this chapter, I investigate electrically driven Janus particles in aqueous PEG 6000 solutions. This system offers an advantage because the propulsion is controlled externally by the applied AC electric field, while the polymer concentration can be varied independently. In this way, PEG solutions are used as viscosified polymer environments to test how increasing polymer concentration modifies the dynamics of active Janus particles. The experiments are designed around three main questions. First, how does the transition from dilute to semidilute PEG solutions influence the motion of electrically driven Janus particles? Second, do silica-gold (SiO_2 Au) and polystyrene gold Janus particles (Ps JPs) respond differently to the same polymer environment, and if so, what does this imply about particle polymer or particle substrate interactions? Third, to what extent can external electric-field control compensate for polymer-induced slowing, trapping, or deviations from active-Brownian particle like motion?

To address these questions, I compare Janus-particle trajectories at different PEG concentrations, electric-field strengths, and particle compositions. The analysis focuses on swimming velocity, trajectory shape, persistence, and deviations from simple active Brownian motion. This chapter therefore establishes how robust AC electric-field-driven Janus particles are in viscosified polymer environments and provides the basis for later experiments on transport and cargo delivery in polymer suspensions.

5.2 JPs dynamics in polymer solutions

5.2.1 **Active and passive particle's mobility**

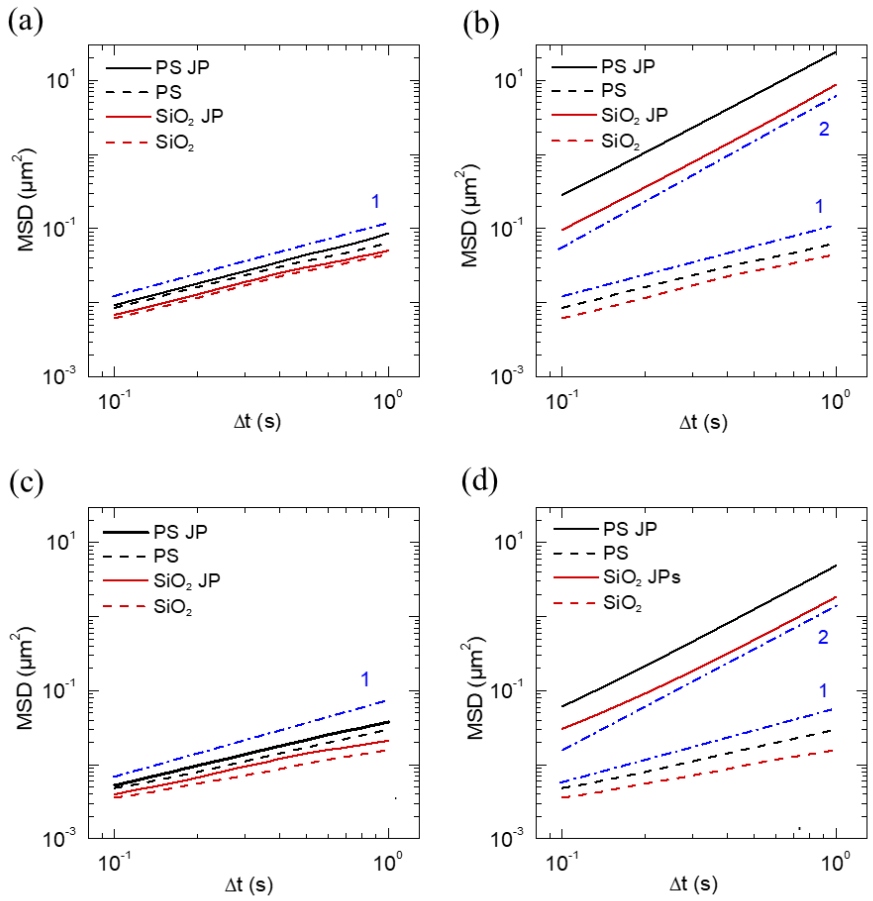

Figure 5.1, Mean squared displacement (MSD) of Au-capped silica Janus particles (SiO_2 JPs), polystyrene Janus particles (PS JPs), and their corresponding uncoated particles measured in polymer free and polymer-containing media under different electric field conditions. (a) Particle motion in polymer-free solution without electricfield both coated and uncoated particles exhibit diffusive Brownian motion with MSD slope 1. (b) Corresponding measurements with an applied electricfield 0.12 V/μm SiO_2 and PS JPs display ABP motion with slope 2, while the uncoated particles behavior remains diffusive. (c) Particle motion in PEG solution of viscosity 4mPas without an applied electricfield. The polymeric environment reduces the mobility of both coated and uncoated particles with hindered diffusion compared to the polymer free reference system. (d) Corresponding measurements with an applied electricfield 0.12 V/μm SiO_2 and PS JPs display ABP motion with slope 2, while the uncoated particles show subdiffusive behavior.

As a first step, the dynamics of polystyrene particles (Diameter: 4.37μm) and silica particles (Diameter: 5.02μm) both in coated Janus particle (JPs) and uncoated passive form are compared using mean squared displacement (MSD) analysis. As a reference, their motion is first examined in the polymer free medium without an applied electricfield. As shown in Figure

5.1(a), all four particle types exhibit diffusive Brownian motion with MSD slopes close to unity. When an electricfield of E = 0.120 $V\mu m^{-1}$ is applied, the corresponding MSDs change only for the coated particles, as shown in Figure 5.1(b). Both PS-JPs and SiO_2 -JPs exhibit active Brownian particle (ABP) type motion with MSD slopes approaching 2, whereas the uncoated silica and polystyrene particles remain diffusive with slopes close to 1. Together, this is the expected behaviour for both active and passive particles.

The particles are then dispersed in a viscosified PEG 6000 solution with a viscosity of approximately 4mPas. In the absence of electricfield, Figure 5.1 (c) shows that all four species exhibit MSD slopes below 1. This deviation from normal Brownian diffusion indicates subdiffusive, hindered motion in the polymeric medium. Compared to the polymer-free reference system, the reduced MSDs suggest increased viscous resistance and possible transient interactions within the polymeric medium. Finally, under the same conditions an electricfield of E = 0.120 $V\mu m^{-1}$ is applied, as shown in Figure 5.1(d). Both Ps and SiO_2 JPs recover directed ABP type motion with MSD slopes approaching 2, in contrast uncoated PS and Silica particles remain subdiffusive.

In addition to the above observation, it is interesting to note that the stronger hindrance observed for silica-based particles (coated as well as uncoated) in PEG solution is likely related to surface specific polymer adsorption. PEG is known to adsorb on silica through hydrogen bonding with surface silanol groups, which may locally increase viscoelastic stresses and hydrodynamic drag near the particle surface. To assess the role of surface chemistry, the SiO_2-JPs are compared with PS-JPs under identical conditions here. Although PEG can also interact with polystyrene, the absence of silanol groups is expected to weaken the polymer surface interaction. The higher mobility of PS JPs in PEG solution (see Figure 5.1(d)) suggests that the surface specific interactions contribute significantly to the different to the different propulsion dynamics of silica and PS based Janus particles.

Taken together, Figure 5.1 provides the reference behavior of passive and active particles in polymer-free and polymer-containing media. Since PEG-induced hindrance is overcome only for the driven Janus particles, the following section analyses the swimming performance of PS-JPs and SiO_2 JPs in more detail as a function of electric field strength and PEG concentration.

5.2.2 **Swimming performance of JPs in polymer media**

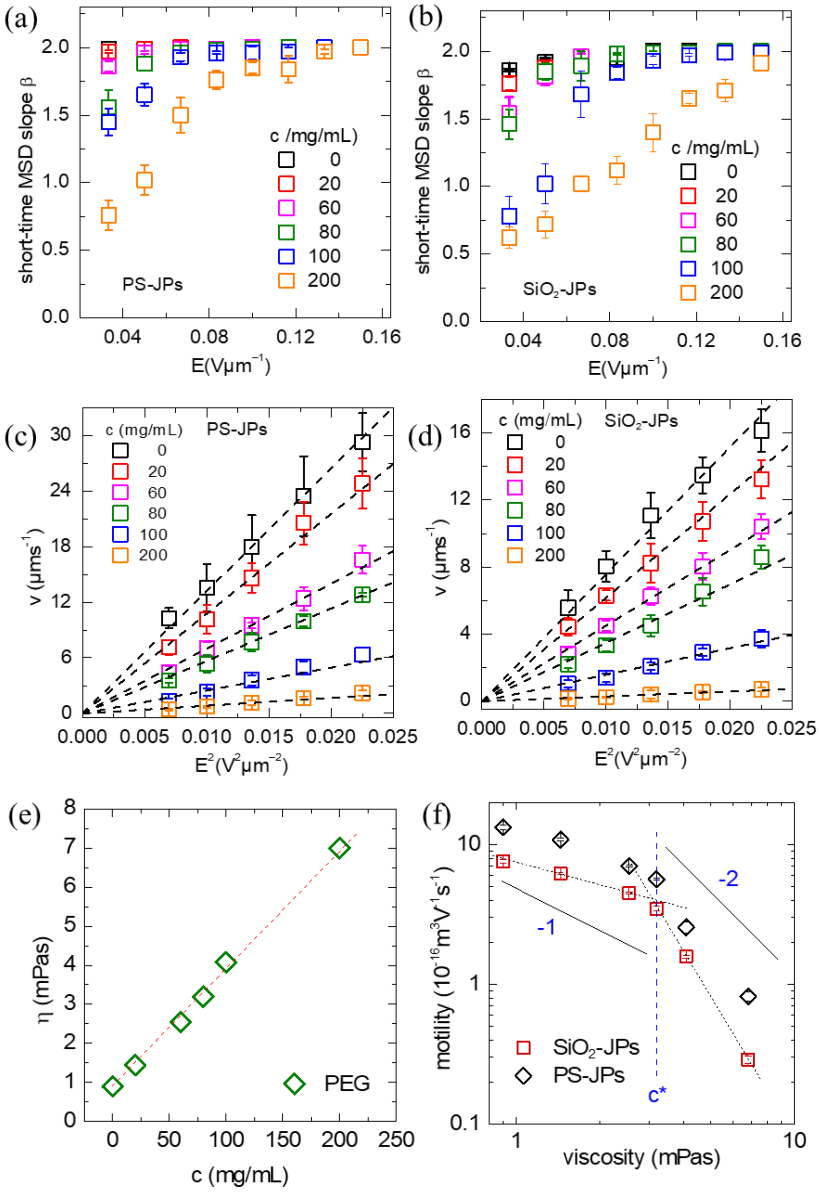

Figure 5.2, Field-strength dependence of the MSD exponent for JPs in solutions of increasing viscosity (a) Ps-JPs and (b) SiO_2 – JPs. Corresponding particle velocity v, plotted against the squared electric-field strength for (c) Ps-JPs and (d) SiO_2 – JPs. The dashed line is a least-squares linear fit to the data. (e) viscosity of polymer suspension plotted versus the concentration of PEG (f) displays a log - log plot of particle mobility of PS and SiO_2 JPs versus the viscosity of the PEG.

To explore this behaviour further, the initial MSD exponent of field driven PS JPs and SiO_2 JPs is plotted as a function of electricfield strength for different PEG concentrations, see Figure 5.2(a, b). For both particle systems, the initial MSD exponent increases with increasing field strength. At lower fields, exponents below 1 are observed, indicating subdiffusive or transiently

trapped motion. For PS-JPs, the exponent approaches the limiting value of 2 already at $E \geq 0.08V/\mu m$ for the lower PEG concentrations, corresponding to directed motion with approximately constant velocity. For a PEG concentration of 200mg/mL, a higher field strength of $E \geq 0.12V/\mu m$ is required to reach this limiting behaviour. For SiO_2 JPs, the same qualitative trend is observed, but the transition to the directed motion occurs at higher field strengths. At lower PEG concentrations, the MSD exponent approaches 2 for $E \geq 0.12V/\mu m$, whereas at concentration of 200mg/mL, this limit is reached only for $E \geq 0.16V/\mu m$. This delayed transition indicates stronger polymer induced hindrance for SiO_2 JPs compared to PS-JPs. Note, however, that for $E>0.06V/\mu m$, an MSD-slope of 2 always is reached, irrespective of the initial slope.

Under such conditions, we can determine an average JPs velocity in dependence of E^2 as shown in Figure 5.2(c, d). As expected, v increases linearly with the square of the applied electric field. Least squares fit of a linear function through the origin, we next can determine the JP mobility in dependence on PEG6000 concentration, respectively the corresponding viscosity (see Figure 5.2(e)). However, the velocity data reveal a stronger polymer induced slowing for SiO_2-JPs than for PS-JPs. In particular, SiO_2 JPs show a pronounced decrease in propulsion velocity with increasing polymer concentration, reaching a reduction of up to approximately a factor of two. Figure 5.2(f) shows that the mobility displays a significant qualitative change in its concentration dependence at a critical concentration of $c_{crit} = 80$ mg/mL, which coincides with the overlap concentration for PEG 6000.

The stronger reduction in velocity observed for SiO_2 JPs further supports the interpretation that PEG adsorption on silica contributes to the hindered propulsion. Since PEG can adsorb on silica through hydrogen bonding with surface silanol groups, silica-based JPs are expected to experience stronger polymer mediated resistance than PS-JPs. The weaker decrease in PS-JPs velocity is consistent with reduced polymer surface coupling on polystyrene, where silanol groups are absent. Thus, the velocity comparison presented in Figure 5.2 provides additional evidence that surface-specific PEG adsorption contribution.

Finally, these results show that SiO_2 JPs are more strongly affected by PEG than PS-JPs, both in the onset of directed motion and in the reduction of propulsion velocity. Therefore, the following section focuses on SiO_2 JPs and systematically examines their dynamics in PEG suspensions as a function of increasing electric field strength, with the aim of identifying the different characteristic motion modes.

5.2.3 **Characterization of the various modes of motion**

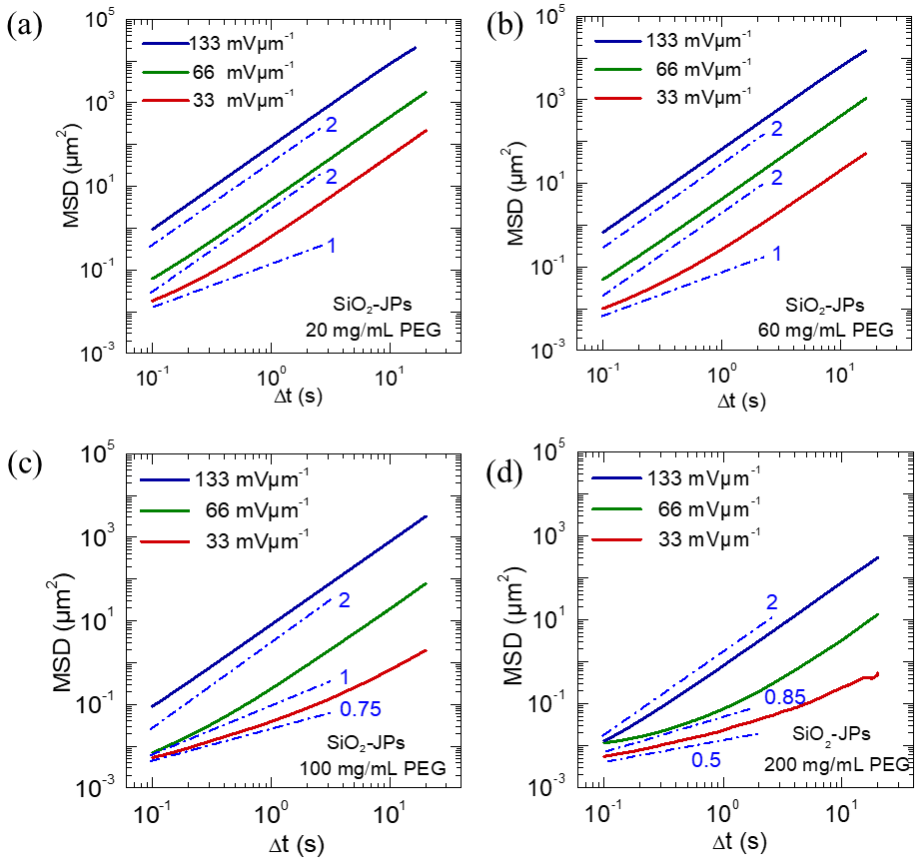

Figure 5.3, Mean squared displacement (MSD) of SiO_2 JPs measured at different electric field strengths and PEG concentrations. The dashed guide lines indicate reference power law scaling with MSD $\propto \tau^{\alpha}$, where $\alpha = 1$ corresponds to normal diffusion and $\alpha = 2$ to persistent directed motion with approximately constant velocity. (a, b) At low PEG concentration and sufficiently high electricfield strength, the MSDs approach the ABP like directed regime with $\alpha \approx 2$. (c, d) At higher PEG concentrations, this reduction of the initial MSD slope becomes more pronounced. In particular, at low electric field strengths the MSDs show subdiffusive behavior with $\alpha < 1$, indicating confined motion in the polymeric medium.

Here we first compare the MSDs of SiO_2 JPs at lower PEG concentrations and different electric field strengths. Figure 5.3(a,b) shows, at low polymer concentration, the MSDs approach a power-law scaling with $\alpha = 2$, consistent with persistent directed motion. At lower field strengths, the initial MSD slopes decrease, indicating that directed motion is not immediately established. This behavior changes more strongly at higher PEG concentrations, as shown in Figure 5.3(c, d). Here, the reduction of the initial MSD slope becomes more pronounced, particularly at weak electric fields. In these cases, slopes below unity are observed, indicating subdiffusive or transiently confined motion in the polymeric medium. Thus, the PEG solution does not only reduce the particle mobility but also modifies the time dependence of the motion.

These observations shows that the motion of JPs motion is controlled by both field strength and the polymer concentration. Based on this systematic change in the MSD behavior, the motion of SiO_2 JPs is analyzed in more detail at a fixed PEG concentration of 100 mg/mL. Three representative electric field strengths are selected E = 33 mV/µm, 66 mV/µm and 133 mV/µm. These conditions correspond to three characteristic motion types observed experimentally, I.e., Confined at low field strength, intermittent jittery motion at intermediate field strength, and persistent motion at high field strength. The corresponding trajectories and angular distribution are then used in the following section to characterize these regimes more quantitatively.

Based on the MSD analysis, the motion of SiO_2 JPs is further examined at a fixed PEG concentration by analysing representative trajectories and angular distributions. For this purpose, the displacement angle Θ and the particle orientation angle φ was defined with respect to x-axis, as shown schematically in Figure 5.4 (a). This allows the directional persistence of the particle motion to be compared for different electricfield strengths. At the lowest field (E=33 mV/µm) strength, the particle motion remains to a small spatial region during the observation time, see Figure 5.4(b). The corresponding angular distributions in Figure 5.4(e) are broad and show no pronounced preferred displacement direction. This indicates that the propulsion is too weak to generate persistent direction motion against the local resistance of the PEG medium. The particle orientation also fluctuates strongly, consistent with weak activity and local confinement (**see supplementary video 4**).

At intermediate field strength (E=, 66 mV/µm), Figure 5.4(c) shows that the particle is no longer confined, but its trajectory remains irregular. The motion contains short directed segments interrupted by lateral deviations and changes in orientation. This behaviour is also reflected in the angular distribution as show in Figure 5.4(f), where partial directionality is visible, but both displacement and orientation angles remain broadly distributed. This motion type therefore represents an intermediate state in which the field induced propulsion partly overcome the polymer induced hindrance, but not yet in a stable and persistent manner (**see supplementary video 5**).

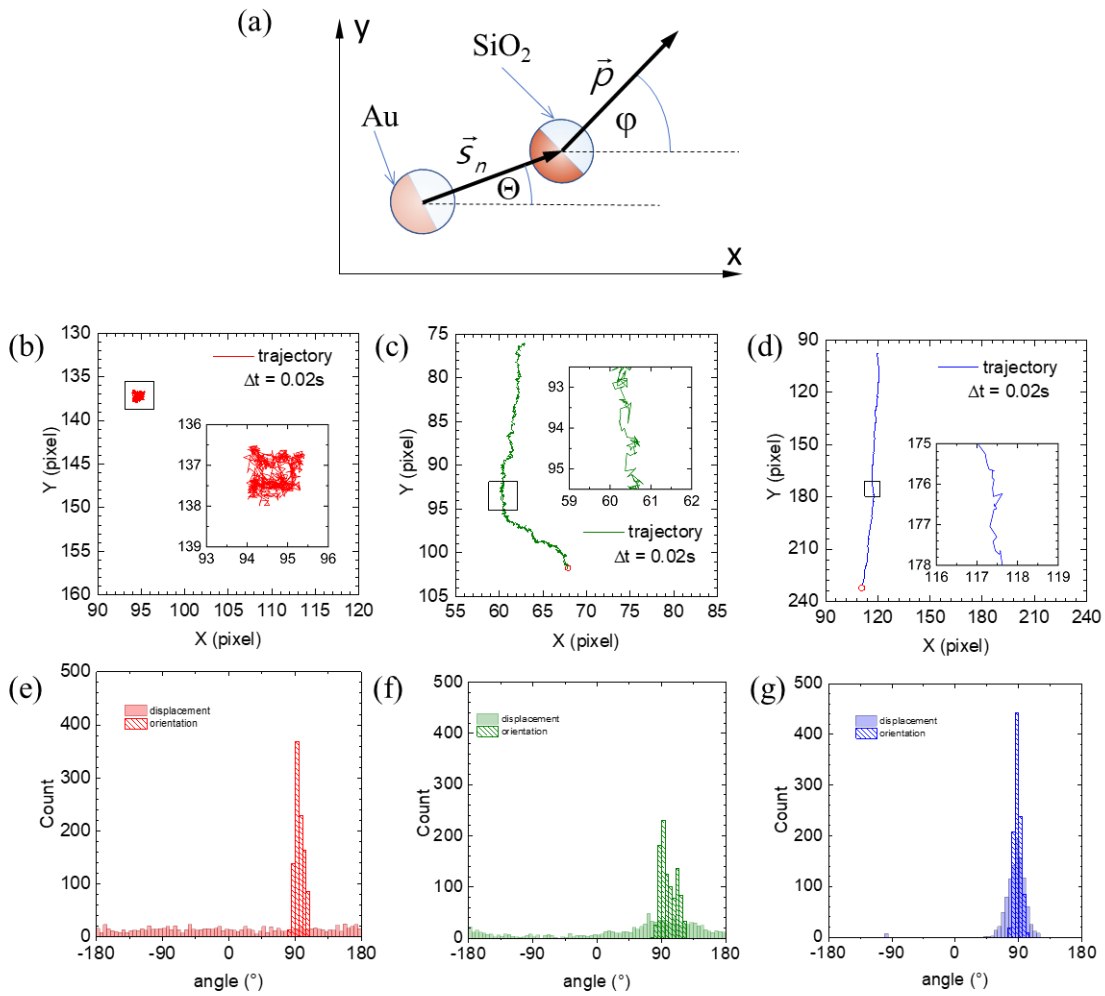

Figure 5.4, Characterization of SiO_2-JP motion modes in PEG solution. (a) Schematic definition of the JP displacement angle (Θ) and orientation angle (φ) with respect to the x-axis. (b–d) Representative trajectories recorded over 20s at increasing electric field strengths, showing three characteristic motion types: (b) confined motion, (c) jittery motion, and (d) straight-line motion. (e–g) Corresponding histograms of particle orientation and displacement angles. (e) In the confined regime, displacement angles exhibit a broad distribution with no preferred direction, while the particle orientation fluctuates due to weak activity and local confinement. (f) In the jittery regime, partial directionality is observed, accompanied by noticeable deviations in both displacement and orientation angles. (g) In the straight-line regime, both angular distributions become narrow, indicating persistent propulsion with only small deviations from the mean direction of motion.

Finally at highest field strength, the trajectory becomes nearly straight over the analysed time interval, see Figure 5.4(d). The corresponding histogram in Figure 5.4(g) show narrow distributions of both displacement and orientation angles, indicating persistent propulsion with only small deviations from the mean direction of motion (**see supplementary video 6**). Under

these conditions, the electric driving is sufficiently strong to overcome the local hindrance of the PEG solution, and the particle motion approaches the ABP like directed behaviour observed in the MSD analysis.

Thus, Figure 5.4 illustrates three representative situations observed at different electric field strengths at selected field strengths. Together with the systematic MSD analysis in Figure 5.3, these distributions of angles support the interpretation that the SiO_2 JP motion changes continuously from confined to persistent directed motion as the electricfield strength is increased.

5.2.4 **Autocorrelation of displacement (Θ) and orientational (*φ*) angles**

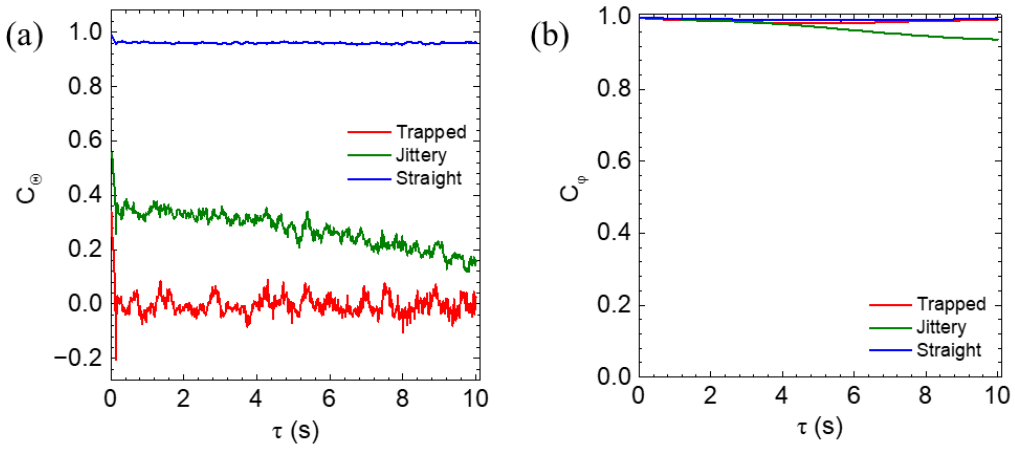

Figure 5.5, Autocorrelation analysis of the displacement and orientation angles of SiO_2 JPs in PEG solution for three representative field strengths corresponding to confined, jittery and straight-line motion. (a) Displacement angle (Θ) autocorrelation function. At low electricfield strength, the autocorrelation decays strongly and fluctuates around low values, indicating weak directional persistence. At intermediate field strength, the autocorrelation remains higher but shows pronounced fluctuations, consistent with jittery motion. At high electricfield strength, the autocorrelation remains close to unity, indicating persistent displacement along a stable direction. (b) Orientation angle (φ) autocorrelation function for the same trajectories. Compared to the displacement angle, the orientation autocorrelation remains more stable, especially at high field strength, showing that straight line motion is accompanied by persistent particle orientation.

Following the trajectory and angular distribution analysis in Figure 5.4, the temporal stability of the displacement and orientation angles is quantified using autocorrelation functions. This analysis allows the directional persistence of the three representative motion types to be compared more directly. The displacement angles (Θ) characterized the direction of

displacement, whereas the orientation angle (φ) describes the particle body orientation with respect to the x axis.

As shown in Figure 5.5(a), the displacement angle autocorrelation (C_Θ) strongly depends on the applied electricfield strength. At the lowest field strength, corresponding to confined motion in Figure 5.4(b), the autocorrelation rapidly decreases and fluctuates around low values (red line). This indicates that the displacement direction is not maintained over time, consistent with the broad angular distribution observed in Figure 5.4(e). At intermediate field strength, corresponding to jittery motion in Figure 5.4(c), the autocorrelation remains higher but exhibits pronounced fluctuations (see green line in Figure 5.5(b)). This reflects intermittent directional persistence interrupted by sudden changes in displacement direction, in agreement with the broader but partially directional histogram in Figure 5.4(f). At the highest field strength, corresponding to straight line motion in Figure 5.4(d), the autocorrelation remains close to unity, showing that the particle displacement direction is more stable over the analysed time interval.

The Orientation angle autocorrelation (C_φ) in Figure 5.5(b) remains close to unity for all three electric field strengths. This shows that the particle orientation is largely stable over the analysed time interval, independent of whether the trajectory appears confined, jittery or straight. Therefore, the differences between the three motion types cannot be attributed primarily to a loss of particle orientation. Instead, they arise mainly from changes in the displacement direction, as reflected by the much stronger variation of the displacement-angle autocorrelation in Figure 5.5(a). This suggests that the polymeric environment perturbs the translational motion of the particle more strongly than its orientational stability.

5.2.5 **Cross correlation of displacement (Θ) and orientational angles (*φ*)**

Following the trajectory analysis in Figure 5.4 and the angular autocorrelation analysis in Figure 5.5, now the relation between the particle orientation and displacement direction is quantified using the cross correlation $C_{\Theta,\varphi}$, see Figure 5.6. This analysis is important because Figure 5.5 shows that the particle orientation remains relatively stable in all three cases, whereas the displacement direction changes strongly depending on the electricfield strength. Therefore, the decisive difference between the motion types is not only whether the JP orientation is stable, but whether this orientation correlated with the actual direction of displacement**.**

At the lowest field strength, corresponding to confined motion in Figure 5.4(b), $C_{\Theta,\varphi}$ remains low (see red line in Figure 5.6). This indicates that the particle orientation and the displacement direction are only weakly coupled. Although the particle maintains an orientation, the surrounding PEG medium prevents this orientation from producing persistent displacement. This is consistent with the broad displacement angle distribution in Figure 5.4(e) and the weak displacement angle autocorrelation in Figure 5.5(a).

At intermediate field strength, corresponding to the jittery motion in Figure 5.4(c), the cross correlation increases but remains clearly below unity (see green line in Figure 5.6). This indicates partial coupling between orientation and displacement direction. The particle can move intermittently along its orientation, but this motion is repeatedly disturbed by the polymeric environment, leading to the irregular trajectory and broader angular distributions observed in Figure 5.4(f).

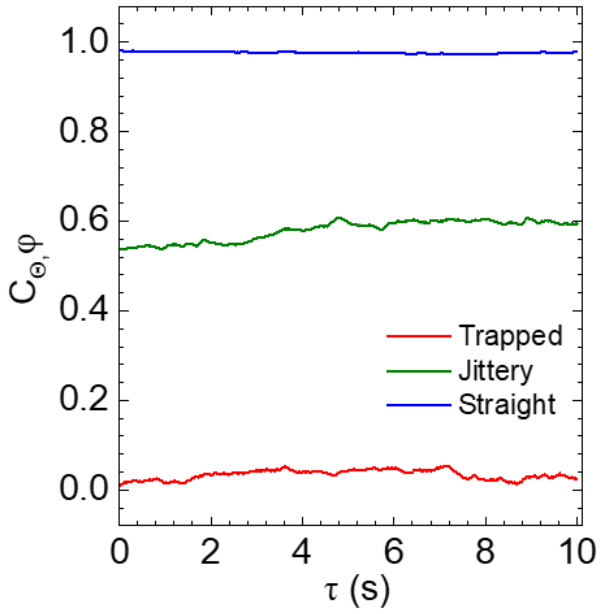

Figure 5.6, Cross correlation $C_{\Theta,\varphi}$ between the displacement angle (Θ) and orientation angle (φ) of SiO2 JPs in PEG solution for three representative electric field strengths corresponding to confined, jittery and straight-line motion. At low electric field strength, the cross correlation remains low, indicating weak coupling between particle orientation and displacement direction. At intermediate field strength, the cross correlation increases but remains below unity, consistent with partially directed motion. At High field strength, the cross correlation remains close to unity, showing that the displacement direction is strongly aligned with the particle orientation. This strong alignment demonstrates that ABP type motion is recovered at sufficiently high field strengths.

Finally at the highest filed strength, corresponding to the straight-line motion in Figure 5.4(d), $C_{\Theta,\varphi}$ remains close to unity (see blue line in Figure 5.6). Here, the displacement direction is

strongly aligned with the particle orientation, showing that the propulsion is no longer significantly disrupted by local polymer induced hindrance. Together with the narrow angular distributions in Figure 5.4(g) and the stable autocorrelations in Figure 5.5, this demonstrates ABP-like directed motion is recovered within the experimental observation window **at** sufficiently high electricfield strengths.

Taken together, Figures 5.4 to 5.6 show that the different motion types arise from the changing coupling between particle orientation and actual displacement. In PEG solution, SiO_2 JPs may remain orientationally stable even when their translational motion is hindered. Only at sufficiently high field strength does the particle orientation reliably translate into persistent displacement, marking the recovery of ABP-like propulsion**.**

5.3 Conclusion

This chapter examined how aqueous PEG solutions influence the motion of electrically driven Janus particles. The experiments show that polymer solutions affect both passive diffusion and active propulsion. For uncoated passive particles, PEG leads to hindered and subdiffusive motion. For Janus particles, however, the applied AC electric field provides an additional control parameter: by increasing the field strength, directed active motion can be recovered even in polymer-containing media. Thus, the observed slowing cannot be explained by bulk viscosity alone, but results from the competition between polymer-induced resistance and externally controlled propulsion.

A central observation is the different response of silica gold and polystyrene gold Janus particles. Silica based Janus particles require higher electric-field strengths to regain directed motion and show a stronger decrease in propulsion velocity with increasing PEG concentration. This suggests that the particle surface plays an important role. In particular, PEG can interact with silica through hydrogen bonding with surface silanol groups, which may increase local polymer mediated drag near silica surfaces. Polystyrene based Janus particles are therefore less strongly affected under otherwise similar conditions.

The advantage of the AC electric field driven system is that the propulsion strength can be tuned without changing the chemical composition of the medium [182, 184, 186,]. This is different from many chemically driven swimmers, where activity is coupled to fuel concentration, reaction kinetics and chemical gradients. In such systems, polymer solutions can modify not only the viscosity but also the fuel supply and local reaction environment. Here, the external

electric field provides a cleaner control parameter, allowing the activity to be adjusted reversibly while the PEG concentration remains fixed.

The detailed analysis of silica gold Janus-particle motion shows that PEG does more than reduce the swimming speed. It also modifies the character of the trajectories. MSD analysis, trajectory shapes, angular distributions, autocorrelations and cross-correlations show that the coupling between particle orientation and displacement direction depends on field strength. At low fields, particles can remain orientationally stable but do not translate persistently. At intermediate fields, partial coupling produces irregular, jittery motion. At high fields, the displacement direction becomes strongly aligned with the particle orientation, corresponding to recovered active-Brownian particle like motion.

Overall, this chapter demonstrates that electrically driven Janus particles can remain functional in polymeric environments when the applied electric field is chosen appropriately. Compared with chemically and light driven active colloids [191,192], this approach provides a fuel-free and externally tunable platform for studying microswimmers in viscosified media. These findings provide the basis for the next step of the thesis: using field-controlled Janus particles for transport and cargo manipulation in polymer-rich environments.

Chapter 6 - **Ac Field driven active colloids cargo delivery in polymer solutions**

6.1 Introduction

Chapter 5 showed that AC electric-field-driven Janus particles can remain mobile in PEG solutions when the applied field strength is sufficiently large. This establishes the basic requirement for using these particles not only as swimmers, but also as functional transport units in polymeric environments. The next question is whether this field-controlled motion can be combined with particle cargo interactions to achieve controlled pickup, transport and release in a viscosified medium.

Cargo delivery at the microscale requires more than persistent propulsion. A useful carrier must be able to bind a passive object, move with it through the surrounding medium, release it at a chosen stage, and ideally return without the load. In polymer solutions, this task becomes more challenging because the increased viscosity and possible polymer-mediated interactions can hinder both swimmer motion and cargo manipulation. At the same time, AC electric fields offer a direct control route because the propulsion direction and dielectrophoretic interactions [199, 213, 214,] between Janus particles and passive cargo can be tuned by the applied frequency.

In this chapter, I investigate cargo delivery using AC electricfield driven Janus particles in PEG polymer solutions. The experiments focus on how field frequency and field strength control the different steps of the transport cycle: cargo pickup, cargo-loaded motion, cargo release and load-free return. The aim is to demonstrate whether the same electrically driven platform that restores active motion in polymer solutions can also be used to perform controlled microscale transport in a viscosified environment.

6.2 Field Controlled Cargo Pickup, transport and delivery in polymer solutions

6.2.1 **Cargo Pickup by Self-Dielectrophoretic Janus Particles in PEG Solutions**

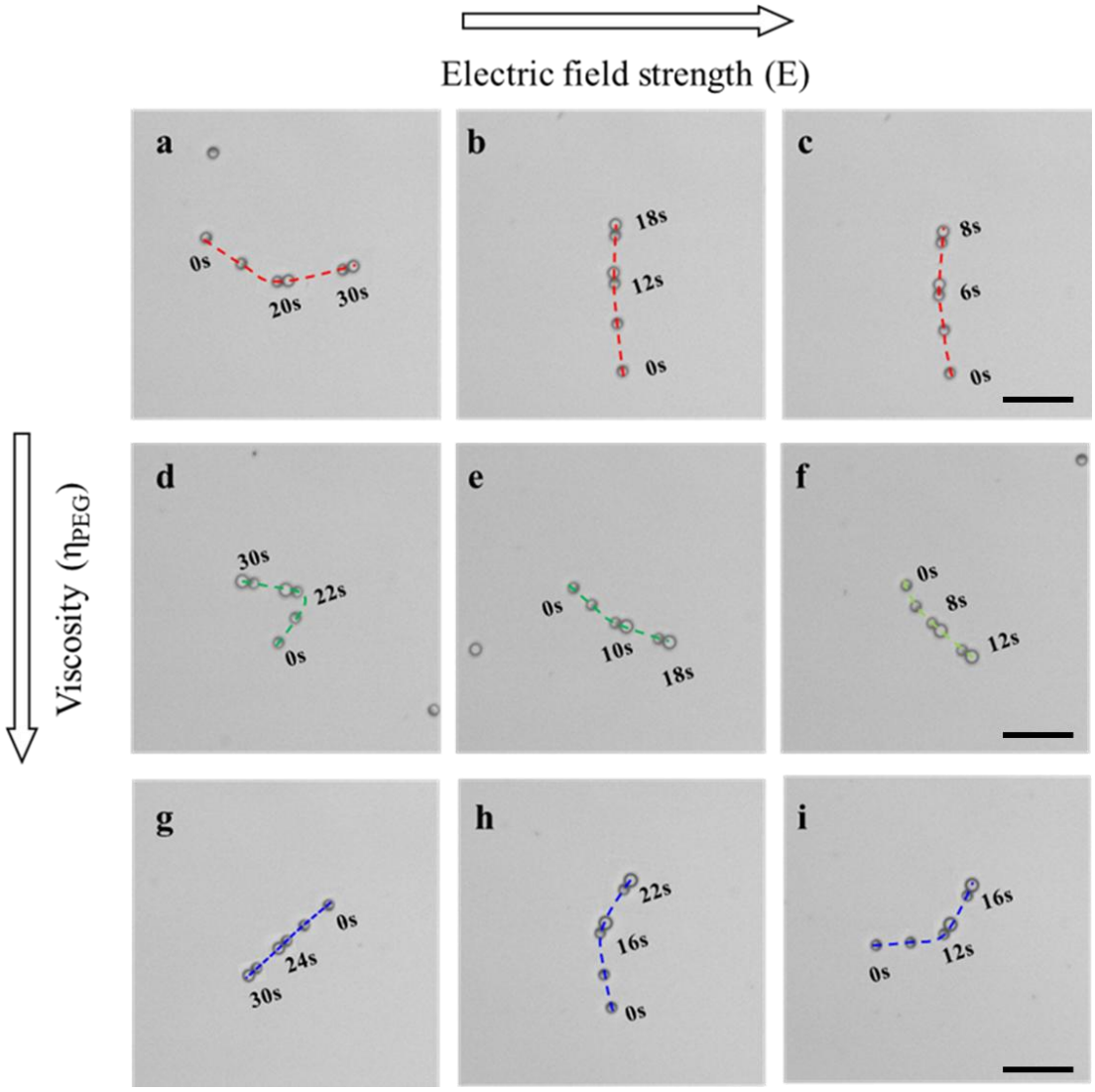

Figure 6.1, Cargo pickup by SiO_2 JPs in PEG solutions of different viscosities. Microscopy images show cargo approach and pickup at fixed frequency f = 250 kHz. The electricfield strength increase from left to right: E =0.066,0.100, and 0.133 V/μm, while the PEG viscosity increases from top to bottom: η_{PEG} = 1.44,2.54, and 4.00 mPa s. The dashed trajectories indicate the motion of the JPs before and during the cargo pickup. Cargo attachment is observed for all viscosities when sufficiently large electric fields are applied. In several cases, such as panels (d), (h), and (i), pickup occurs even when the initial trajectory is not directly aligned with the cargo, indicating that short range dielectrophoretic attraction redirects the JP towards the cargo. The scale bar corresponds to 30μm.

Here, the Janus particles (JPs) of size 5.00 μm were suspended in different concentrations of polymer suspensions along with silica cargo particles of size 5.23 μm. The suspension was subjected to an alternating electric field with constant frequency 250 KHz using transparent

electrodes. The term “self-dielectrophoresis” describes this phenomenon, as the Janus particles move dielectrophoretically in response to the local electric field gradient that they themselves create near the electrodes. Owing to the different polarizabilities of the metallic and dielectric hemispheres, the JPs creates an asymmetric local electric-field distribution. The applied electrified also induces attractive dipolar interactions in addition to the self-propelling nature of the Janus particles that enable the silica cargo particles to assemble to the Janus particles [199].

This field asymmetry is responsible for self-propulsion and, at the same time, induces attractive dipolar interactions between the metallic hemisphere and nearby passive cargo particles. Similar AC-field-driven Janus shuttle systems have been shown to trap and transport cargo through field-induced dipolar interactions, where cargo remains attached as long as the field is applied. In the present system, this mechanism is used to test whether cargo pickup remains possible in PEG solutions, where polymer-induced resistance can hinder JP motion.

Figure 6.1 shows representative cargo-pickup events for SiO_2 JPs at fixed frequency. The electric field strength is increased from left to right (E = 0.066, 0.100, and 0.133 V/µm), while the PEG viscosity increases from top to bottom (η_{PEG} = 1.44, 2.54, and 4.00mPas). The red, green and blue dashed lines mark the JP trajectories at low, intermediate and high viscosity, respectively. In all three viscosity regimes, cargo pickup occurs once the active particle approaches the passive cargo sufficiently closely. This shows that the short-range dielectrophoretic attraction remains effective even in polymer-containing media.

The role of the electric field becomes particularly clear at higher viscosities. At low viscosity, Figure 6.1(a-c), the JP remains highly mobile and cargo pickup occurs readily over the investigated field range. At intermediate and high viscosities, Figure 6.1(d-i), the particle motion is more strongly affected by the polymeric environment. Nevertheless, cargo capture is still observed when the applied field is sufficiently large. In several cases, especially Figure 6.1(d, h, i), the initial JP trajectory is not directly aimed at the cargo. The subsequent redirection of the JP at short separation distances indicates that local dielectrophoretic attraction assists the final pickup step.

Thus, Figure 6.1 demonstrates that PEG-induced viscosity does not suppress the cargo-capture mechanism itself. Instead, the main requirement is that the electric field must be strong enough to bring the active particle into the capture range. This establishes the first condition for cargo

transport in polymeric media: the JP must remain sufficiently mobile to approach the cargo, while the sDEP interaction provides the short-range attraction required for attachment.

6.2.2 **Cargo transport of passive colloids after Self-Dielectrophoretic pickup**

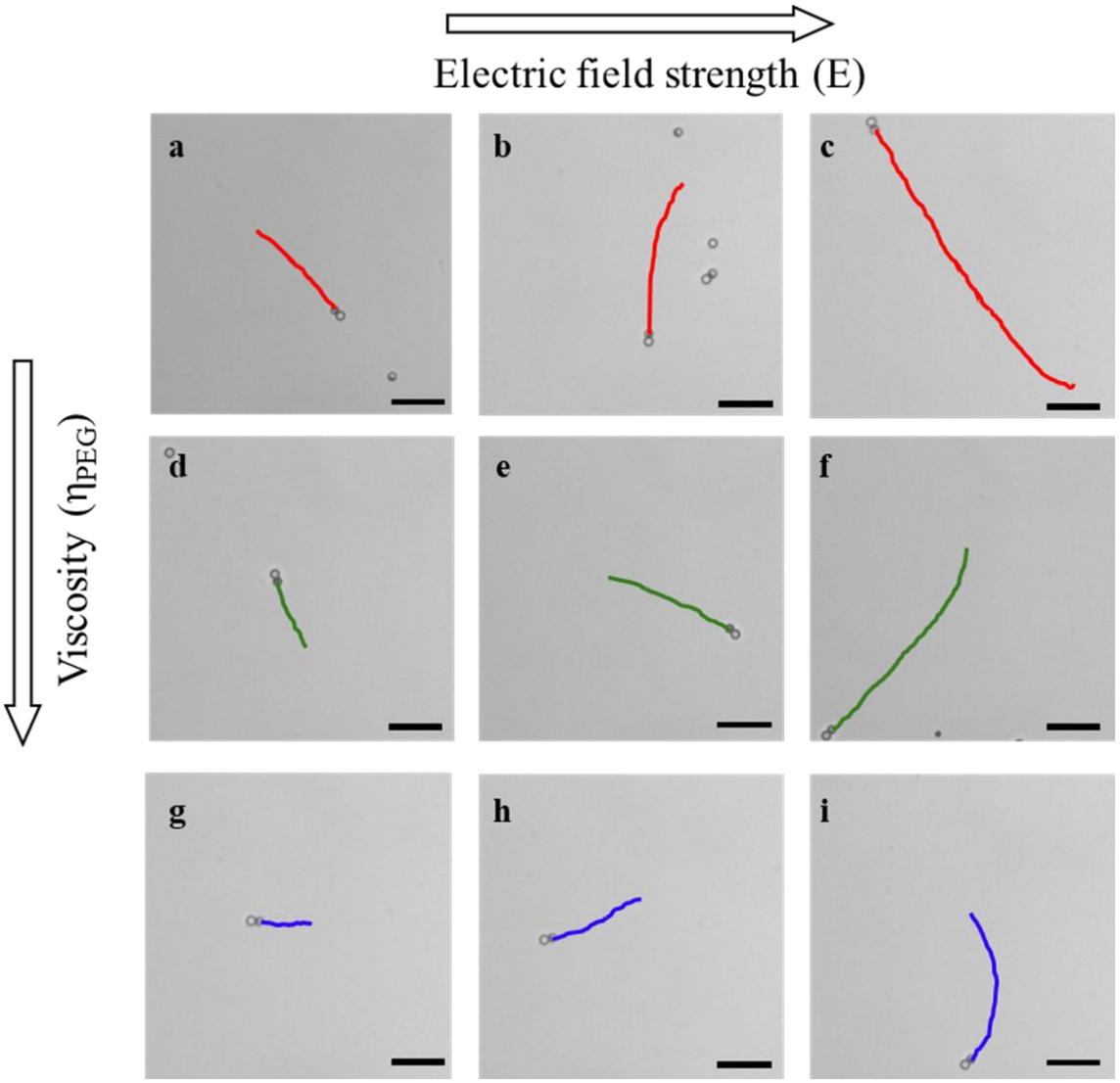

Figure 6.2, Trajectories of SiO_2 JPs cargo assemblies in PEG solutions after pickup of a single passive cargo particles. The trajectories are recorded at fixed frequency f = 250 kHz. The electricfield strength increase from left to right: E =0.066,0.100, and 0.133 V/µm, while the PEG viscosity increases from top to bottom: η_{PEG} = 1.44,2.54, and 4.00 mPa s. (a-c) η_{PEG} = 1.44mPas, (d-f) η_{PEG} = 2.54mPas, and (g-i) η_{PEG} = 4.00 mPas. The coloured lines indicate the trajectories of the JP-Cargo assembly during transport. Cargo-loaded JPs remain mobile in all investigated PEG solutions, with longer and more persistent trajectories observed at higher electric field strengths. The scale bar corresponds to 30µm.

After cargo pickup, the motion of the JP cargo assembly is demonstrated over an observation time 20s. Figure 6.2 shows representative trajectories for three electric field strengths, E=0.066,

0.100, and 0.133 V/μm, and three PEG viscosities, η_{PEG} = 1.44,2.54, and 4.00 mPa s. This allows the influence of both driving strength and medium viscosity on cargo transport to be compared directly.

At the lowest viscosity, η_{PEG} = 1.44mPas, the JP-cargo assemblies remain mobile for all applied field strengths, see Figure 6.2(a-c). At the lowest field, transport distance is limited, while increasing the field strength leads to longer and more persistent trajectories. This indicates that the increased electric driving enhances the propulsion of the loaded JP-cargo assembly.

At the intermediate viscosity, $\eta_{PEG} = 2.54$mPas, the trajectories become shorter and less extended, particularly at low and intermediate fields, see Figure 6.2(d-f). This shows that the increased viscosity reduces the mobility of the loaded assembly. Nevertheless, at the highest field strength, the JP cargo assembly still undergoes directed transport over applicable distances. At the high viscosity, η_{PEG} = 4.00mPas, transport is most strongly hindered, see Figure 6.2(g-i). At low field strengths, only limited displacement is observed. With increasing field strength, the transport distance increases, and directed motion is recovered at the highest field.

Overall, Figure 6.2 demonstrates that cargo loaded SiO_2 JP can transport passive cargo in PEG solutions at all the chosen electricfield strengths. The transport performance is controlled by the competition between electricfield driven propulsion and the polymer induced drag. Since cargo pickup and directed transport remain possible even at the highest investigated viscosity (η_{PEG} = 4.00mPas) when sufficiently strong electric fields (E=0.133 V/μm) are applied, these conditions are selected to demonstrate cargo delivery.

6.2.3 **Controlled Cargo Delivery and Load-Free Return**

For the cargo delivery experiment, the JP-Cargo assembly is first driven at high frequency (f=250kHz) and high field strength (E=0.133 V/μm). Under these conditions, self-dielectrophoretic propulsion is accompanied by attractive dipolar interactions between Janus particles and passive cargo. These interactions keep the cargo attached to the metallic hemisphere during the transport, corresponding to the pickup and transport steps shown in Figure 6.3 (a, steps 1 and 2).

Cargo release is achieved by switching the frequency to (f=4kHz). At this lower frequency, the propulsion mechanism changes from the high frequency sDEP regime to the low frequency induced charge electrophoresis. As a result, the direction of JP motion reverses, while the attractive dipolar coupling to the cargo is terminated due to frequency switching. The JP therefore moves away from the

cargo, producing controlled release followed by load free return motion, as illustrated in Figure 6.3(a, steps 3 and 4).

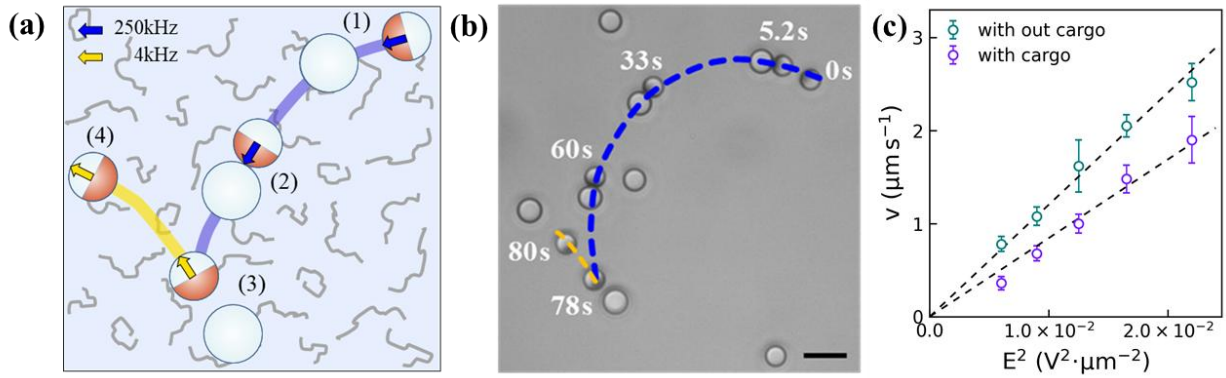

Figure 6.3, Cargo delivery cycle of SiO_2 JPs in PEG solutions. (a) Schematic representation of the delivery protocol: (1) cargo pickup, (2) forward transport of the JP–cargo assembly, (3) cargo release followed by reverse motion of the unloaded JP, and (4) subsequent load-free motion. Blue arrows indicate forward motion at high frequency (f = 250 kHz), while yellow arrows indicate reverse motion at low frequency (f =4 kHz). (b) Experimental image sequence showing the corresponding cargo delivery process in PEG solution of viscosity η_{PEG} = 4.00mPas and electricfield strength (E=0.133 V/μm). The blue dashed line marks forward cargo transport, and the yellow dashed line marks the reversed trajectory after cargo release. The time stamps indicate the particle position during the delivery cycle. The scale bar corresponds to 15μm. (c) Mean velocity of SiO_2 JPs plotted as a function of the squared electric field strength, E^2, in PEG solution with and without attached cargo. In both cases, the velocity increases approximately linearly with E^2, confirming the field-driven nature of the propulsion. The JP–cargo assembly moves more slowly than the unloaded JP because the attached cargo increases the hydrodynamic drag and resistance in the polymer solution. The dashed lines are linear fits to the data.

The corresponding experimental realization is shown in Figure 6.3(b) for PEG solution of viscosity η_{PEG} = 4.00mPas. The JP first transports the cargo along the forward trajectory at 250kHz (blue trajectory in Figure 6.3(b)). After switching to 4kHz, the cargo remains at the delivery position, whereas the JP reverses direction (yellow trajectory in Figure 6.3(b)) and moves away without load. This demonstrates that cargo pickup, transport, delivery and load-free return can be controlled by changing only the frequency of the applied AC field **(see supplementary video7)**.

Although the frequency-switching mechanism is general and should also operate in simple aqueous media [199], the present experiments are deliberately performed in PEG solutions. This choice demonstrates that the complete delivery cycle remains functional even in a polymeric medium, where passive diffusion is slowed and particle motion is hindered. The field-dependent velocities with and without cargo are compared in Figure 6.3(c). In both cases,

the velocity increases approximately linearly with E^2, confirming that the motion remains governed by the electric-field-driven propulsion mechanism. However, the JP–cargo assembly moves more slowly than the unloaded JP at the same field strength. This reduction is expected because the attached cargo increases the effective hydrodynamic drag and the resistance experienced by the swimmer in the PEG solution. The comparison therefore shows that cargo loading reduces the absolute speed, but does not suppress field-controlled propulsion.

Finally, Figure 6.3 demonstrates a complete and reversible cargo-shuttling cycle in a polymeric medium. In contrast to release strategies based on simply switching off the field, the present protocol uses frequency switching to actively separate the JP from the cargo while preserving controlled particle motion. This shows that AC-driven JPs can combine propulsion, cargo retention, release and load-free return within a single externally tunable mechanism.

6.3 Conclusion

This chapter demonstrated cargo delivery using AC electric-field-driven Janus particles in PEG polymer solutions. The main advantage of this strategy is that propulsion, cargo pickup, transport, release and load-free return are all controlled by the applied AC electric field. Thus, cargo handling is not treated as a separate process from swimmer propulsion, but as part of the same field-controlled mechanism.

In many microscales cargo-transport approaches, release is achieved by switching off the external field after transport. The cargo then separates passively, mainly by diffusion. While this can be sufficient in simple liquids, it becomes less reliable in polymer solutions, where diffusion is slowed and particle motion is strongly hindered. In the present system, cargo release is instead controlled actively by changing the field frequency. At high frequency, the Janus particle operates in the self-dielectrophoretic regime, where the electric field drives propulsion and supports cargo attachment through attractive dipolar interactions. When the frequency is lowered, the propulsion direction changes and the Janus particle moves away from the cargo, enabling controlled release followed by load-free return.

This provides a unified mechanism for cargo shuttling in viscosified polymer environments. The field amplitude controls the strength of propulsion and allows the Janus particle–cargo assembly to overcome polymer-induced resistance. The field frequency controls the propulsion mode and the cargo interaction. Together, these two control parameters make it possible to regulate both cargo retention and cargo release under the same experimental conditions.

The novelty of this experiment is therefore not only the transport of cargo in a polymer solution, but the realization of a complete electrically controlled delivery cycle: pickup, loaded transport, release and load-free return. The demonstration at the highest investigated viscosity shows that the system remains functional even when passive diffusion and low-activity motion are strongly hindered. These results establish AC-driven Janus particles as a promising model system for controlled microscale transport in polymeric media, where fuel-free operation, tunable activity and on demand release are required.

Chapter 7 - **Island Hopping of active colloids**

7.1 Introduction

In the previous chapters, I studied Janus-particle motion in polymer solutions and showed how AC electric fields can maintain propulsion and enable cargo transport in viscosified media. In this chapter, I move from homogeneous polymer solutions to spatially heterogeneous colloidal landscapes, where passive particles form obstacles that directly influence active trajectories.

A central question is how an active colloid moves when the distance between obstacles is shorter than its free persistence length. In a simple fluid, an active Brownian particle loses directional memory gradually through rotational diffusion. In a structured environment, however, collisions with obstacles can cause abrupt reorientation events, producing motion that resembles run-and-tumble dynamics, although the underlying mechanism is purely colloidal.

Here, I investigate AC electric-field-driven Janus particles moving through passive silica islands. The applied field both propels the Janus particles and induces electrohydrodynamic attraction between passive silica spheres, which assemble into island-like clusters. These islands act as localized obstacles in a quasi-two dimensional environment.

The aim of this chapter is to determine how such passive island structures modify active motion. In particular, I examine whether collisions with islands only slow the particles down or whether they create a distinct hopping-like dynamics with backscattering at the island boundaries. This provides a controlled example of how a field-assembled passive environment can transform the trajectory statistics of an electrically driven microswimmer.

This chapter is part of the published article: Venkata Manikantha Sai Ganesh, T., Vogel, P., Palberg, T., and Buttinoni, I., **2023**. Island hopping of active colloids. Soft Matter, 19(29), pp.5452-5458.

7.1 Island-Hopping of active colloids in the self-assembled passive crowd.

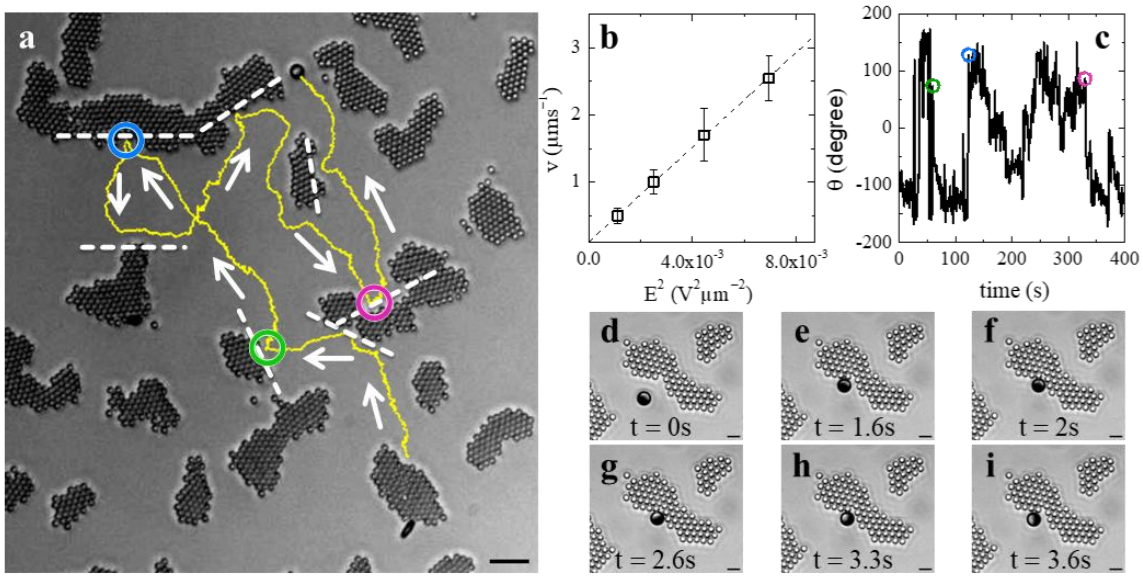

Figure 7.1, Active JP undergoing island-hopping in an environment of 'passive' colloidal islands. (a) Trajectory of an active JP (electric field, E = 0.066 V/μm) in the presence of passive silica spheres forming clusters (islands). The arrows and dashed lines indicate the swimming direction and the location as well as the orientation of "scattering planes". The scale bar is 20 μm. (b) Mean swimming velocity, v, in the islands environment plotted against the squared electric field strength. Each data point is an average of over 10 – 15 individual particles based on the short-time MSD analysis. The error bars denote the corresponding standard deviation. The dashed line is a least-squares linear fit to the data with a slope of approximately 3.5×10^{-2} $V^{-2}\mu m^{3} s^{-1}$. (c) Time evolution of the angle θ corresponding to the yellow trajectory in (a). The coloured circles mark the same scattering events as in (a). (d–i) Sequence of snapshots showing the interaction of an active JP particle with an island of passive silica spheres; the microswimmers approaches and comes in contact with a cluster, rotates counter clockwise and swims away. The scale bar is 5 μm.

The formation and structural properties of the passive silica islands were introduced in Chapter 4, where it was shown that uncoated silica particles can reversibly assemble into dense, locally ordered clusters under a vertical AC electric field. These field induced islands arise from electrohydrodynamic attractions between the passive particles and provide a tunable obstacle landscape for active colloids. In this chapter, the same island-forming conditions are used to investigate how electrically driven Janus particles move through and interact with this structured passive environment.

Briefly, uncoated silica particles with diameter $2.31\mu m$ are used as passive obstacles for $5.02\ \mu m$ silica gold Janus particles. When an AC electric field is applied, the passive particles assemble into close-packed islands [200,201,202,], while the Janus particles remain motile and undergo ICEP-driven propulsion [184]. This creates an active–passive system in which the moving JP repeatedly encounters field-assembled passive clusters.

Figure 7.1(a) shows the trajectory of an active JP when it cruises through islands of silica colloids (Figure 7.1) and an AC electric field E = 0.066 V/μm is applied in z. The linear increase of the mean swimming velocity (v, Figure 7.1(b)) with E^2 is preserved, but $v \sim 0.5v_o$, indicating that, on average, the complex environment reduces the motility of the active colloids. By calculating the instantaneous velocity as a function of time for the trajectory shown in Figure 7.1(a), we observe no significant change when they approach and leave the islands. Nonetheless, the key difference with free active Brownian motion lies in the fact that, here, the direction of the velocity is randomized not only by rotational diffusion but also by microswimmers-island 'collisions. In particular, since τ_R is much larger than the typical time required for the microswimmers to travel between islands (given by d_c/v) for all values of v used in our experiments, the contribution of rotational diffusion is negligible. Hence, the 2D trajectory of the active Brownian particle is characterized by the combination of straight paths and abrupt reorientations, and qualitatively resembles the run-and-tumble motion of bacteria such as E. coli, except for the fact that the reorientations here are systematic and due to 'backscattering'. In Figure 7.1(c), we plot the angle θ of the instantaneous velocities of the trajectory in Figure 7.1(a). 'Runs' can be identified by the regions where θ is roughly constant. Conversely, 'turnings' give rise to abrupt jumps lasting only few seconds (see coloured circles). In several instances the changes of local angle are also greater than 90°. These observations strongly point towards the presence of torques that, upon collision, quickly turn the velocity vector. A close look at the JP-island interaction (Figure 7.1(d-i)) reveals in fact that, when a JP collides against one of the clusters, the orientation is swiftly reversed via in-plane rotation so that it leaves as if it were 'backscattered' by the island. Overall, the behaviour of the JP in the complex environment made of passive islands can be clearly distinguished from the motion of ABP. The active colloid always swims in the direction given by the arrow linking the poles of the Au-hemisphere to the pole of the SiO2-hemispheres, but their reorientation is predominantly driven by sudden tumbling events caused local torques (see the mechanism below).

7.2 Island hopping mechanism

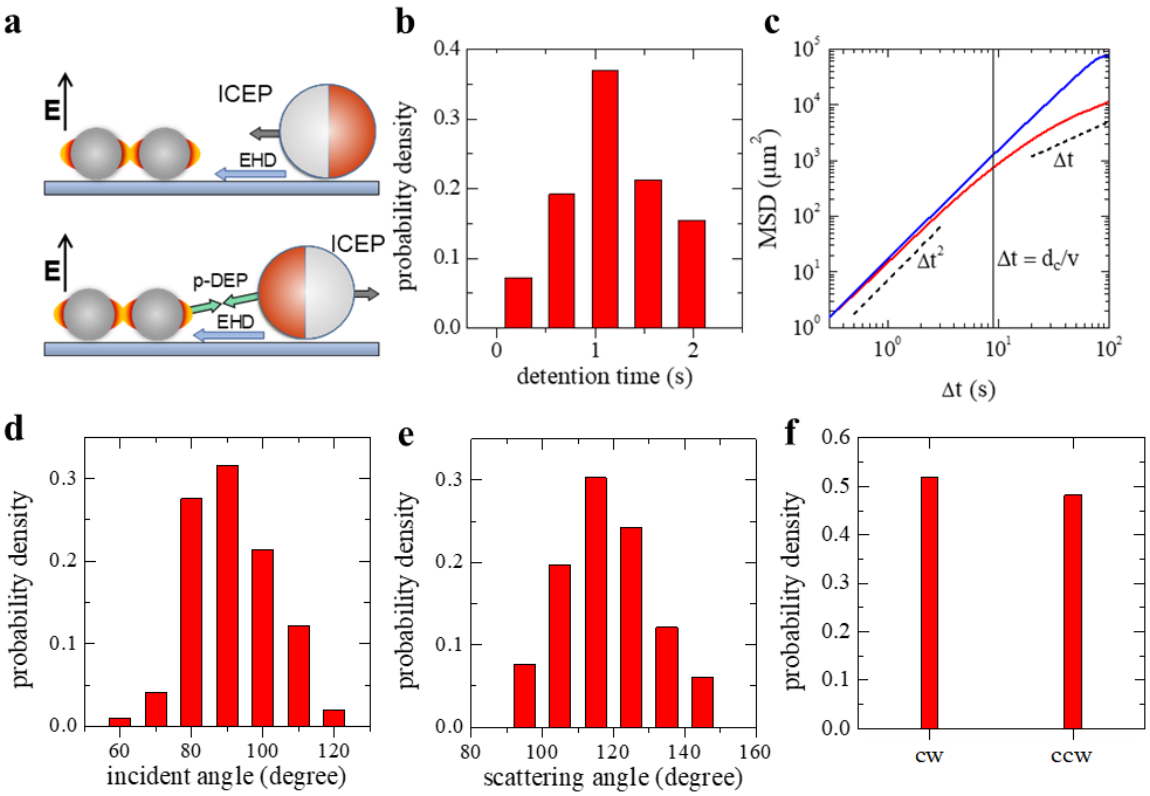

Figure 7.2, Active motion in the presence of island-hopping mechanism. (a) Scheme of the proposed docking-undocking mechanism. (b) Probability density for the detention time of JP colliding against passive islands (see definition in the main text). (c) Mean squared displacement (MSD) of JP plotted using double-logarithmic scale and averaged over 40 individual particle trajectories, (red) with and (blue) without silica islands for E = 0.066 $V\mu m^{-1}$ (d) Probability density for the incident angle (e) Probability density for scattered angle i.e., the angle between the incoming and outgoing velocity vectors. (f) Probability density for the clockwise (cw) and counterclockwise (ccw) rotational direction of JP upon collision with islands.

Charged surfaces wetted by polar fluids and subjected to external electric fields develop slip flows due to the motion of the ions comprised in the electrical double layers. This leads to fluid or particle transport [215], depending on whether the solid surface is fixed (as in the case of charged substrates) or freely suspended (as in the case of charged colloidal particles). A popular example is the migration of micro- and nanoparticles in the direction parallel or antiparallel to an applied DC field, E, with velocities proportional to the applied voltage (linear electrophoresis). Here, (1) the island formation and (2) the active motion of JP is driven by nonlinear electrophoretic effects known as induced-charge electroosmosis (ICEO) and induced-

charge electrophoresis (ICEP) [182, 184, 186, 187,]. In (1), the AC electric field perpendicular to the observation plane sets in motion the electrical double layer of the ITO-coated substrate and, simultaneously, polarizes the particle. The polarization changes the electric field just beneath the particle and drives the induced charges and electrohydrodynamic (EHD) solvent flow along the substrate [216]. The net result is the formation of recirculating electroosmotic rolls, where the current leaves and enters the surface, which in turn lead to an effective mutual attraction or repulsion between particles [217]. For silica colloids, the EHD flows are attractive [200, 201, 202,], consistently with our observation of close-packed islands at $f = 1.5\,\mathrm{kHz}$ (Figure 7.2(b)). In (2), the metallic hemisphere of the JP is more strongly polarized under the applied electric field. This unbalance leads not only to local fluid rolls of different magnitude but also to fluid being drawn from the front (ahead of the silica hemisphere) and ejected behind the gold cap [182, 184,]. Consequently, the JP self-propels in the xy-plane normal to the applied field, in the direction of the dielectric hemisphere (see Figure 7.2(a)).

Ultimately, local hydrodynamic and electric phenomena are, to our understanding, the reason behind the island-microswimmers 'scattering events' reported in Figure 7.1. The docking-undocking mechanism is schematically illustrated in Figure 7.1(a). When a JP swims towards an island with its SiO_2 hemisphere heading, the attractive EHD flows help to bring the two in contact [218], as shown in Figure 6.3(d–i) **(see supplementary video 8)**. Upon contact, local nonuniform electric fields start to play a key role in the JP reorientation. Wang et al. showed that the local electric field nearby a passive silica particle is low beneath the colloid and high across its equator (red regions in Figure 7.2(a) [197]. Thus, permanent attachment occurs due to negative dielectrophoretic (n-DEP) when the JP is able to fit underneath the passive bead, i.e., for $R_{JP}/R_P < 1$. In this work, the JP is larger than the passive spheres forming an island; permanent docking does not take place since positive dielectrophoretic (p-DEP) attracts the metallic hemispheres towards the high E region. The net result is a torque that quickly turns the JP orientation (Figure 7.1(d–i)). Because of this, detention only lasts a few seconds (Figure 7.2(b)), while rotational diffusion would require dozens of seconds to reorient the JP. Hydrodynamic interactions such as those generated by source dipoles also contributes to the quick reorientation [219]. Once the Au hemisphere faces the island, the repulsive backflow due to ICEP is strong enough to force the undocking (bottom sketch in Figure 7.2(a)). We note that particles can also occasionally glide along the surface of an island; this situation occurs when the JP approaches sideways an edge of the island so that contact is not achieved and persistent motion is continued at a distance from the raft, where realigning torques are weak.

The outcome of the scattering events is a JP-island collision that resembles the phenomenon of 'backscattering', even though the Reynolds number of our macroparticles is always much smaller than 1 ($\mathrm{Re} \sim 10^{-6}$). Averaged over several collisions, the overall active Brownian motion of the JP has similarities with the swimming behavior of biological microorganisms undergoing run-and-tumble motion, with the islands acting as turning sites. The run-and-tumble dynamics manifests itself in the MSD of many JP (Figure 7.2(c), red curve), showing a crossover from a ballistic to a diffusive regime at $\Delta t \sim d_c/v$, where v is the mean swimming velocity of the microswimmers and d_c is the mean inter-island distance (here d_c plays the role of mean run length). This behavior is in contrast with the active Brownian motion of free JP, where a transition from ballistic to diffusive motion is found at $\Delta t = \tau_R \sim D_R^{-1}$. This difference was highlight by Solon et al. while comparing the tumbling rate of biological swimmers with the characteristic free reorientation time of ABP [220]. Here, the inverse of the mean travel time between clusters plays the role of a tumbling rate. Importantly, we note that the 'backscattering' does not show up in the MSD because the short-time behavior is dominated by the long ballistic runs.

The angular statistics in Figure 7.2(d–f) further clarify the nature of the JP–island collision events. Figure 7.2(d) shows the probability distribution of the incident angle, which describes how the JP approaches the passive island before contact. The distribution indicates that collisions occur over a range of approach directions, rather than only through head-on impacts. Figure 7.2(e) shows the corresponding scattering angle, defined as the angle between the incoming and outgoing velocity vectors. The distribution is strongly weighted toward large scattering angles, indicating that the JPs often leaves the island in a direction substantially different from its incoming trajectory. This confirms that the passive islands act as reorientation sites for the active particle. Finally, Figure 7.2(f) compares the clockwise and counterclockwise rotation of the JP during the collision. The nearly balanced probability of both rotation directions suggests that the reorientation is not biased toward a preferred handedness, but is instead determined by the local geometry of the collision and the instantaneous orientation of the JP at the island boundary. Together, these angular distributions show that the island-hopping dynamics is not simply a trapping process, but a docking–reorientation–undocking event in which the passive islands redirect the active particle motion. Thus, Figure 7.2(d–f) demonstrates that passive islands act as active scattering centres, they transiently detain the JP, rotate its propulsion direction, and release it along a new trajectory. This microscopic collision mechanism explains the island-hopping motion observed in the trajectories and supports the

interpretation of the island matrix as a structured environment that controls active-particle transport.

7.3 Conclusion

Overall, this chapter shows that passive silica islands strongly influence the motion of electric-field-driven Janus particles. The islands do not act only as static obstacles; instead, they behave as transient turning sites. When a JP collides with an island, it can remain temporarily detained, reorient, and then leave along a new direction, producing an island-hopping type of motion.

This docking and undocking behavior is tentatively attributed to local electric-field gradients and dielectrophoretic interactions between the passive silica particles and the metallic cap of the JP. These interactions can generate a torque on the JP during contact, leading to rapid reorientation before release. The angular statistics support this interpretation by showing that collisions with islands significantly change the outgoing direction of motion, while the rotation direction remains approximately unbiased.

Thus, the passive islands provide a structured environment that controls active-particle transport through repeated detention, reorientation, and release events. This system therefore offers a useful model for studying active motion in heterogeneous crowded environments.

Chapter 8 - **Active colloids in tunable and compressible environments**

8.1 Introduction

In the previous chapters, I studied Janus particle motion in polymer solutions and in heterogeneous island-like obstacle landscapes. In this chapter, I use the tunable active passive colloidal platform established in Chapter 4 to investigate a more ordered form of crowding: dense passive colloidal environments with locally crystalline or polycrystalline structure.

Such environments combine two important aspects of complexity. First, they restrict active motion through crowding and collisions. Second, they possess internal structure, including local order, defects and grain boundaries, which can guide or hinder particle motion in a spatially dependent way. Lastly, the active particle therefore does not move through a featureless viscous background, but through a structured medium whose organization can feed back on its trajectory. Gold-capped silica Janus particles are used as active swimmers, while untreated passive silica particles form the surrounding colloidal matrix. Under the selected AC electric-field conditions, the Janus particles remain actively driven and the passive particles interact repulsively, allowing dense ordered or polycrystalline arrangements to be explored.

This chapter is part of the published article: Venkata Manikantha Sai Ganesh, T., Malhotra, I., Caprini, L., Löwen, H., Palberg, T., and Buttinoni, I. (2026). Active particle in tunable compressible environments. Small Science,6, e202500599.

8.2 Active colloids in tunable colloidal environments

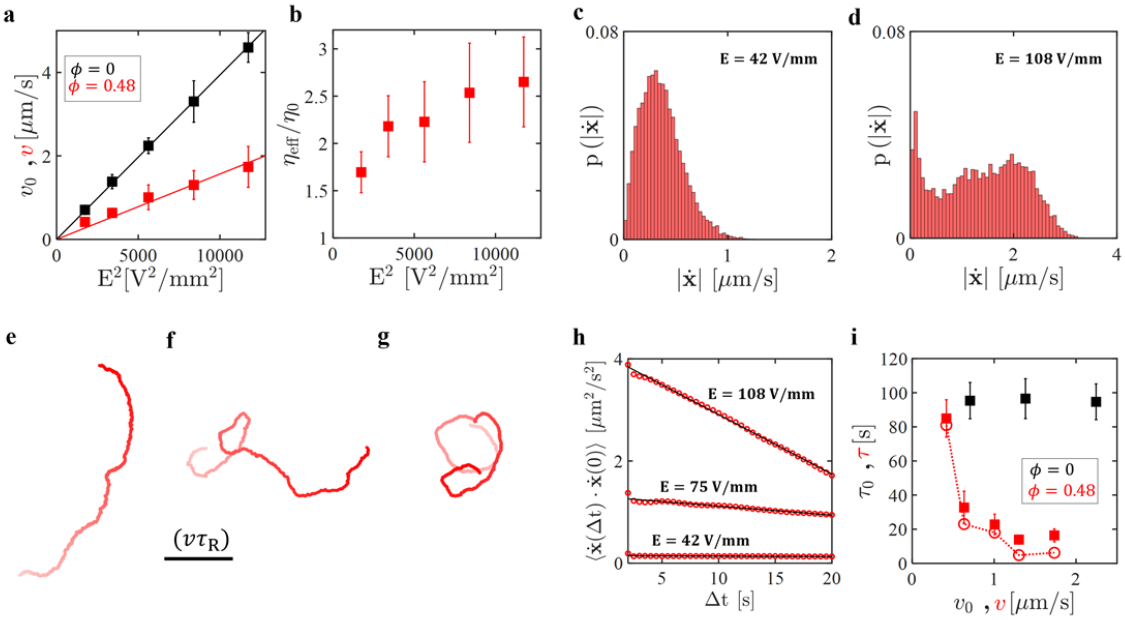

Figure 8.1, Swimming in crowded environments. (a) Mean swimming velocities (black) v_0 and (red) v plotted as a function of the electric-field strength squared E^2 for active particles swimming "freely" ($\phi = 0$) or cruising in colloidal environments of packing fraction $\phi = 0.48$. The solid lines are linear fits crossing the origin. (b) Ratio between the effective viscosity η_{eff} of the colloidal environment and the water viscosity η_0, calculated as described in the text. (c–d) Normalized histograms of the instantaneous speed $|\dot{x}|$ under an applied electric field: (c) E = 42 V/mm and (d) E = 108 V/mm. (e–g) Trajectories of active particles cruising in colloidal environments of packing fraction $\phi = 0.48$ under applied electric fields: (e) E = 42 V/mm, (f) E = 75 V/mm, and (g) E = 108 V/mm. The scale bar is dynamic and corresponds to $(v\tau_R)$ for all trajectories, where v is the average swimming velocity and τ_R is the rotational Brownian time (defined in the text). The color indicates the time: from t = 0 (white) to t = 500 s (red). (h) Time autocorrelation functions of $\dot{x}$ for the trajectories shown in (e–g). The solid lines are linear fits. (i) Mean persistence times τ (red symbols, $\phi = 0.48$) and τ_0 (black symbols, $\phi = 0$) plotted against v. The filled symbols are obtained from experiments, while the empty symbols (linked by the dotted line) are from numerical simulations matching the experimental values of v. In all panels, the error bars represent the standard deviations

As established in Chapter 4, the passive silica monolayer provides a field-tunable polycrystalline environment. By varying the packing fraction and the applied AC electric field at f=20 kHz, the passive matrix can be tuned from a weakly ordered Brownian monolayer to a more ordered structure with enhanced local hexagonal correlations. In this chapter, the same platform is used as a controlled crowded environment to investigate how active Janus particles move through, interact with, and become reoriented by a structured passive colloidal matrix.

In this section, we show experimentally that a tunable colloidal environment strongly modifies the motion of self-propelled particles moving through it. By varying the amplitude of the applied AC electric field, we simultaneously control the propulsion of the active particles and their interaction with the surrounding passive colloidal matrix. The active particles are silica microspheres of radius R_a=2.5 μm, half-coated with gold. Under the AC electric field, these Janus particles self-propel along the substrate. In the absence of passive colloids, the swimming speed increases with the square of the electric field, as shown in Figure 8.1 (a) (black symbols). In contrast, when the particles move in a crowded colloidal environment (ϕ=0.48), their mean velocity is reduced (Figure 8.1 (a), red symbols), indicating an increased effective resistance from the surrounding medium. This slowdown can be quantified by comparing the effective viscosity experienced by the particles. The ratio between the effective viscosity and the solvent viscosity increases with the electric field (Figure 8.1 (b)), demonstrating that the colloidal environment becomes dynamically more restrictive at higher field strengths.

To gain further insight, we analyze the instantaneous velocity distributions. At moderate field strength (E=42 V/mm), the velocity distribution remains peaked around a finite value (Figure 8.1(c)), similar to the behaviour of free swimmers. However, at higher field strength (E=108 V/mm), the distribution broadens and develops a significant contribution near zero velocity (Figure 8.1(d). This indicates intermittent dynamics, where particles alternate between mobile and nearly arrested states. This behaviour is directly visible in the particle trajectories. Representative trajectories at different electric fields are shown in Figure 8.1(e-g). At low field, particles move along relatively extended and smooth paths (Figure 8.1(e), **Supplementary Video 9 §9.9**). As the field increases, the trajectories become more irregular (Figure 8.1(f)), and at high field, they show pronounced circular motion (Figure 8.1(g), **Supplementary Video 10 §9.9**), consistent with frequent trapping by the surrounding colloidal structure. To quantify the temporal correlations in the motion, we compute the velocity autocorrelation function. As shown in Figure 8.1(h), the autocorrelation decays faster at higher electric fields, indicating shorter persistence of the particle motion. This effect is summarized by extracting the persistence time τ, which decreases as the propulsion strength increases (see Figure 8.1(i)).

The same qualitative behaviour is also observed in numerical simulations, as shown in Figure 8.2, although caging events occur more frequently and are generally longer-lived in the simulations. This difference is likely related to the geometrical constraints of the numerical model. In the simulations, the system is treated as perfectly two-dimensional**,** meaning that both active and passive particles are confined to the same plane and interact as disks. As a result, the

active particle cannot partially bypass or move over the passive monolayer, which increases the probability of becoming trapped inside cages formed by neighbouring passive particles.

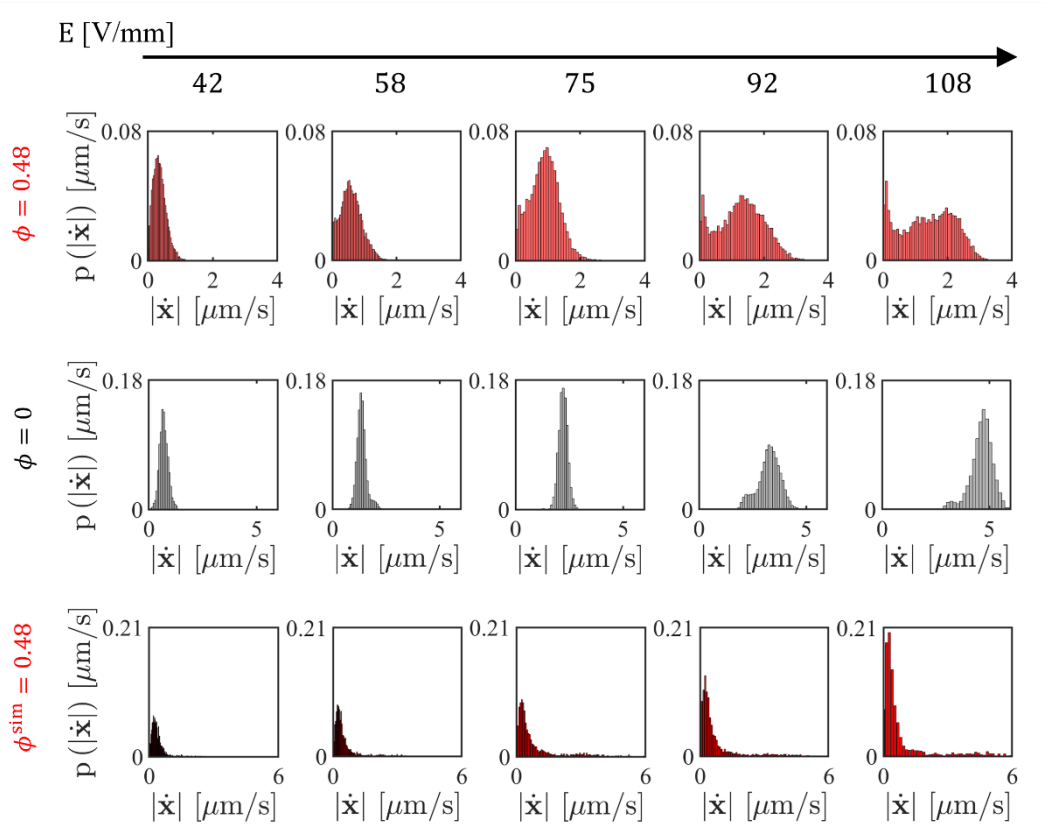

Figure 8.2, Normalized histograms of the instantaneous velocities |ẋ| of approximately 20 active particles swimming throughout a colloidal monolayer at ϕ = 0.48 (red histograms) and ϕ = 0 (gray histograms) for five different values of E, as indicated by the arrow. The figure highlights the bimodal distributions observed in the colloidal bath, as opposed to the 'free' case (ϕ = 0). Note that, for a given E, the mean swimming velocity of 'free' active particles is systematically larger.

In the experiments, however, the active Janus particles are larger than the passive particles and therefore protrude above the colloidal monolayer. This out-of-plane height difference allows the swimmer to interact with the passive matrix in a less strictly two-dimensional manner. Consequently, the active particle can more easily escape from local cages or move through defects in the monolayer, reducing the frequency of long trapping events compared with the simulations. This interpretation is supported by **supplementary video 9**, where the size mismatch is reduced. In this experiment, an active Janus particle with radius $R_a = 2.5\mu m$ moves through a colloidal monolayer of Brownian microspheres with radius $R_a = 2.1\mu m$ at an area fraction of ϕ=0.48under an applied electricfield $E = 108 V mm^{-1}$. Because the active and

passive particles have more similar size, the active particles are more strongly confined within the monolayer plane and is frequently caged by the neighbours. This observation supports the idea that particle size mismatch and out of plane motion in the experiments reduce caging, whereas the strictly two-dimensional simulations enhance it.

Finally, we compare the persistence time with the swimming velocity. Figure 8.1(i)shows that, in the crowded environment (ϕ=0.48, red symbols), the persistence time decreases strongly with increasing velocity, whereas in the absence of passive particles (ϕ=0, black symbols), it remains approximately constant. This demonstrates that the reorientation dynamics in the colloidal environment are not governed solely by rotational diffusion, but are strongly influenced by interactions with the surrounding passive matrix.

According to our description, $\tau \propto v^{-1}$ since more distance travelled means more reorientation events. We verified this dependence by performing numerical simulations where v (swimming velocity of the individual active particles) and K (strength of the dipolar interactions) are decoupled. The results are shown in Figure 8.3 in most instances, τ and v are inversely proportional suggesting that each reorientation event depends weakly on the local interaction strength K. Overall, here we consistently show that increasing the electric field enhances both propulsion and interactions with the environment. As a result, active particles experience slower average motion, intermittent caging, and reduced directional persistence in crowded colloidal environments.

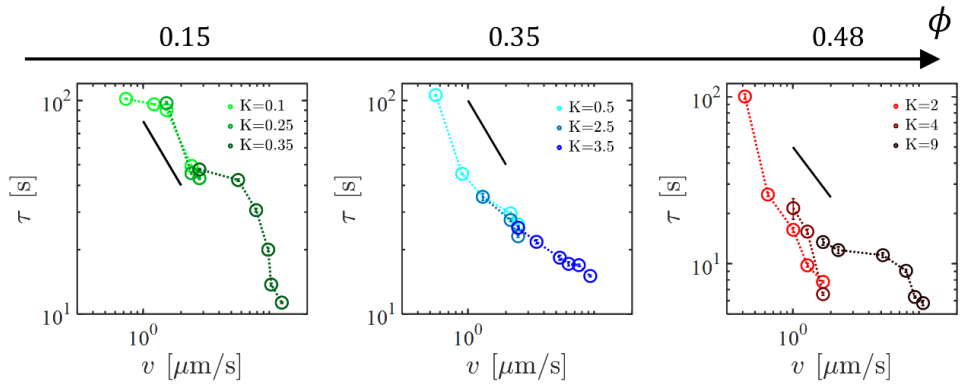

Figure 8.3, Log-log plot of the numerical persistence time τ as function of the mean swimming velocity v in colloidal monolayers at different area fraction (ϕ, see arrow). The colors correspond to the strength K of the dipolar interactions, which in these particular simulations varies independently of v. The solid black lines have slope −1, suggesting that the $\tau \propto v^{-1}$ approximately holds for a broad range of packing fractions and interaction strengths.

8.3 Spontaneous chiralization mechanism

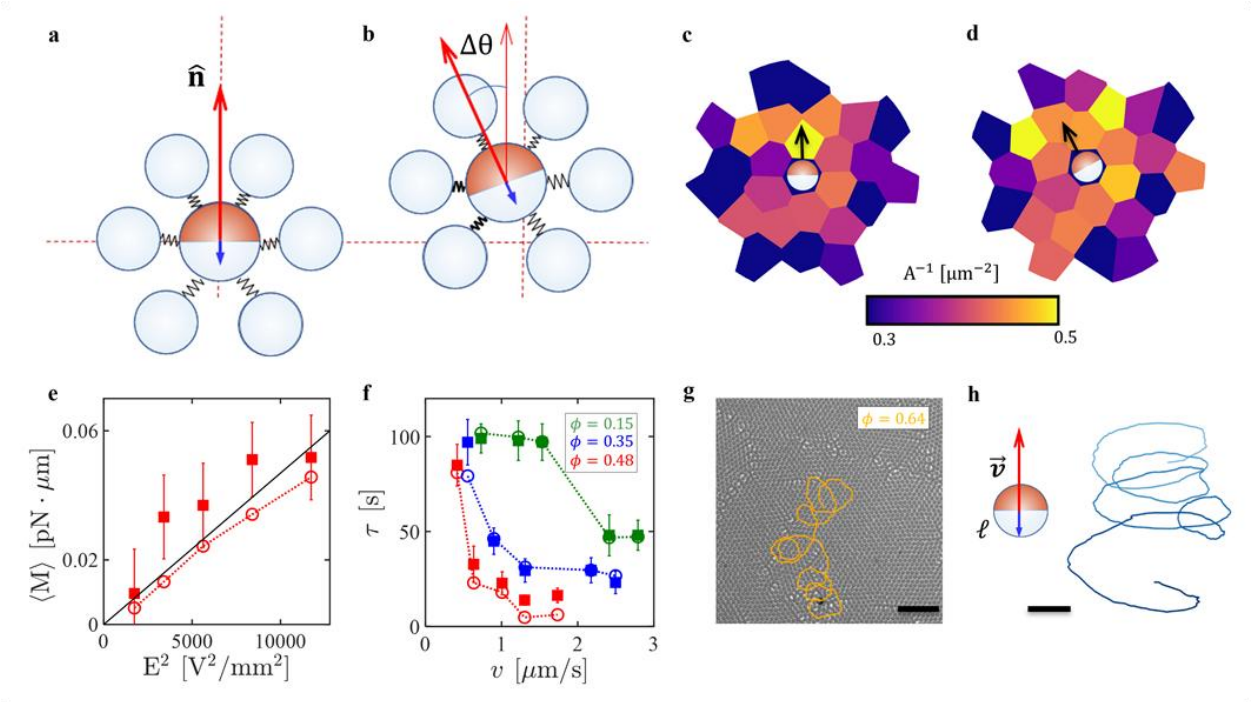

Figure 8.4, Self-sustaining reorientation. (a–b) Sketch of the reorientation mechanism, as modelled in numerical simulations, causing the drop of the persistence time of the active particle in colloidal environments. (a) An active particle moving with the Au cap heading produces a swimming force $f_s \hat{n}$ in the same direction. (b) Upon rotation by an angle Δθ, the colloidal environment is compressed, generating a torque due to dipolar repulsion between passive particles and the silica back hemisphere of the active colloid. (c–d) Voronoi tessellation of the environment (c) before and (d) after a rotation. The color code indicates the local packing, i.e., the inverse area of the Voronoi cell. (e) Mean torque experienced by an active Janus particle swimming throughout a monolayer at area fraction ϕ = 0.48 for different applied electric fields. Solid and empty symbols correspond to experiments and simulations, respectively. The red dashed line connects the numerical data, and the black solid line marks the linear relationship between ⟨M⟩ and E^2. (f) Persistence time τ as a function of the average velocity v in colloidal environments at different ϕ, as indicated in the legend. The filled symbols correspond to the experiments, while the empty symbols are from numerical simulations matching the experimental values of v. (g) Helical active trajectory of 4-minutes duration observed in experiments when the area fraction of the surrounding colloidal bath is ϕ = 0.64. The scale bar corresponds to 20 μm. (h) Numerical trajectory of an active particle swimming at velocity v = 2.4 μm/s in colloidal environments at ϕ = 0.35. The colour indicates the time, from t = 0 (light blue) to t = 40 s (blue). The lever arm ℓ = 0.4 μm determining the torque is shown as a blue arrow pointing from the geometric particle center to the interaction center. The scale bar corresponds to 1 μm.

In addition to the slowdown and reduced persistence discussed above, active particles in crowded colloidal environments exhibit a striking qualitative change in their trajectories: the emergence of spontaneous chiral motion. Under certain conditions, particles no longer follow approximately straight or randomly reoriented paths, but instead develop sustained circular or helical trajectories. This behavior is summarized in Figure 8.4. The mechanism is illustrated schematically in Figure8.4 (a–b). As an active particle moves through the colloidal environment, it locally compresses the surrounding passive particles. Because this environment is disordered, such compression is typically asymmetric. As a result, the particle experiences an effective torque that continuously reorients its direction of motion. When this torque persists over time, it leads to curved trajectories. The structural origin of this effect is highlighted using Voronoi tessellation in Figure8.4 (c–d). These maps show that the local packing of the passive particles around the active particle becomes anisotropic during motion. This asymmetry in the surrounding structure is directly correlated with the emergence of directional rotation. The strength of this rotational behavior depends on the propulsion strength. As shown in Fig. Figure8.4 (e), the magnitude of the effective torque ($\langle M \rangle = \xi R \langle \dot{\theta} \rangle$, where $\langle \dot{\theta} \rangle$ is the mean angular speed) increases with the electric field, indicating that stronger propulsion enhances the interaction with the surrounding colloidal matrix. At the same time, Figure8.4 (f) shows that the persistence time decreases with increasing swimming speed, consistent with more frequent reorientation events. A direct manifestation of this effect is observed in particle trajectories. In Figure8.4 (g-h), the active particles follow clearly curved and, in some cases, helical paths over extended periods. Importantly, the direction of rotation (clockwise or counterclockwise) is not predetermined but emerges spontaneously from the local configuration of the environment. Both directions are observed with equal probability, indicating that the chiral motion does not arise from an intrinsic asymmetry of the particle, but from interactions with the surrounding medium. We further observe that this spontaneous chiralization depends sensitively on the properties of the colloidal environment. At low packing fractions, the motion remains largely non-chiral, as interactions with passive particles are weak. As the packing fraction increases, circular trajectories become more frequent. However, at very high densities, strong caging effects suppress sustained rotation, limiting the development of long-lived chiral motion. Overall, Figure8.4 (a-h), demonstrates that spontaneous chiralization emerges from the interplay between active propulsion and the structured, yet disordered, colloidal environment (**see supplementary video 10**). The environment not only slows down the particles and reduces their persistence, but can also induce sustained rotational motion, providing a new mechanism for controlling active particle trajectories without modifying particle design.

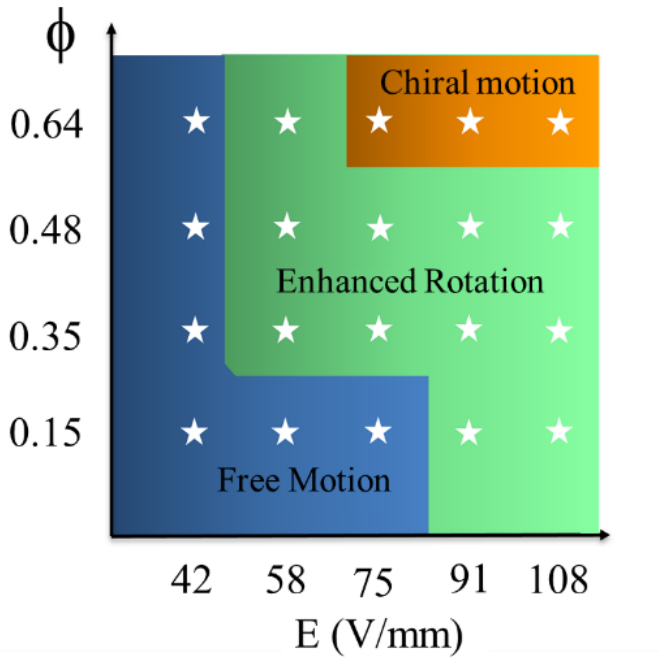

Figure 8.5, Qualitative diagram showing the type of active motion observed as function of the applied electric field E and packing fraction φ of the environment. (blue) "Free motion" where $\tau \approx \tau_R$. (green) "Enhanced rotation" where $\tau < \tau_R$ but trajectories are not fully circular. (orange) "Chiral motion" where the active particles undergo helical motion with well-defined orbit's radius.

The different dynamical regimes observed in the experiments are summarized in Figure 8.5 as a qualitative state diagram in the plane of electric field strength, E, and packing fraction, ϕ. This diagram shows that the emergence of chiral motion is not controlled by activity alone, but by the combined effect of propulsion strength and crowding. At low electric fields and low packing fractions, the particles remain in a free-motion regime, where the rotational persistence time is much larger than the orientational decorrelation time, $\tau \gg \tau_R$. In this regime, particle–environment interactions are too weak or too infrequent to generate sustained curvature.

At intermediate values of E and ϕ, the particles enter an enhanced-rotation regime, where interactions with the passive colloidal matrix become strong enough to increase reorientation, but the trajectories do not yet form well-defined circular or helical orbits. This corresponds to the condition $\tau < \tau_R$, where environmental collisions and local packing asymmetries dominate over free rotational diffusion. At high packing fraction and sufficiently strong electric field, the system enters the chiral-motion regime. Here, the active particle experiences persistent asymmetric confinement by the surrounding passive particles, leading to sustained curved trajectories with a well-defined orbit radius.

Thus, Figure 8.5 provides a compact summary of how spontaneous chiralization depends on both field-driven activity and the structural density of the passive environment. Chiral motion appears only within a restricted region of parameter space: the activity must be strong enough to compress and reorganize the surrounding passive particles, while the packing fraction must be high enough to generate persistent asymmetric contacts. This confirms that the chirality is not an intrinsic property of the Janus particle, but an emergent consequence of active motion in a crowded colloidal matrix.

8.4 Summary and conclusion

In this chapter, I used the tunable active–passive colloidal platform established earlier to study Janus-particle motion in dense, structured passive environments. The passive colloidal monolayer was controlled by the applied AC electric field, which allowed the background to be tuned from a less ordered state toward a more quenched, locally ordered structure at fixed particle concentration.

The results show that the passive environment strongly modifies active-particle dynamics. As the surrounding monolayer becomes more structured, the motion of the Janus particles is no longer described by simple active Brownian motion. Instead, the swimmer reorientation becomes coupled to its propulsion speed and to local rearrangements in the passive matrix. In particular, the persistence time decreases with increasing swimming velocity, following approximately $\tau \propto v^{-1}$. Similar reductions of persistence time have been reported in other complex environments, such as polymer solutions and colloidal glasses [221, 222,].

At sufficiently high propulsion speeds, the active particle can undergo helical or orbit-like motion, even though neither the Janus particle nor the passive particles are intrinsically chiral. This indicates that chirality can emerge dynamically from the coupling between active propulsion, anisotropic particle–environment interactions, and local compression of the surrounding passive colloids. The mechanism therefore differs from chiral motion caused by asymmetric particle shape or permanent bound clusters [223].

The same experimental results were recently revised by De Corato et al. using a memory-free model based on local density variations, anisotropic interactions, and advection terms [224, 225,]

Overall, this chapter shows that dense passive colloidal environments can be used not only to hinder or scatter active particles, but also to tune their reorientation dynamics in situ. The observed coupling between swimmer activity and environmental compressibility provides a useful route to understanding active motion in structured, crowded media. These findings also suggest that similar mechanisms may occur in other microswimmer systems moving through compressible or microstructured environments.

Chapter 9 - **Summary and conclusion**

9.1 Summary of the thesis

This thesis has explored the dynamics of active colloidal systems driven by AC electric fields, with a particular focus on their behaviour in complex, crowded, and structured environments. A central contribution of this work is the development of a versatile experimental platform that enables external control of Janus particle propulsion by tuning the amplitude and frequency of an applied AC electric field. This platform provides a reproducible way to control particle activity, propulsion direction, and particle–environment coupling under well-defined experimental conditions.

Using this platform, two different types of crowded environments were compared: molecularly crowded polymer solutions and colloidally crowded passive-particle matrices. In PEG polymer solutions, the surrounding medium affects swimming mainly through increased viscosity, polymer-induced hindrance, and intermittent particle–surface or particle–polymer interactions. In contrast, colloidal crowded environments influence swimming through direct steric constraints, local structural order, caging, scattering, and reorientation by neighbouring passive particles. This comparison shows that crowding cannot be described only by an increase in effective viscosity; the length scale and structure of the crowded environment play a decisive role in determining active-particle motion.

In polymeric media, active particle motion deviates from simple persistent swimming and exhibits strongly reduced mobility, intermittent trapping, and enhanced trajectory fluctuations. These findings show that propulsion alone is insufficient to predict particle dynamics in complex fluids, because the surrounding medium can strongly modify the effective swimming performance. The results therefore establish PEG solutions as a controlled molecularly crowded environment for studying how viscosity and polymer-mediated interactions affect AC-driven Janus particle motion.

Separately from the crowding studies, this thesis also demonstrated electrically controlled cargo transport using Janus particles in PEG polymer solutions. Here, the main result is not the effect of crowding itself, but the realization of a complete field-controlled transport cycle consisting of cargo pickup, loaded transport, release, and load-free return. This was achieved by using the AC field frequency to switch between propulsion modes and cargo interaction states. Thus, cargo transport represents an independent functionality of the same experimental platform,

showing that AC-driven Janus particles can be used not only to probe complex environments, but also to perform controlled microscale manipulation.

The role of environmental structure was then examined in colloidally crowded systems, using the same field-controlled platform to realize two conceptually different types of passive environments. By tuning the field frequency, the passive silica particles were organized either into spatially inhomogeneous island structures or into more homogeneous polycrystalline matrices. These two cases were not chosen as independent examples, but as complementary model systems for understanding active motion in structured environments.

In the island regime, compact and nearly incompressible passive clusters are separated by open regions of free space. Active Janus particles therefore alternate between persistent motion in open regions and discrete collision events at island boundaries. These collisions produce transient detention, reorientation, and release, giving rise to a backscattering or island-hopping mechanism. This behaviour provides a physical route to run-and-tumble-like transport in a non-biological active system, where the turning events are imposed by the structured environment rather than by an internal swimming cycle.

In contrast, the polycrystalline regime represents a more homogeneous crowded matrix in which the Janus particles remain in continuous contact with surrounding passive particles. Here, the passive environment acts less as a set of isolated obstacles and more as a tunable medium with field-controlled structure and effective stiffness. This allows the influence of local order, caging, and matrix resistance on active motion to be studied systematically. In this regime, the interaction between propulsion and the surrounding colloidal matrix leads not only to slowing and reduced persistence, but also to the first observation of spontaneous chiral motion of electrically driven Janus particles in such a crowded passive monolayer.

Together, these two regimes show that the thesis follows a purposeful progression towards understanding motion and motion control in complex environments. The same active particles and the same external control parameter are used to move from isolated obstacle scattering to continuous matrix-mediated transport. This demonstrates that structured passive environments can do more than hinder active motion: they can redirect, reorient, confine, and even chiralize active trajectories.

Finally, the results presented in this thesis show that active colloids cannot be understood only from the properties of the swimmer itself. Instead, their dynamics emerge from the coupling between field-controlled activity, particle–particle interactions, and the structure of the

surrounding environment. This coupling determines whether active particles move persistently, become slowed or trapped, scatter from obstacles, transport cargo, or develop new modes of motion such as spontaneous chirality.

It is in this sense that this work aligns with the broader idea of functional active materials, where functionality does not arise from an isolated active unit alone, but from the interaction between activity, external control, and environmental structure. The experimental platform developed here therefore provides a step towards designing active colloidal systems in which motion, transport, and trajectory control can be programmed through the properties of the surrounding medium.

9.2 Outlook

The findings of this thesis open several promising directions for future research. The next step is not simply to increase experimental resolution or add more sophisticated instrumentation, but to introduce additional levels of physical complexity in a controlled way. One direction is to study active motion in environments with combined forms of crowding, for example systems where polymeric viscosity, passive obstacles, confinement, and structural heterogeneity act simultaneously. Such experiments would help clarify how different environmental effects compete or cooperate in controlling active-particle transport.

A second important direction is the extension from quasi-two dimensional systems to three-dimensional environments. The experiments presented here provide controlled model systems in which the main interactions can be isolated and interpreted. However, many natural and biological environments are three-dimensional, heterogeneous, and dynamically reorganizing. Moving towards 3D systems would therefore allow the mechanisms identified in this thesis, such as hindrance, scattering, caging, and chiralization, to be tested under more realistic geometrical constraints.

A further step is to investigate active-particle motion in biologically relevant media, where complexity and three-dimensional structure are naturally present. Biological environments provide crowded, viscoelastic, heterogeneous, and dynamic surroundings, and therefore offer a natural testing ground for the concepts developed in this thesis. In such systems, the challenge will be to determine which mechanisms remain robust and which new effects arise from the additional complexity. It is therefore in response to these scientific questions that the

experimental approach will need to be further developed. Improvements in tracking, local structure characterization, and environmental control would not be goals by themselves, but necessary tools for investigating active motion in increasingly complex, three-dimensional, and biologically relevant environments.

Overall, with the developments and findings presented in this thesis, I hope to have made a modest contribution to the understanding of swimming in complex environments. At the same time, this work identifies several rewarding future directions and suggests a path for their systematic investigation.

Appendix

Appendix A Video information

All supplementary videos are available via Seafile. Please scan the link to access them.

Supplementary Video 1 Island-formation by self-assembly of silica passive particles upon applying AC electric fields (E = 0.066 V/μm). The field switching frequency was kept constant at f = 1.5 kHz. The video was recorded at 40 × magnification, where the scale bar corresponds to 5 μm. The recording speed was set to 100 FPS rendered at 5 × speed up.

Supplementary Video 2 Dissolution of islands when turning off the AC electric field (E = 0 V/μm) and fluid phase recovery by thermal diffusion. The video was recorded at 20 × magnification, where the scale bar corresponds to 10 μm. The recording speed was set to 2 FPS rendered at 10 × speed up.

Supplementary Video 3 Structural evolution of a colloidal monolayer of passive silica spheres subjected to electric fields of different magnitude (as indicated in the legend). Recording speed: 10 fps. Playing speed: 200 fps. Scale bar: 20 μm.

Supplementary Video 4 Active Janus particle undergoing trapped motion in 100mg/mL PEG 6000 medium under applied electric field E = 0.033 V/μm. Recording speed: 10 fps. Playing speed: 40 fps. Scale bar: 20 μm**.**

Supplementary Video 5 Active Janus particle undergoing jittery motion in 100mg/mL PEG 6000 medium under applied electric field E = 0.066 V/μm. Recording speed: 10 fps. Playing speed: 40 fps. Scale bar: 20 μm**.**

Supplementary Video 6 Active Janus particle undergoing straight motion in 100mg/mL PEG 6000 medium under applied electric field E = 0.133 V/μm. Recording speed: 10 fps. Playing speed: 40 fps. Scale bar: 20 μm**.**

Supplementary Video 7 Demonstrating cargo transport in viscous medium under applied electric field E = 0.133 V/μm in 100mg/mL PEG 6000 medium. Recording speed: 10 fps. Playing speed: 40 fps. Scale bar: 20 μm**.**

Supplementary Video 8 Island-microswimmers interaction and gold-cap orientation at applied AC electric field (E = 0.066 V/μm at constant frequency f = 1.5 kHz). The video was recorded

at 40 × magnification, where the scale bar corresponds to 5 μm. The recording speed was set to 100 FPS rendered at 5 × speed up.

Supplementary Video 9 Active Janus particle cruising in a colloidal monolayer of Brownian microspheres (ϕ = 0.48) of similar size (active particle radius $R_a = 2.5\mu m$, passive particle radius $R_p = 2.1\mu m$)) under applied electric field E = 108 V/mm.

Supplementary Video 10 Active Janus particle undergoing helical motion in a colloidal monolayer of Brownian microspheres (ϕ = 0.64) under applied electric field E = 108 V/mm. Recording speed: 2 fps. Playing speed: 40 fps. Scale bar: 20 μm**.**

Appendix B

Use of AI Tools

This appendix documents the use of AI-based tolls during the preparation of this thesis. All scientific content, data analysis, interpretations, and conclusions were independently developed by the author. AI tools were used exclusively in a supportive role for language refinement, code debugging, formatting assistance, and conceptual clarification. The author retained full editorial and scientific control at all times, and all AI-generated outputs are critically reviewed, verified and selectively integrated.

Overview of AI Usage

The primary mode of AI assistance ant their specific roles are summarized in Table B.1. In particular, AI tools supported:

- Written communication and language quality for non-native English author,
- Code-related debugging and syntax clarification,
- Preliminary explanations of complex topics, treated as non-authoritative and independently verified.

AI tool	Used for	Purpose and scope	When/Where
ChatGPT	Language refinement, formatting suggestions, Python programs debugging and conceptual clarification.	Improving grammar, academic tone; suggesting alternative phrasings for author developed ideas; resolving syntax -related issues in Python programs written by author, providing preliminary explanations of complex concepts, all of which independently verified and critically assessed.	Throughout the thesis.
Grammarly	Grammar, punctuation, and stylistic correction.	Final proof reading to enhance grammatical accuracy and consistency of academic writing, without altering scientific content or authorial intent.	Final proof-reading phase.

Table B.1, Overview of AI-based tolls used during the preparation of the thesis. AI assistance was limited to supportive talks; all outputs were reviewed, verified, and incorporated under full authorial control.

Bibliography

1 Z. Wang, F. Wang, Y. Peng, Z. Zheng, and Y. Han, *Science*, 2012, **338**, 87–90. Imaging the homogeneous nucleation during the melting of superheated colloidal crystals.

2 R. Ganapathy, M. R. Buckley, S. J. Gerbode, and I. Cohen, *Science*, 2010, **327**, 445–448. Direct measurements of island growth and step-edge barriers in colloidal epitaxy.

3 U. Gasser, E. R. Weeks, A. Schofield, P. N. Pusey, and D. A. Weitz, *Science*, 2001, **292**, 258–262. Real-space imaging of nucleation and growth in colloidal crystallization.

4 S. C. Glotzer and M. J. Solomon, *Nat. Mater.*, 2007, **6**, 557–562. Anisotropy of building blocks and their assembly into complex structures.

5 F. Li, D. P. Josephson, and A. Stein, *Angew. Chem. Int. Ed.*, 2011, **50**, 360–388. Colloidal assembly: the road from particles to colloidal molecules and crystals.

6 J. Lahann, *Small*, 2011, **7**, 1149–1156. Recent progress in nanobiotechnology: compartmentalized micro- and nanoparticles via electrohydrodynamic co-jetting.

7 R. K. Shah, J.-W. Kim, and D. A. Weitz, *Adv. Mater.*, 2009, **21**, 1949–1953. Janus supraparticles by induced phase separation of nanoparticles in droplets.

8 J. Xu, D. H. C. Wong, J. D. Byrne, K. Chen, C. Bowerman, and J. M. DeSimone, *Angew. Chem. Int. Ed.*, 2013, **52**, 6580–6589. Future of the particle replication in nonwetting templates (PRINT) technology.

9 C. J. Hernandez and T. G. Mason, *J. Phys. Chem. C*, 2007, **111**, 4477–4480. Colloidal alphabet soup: monodisperse dispersions of shape-designed lithoparticles.

10 R. F. Shepherd, J. C. Conrad, S. K. Rhodes, D. R. Link, M. Marquez, D. A. Weitz, and J. A. Lewis, *Langmuir*, 2006, **22**, 8618–8622. Microfluidic assembly of homogeneous and Janus colloid-filled hydrogel granules.

11 S. Y. Teh, R. Lin, L. H. Hung, and A. P. Lee, Lab Chip, 2008, 8, 198–220. Droplet microfluidics.

12 J. A. Champion, Y. K. Katare, and S. Mitragotri, *Proc. Natl. Acad. Sci. U.S.A.*, 2007, **104**, 11901–11904. Making polymeric micro- and nanoparticles of complex shapes.

13 P. G. de Gennes, *Angew. Chem. Int. Ed.*, 1992, **31**, 842–845. Soft matter (Nobel lecture).

14 A. Walther and A. H. Müller, *Soft Matter*, 2008, **4**, 663–668. Janus particles.

15 A. Walther and A. H. Müller, Chem. Rev., 2013, 113, 5194–5261.

16 J. Hu, S. Zhou, Y. Sun, X. Fang and L. Wu, Chem. Soc. Rev., 2012, 41, 4356–4378.

17 L. Hong, A. Cacciuto, E. Luijten, and S. Granick, *Nano Lett.*, 2006, **6**, 2510–2514. Clusters of charged Janus spheres.

18 K. J. M. Bishop, C. E. Wilmer, S. Soh and B. A. Grzybowski, Small, 2009, 5, 1600–1630. Nanoscale forces and their uses in self-assembly.

19 Q. Chen, J. K. Whitmer, S. Jiang, S. C. Bae, E. Luijten, and S. Granick, *Science*, 2011, **331**, 199–202. Supracolloidal reaction kinetics of Janus spheres.

20 C. Casagrande, P. Fabre, E. Raphaël, and M. Veyssié, *Europhys. Lett.*, 1989, **9**, 251–255. Janus beads: realization and behaviour at water/oil interfaces.

21 C. Kurzthaler, C. Devailly, J. Arlt, T. Franosch, W. C. K. Poon, V. A. Martinez, and A. T. Brown, *Phys. Rev. Lett.*, 2018, **121**, 078001. Probing the spatiotemporal dynamics of catalytic Janus particles with single-particle tracking and differential dynamic microscopy.

22 C. Bechinger, R. Di Leonardo, H. Löwen, C. Reichhardt, G. Volpe, and G. Volpe, *Rev. Mod. Phys.*, 2016, **88**, 045006. Active particles in complex and crowded environments.

23 X. Ju, C. Chen, C. M. Oral, S. Sevim, R. Golestanian, M. Sun, *et al.*, *ACS Nano*, 2025, **19**, 24174–24334. Technology roadmap of micro/nanorobots.

24 K. K. Dey, F. Wong, A. Altemose, and A. Sen, *Curr. Opin. Colloid Interface Sci.*, 2016, **21**, 4–13. Catalytic motors – quo vadimus?

25 X. Ju, C. Chen, C. M. Oral, S. Sevim, R. Golestanian, M. Sun, N. Bouzari, X. Lin, M. Urso, J. S. Nam, and Y. Cho, *ACS Nano*, 2025, **19**, 24174–24334. Technology roadmap of micro/nanorobots.

26 J. Kim, P. Mayorga-Burrezo, S. J. Song, C. C. Mayorga-Martinez, M. Medina-Sánchez, S. Pané, and M. Pumera, *Chem. Soc. Rev.*, 2024, **53**, 9190–9253. Advanced materials for micro/nanorobotics.

27 Y. Mu, L. Lei, J. Zheng, W. Duan, Z. Wang, J. Tang, Y. Gao, and Y. Wang, *ACS Nano*, 2022, **16**, 6801–6812. Binary phases and crystals assembled from active and passive colloids.

28 I. Buttinoni, G. Volpe, F. Kümmel, G. Volpe, and C. Bechinger, *J. Phys. Condens. Matter*, 2012, **24**, 284129. Active Brownian motion tunable by light.

29 K. Kroy, D. Chakraborty, and F. Cichos, *Eur. Phys. J. Spec. Top.*, 2016, **225**, 2207–2225. Hot microswimmers.

30 P. Fischer and A. Ghosh, *Nanoscale*, 2011, **3**, 557–563. Magnetically actuated propulsion at low Reynolds numbers: towards nanoscale control.

31 S. J. Ebbens and D. A. Gregory, *Acc. Chem. Res.*, 2018, **51**, 1931–1939. Catalytic Janus colloids: controlling trajectories of chemical microswimmers.

32 E. V. Novak, E. S. Pyanzina, and S. S. Kantorovich, *J. Phys. Condens. Matter*, 2015, **27**, 234102. Behaviour of magnetic Janus-like colloids.

33 M. Z. Bazant, M. S. Kilic, B. D. Storey, and A. Ajdari, *Adv. Colloid Interface Sci.*, 2009, **152**, 48–88. Towards an understanding of induced-charge electrokinetics at large applied voltages in concentrated solutions.

34 S. Gangwal, O. J. Cayre, and O. D. Velev, *Langmuir*, 2008, **24**, 13312–13320. Dielectrophoretic assembly of metallodielectric Janus particles in AC electric fields.

35 R. Suzuki, H.-R. Jiang, and M. Sano, *arXiv*, 2011, arXiv:1104.5607. Validity of fluctuation theorem on self-propelling particles.

36 C. Shen, Z. Jiang, L. Li, J. F. Gilchrist, and H. D. Ou-Yang, *Micromachines*, 2020, **11**, 334. Frequency response of induced-charge electrophoretic metallic Janus particles.

37 J. Yan, M. Han, J. Zhang, C. Xu, E. Luijten, and S. Granick, *Nat. Mater.*, 2016, **15**, 1095–1099. Reconfiguring active particles by electrostatic imbalance.

38 S. Saad, Diffusiophoresis of Active Colloids: From Synthesis to Dynamics in Complex Media, PhD thesis, 2020.

39 P. Kumar and R. Chakrabarti, *Phys. Chem. Chem. Phys.*, 2023, **25**, 1937–1946. Dynamics of self-propelled tracer particles inside a polymer network.

40 S. Saad and G. Natale, *Soft Matter*, 2019, **15**, 9909–9919. Diffusiophoresis of active colloids in viscoelastic media

41 W. R. Schneider and R. N. Doetsch, *J. Bacteriol.*, 1974, **117**, 696–701. Effect of viscosity on bacterial motility.

42 H. C. Berg and L. Turner, *Nature*, 1979, **278**, 349–351. Movement of microorganisms in viscous environments.

43 V. A. Martinez, J. Schwarz-Linek, M. Reufer, L. G. Wilson, A. N. Morozov, and W. C. K. Poon, *Proc. Natl. Acad. Sci. U.S.A.*, 2014, **111**, 17771–17776. Flagellated bacterial motility in polymer solutions.

44 Aranson, I. S. (2022). Bacterial active matter. Reports on Progress in Physics, 85(7), 076601.

45 J. R. Gomez-Solano, A. Blokhuis, and C. Bechinger, *Phys. Rev. Lett.*, 2016, **116**, 138301. Dynamics of self-propelled Janus particles in viscoelastic fluids.

46 B. Liebchen and D. Levis, *Europhys. Lett.*, 2022, **139**, 67001. Chiral active matter.

47 M. De Corato and P. Martínez-Lera, *Soft Matter*, 2025, **21**, 186–197. Enhanced rotational diffusion and spontaneous rotation of an active Janus disk in a complex fluid.

48 K. Saito, R. Kawano, C. Sadamatsu, Y. Iwashita, and Y. Kimura, *Phys. Rev. E*, 2025, **111**, 045409. Self-propelled motion of induced-charge electrophoretic Janus particles in viscoelastic fluids.

49 H. Raman, S. Das, H. Sharma, K. Singh, S. Gupta, and R. Mangal, *ACS Phys. Chem. Au*, 2023, **3**, 279–289. Dynamics of active SiO_2–Pt Janus colloids in dilute poly(ethylene oxide) solutions.

50 J. P. Banerjee, R. Mandal, D. S. Banerjee, S. Thutupalli, and M. Rao, *Nat. Commun.*, 2022, **13**, 4533. Unjamming and emergent nonreciprocity in active ploughing through a compressible viscoelastic fluid

51 J. Zhang, E. Luijten, B. A. Grzybowski, and S. Granick, *Chem. Soc. Rev.*, 2017, **46**, 5551–5569. Active colloids with collective mobility: status and research opportunities.

52 Massana-Cid, H., Meng, F., Matsunaga, D., Golestanian, R., & Tierno, P. (2019). Tunable self-healing of magnetically propelling colloidal carpets. Nature communications, 10(1), 2444.

53 C. van Baalen, W. E. Uspal, M. N. Popescu, and L. Isa, *Soft Matter*, 2023, **19**, 8790–8801. Transition from scattering to orbiting upon increasing the fuel concentration for an active Janus colloid moving at an obstacle–decorated interface.

54 T. Dhar and D. Saintillan, Sci. Rep., 2024, 14, 11844. Active transport of a passive colloid in a bath of run-and-tumble particles.

55 B. van der Meer, L. Filion, and M. Dijkstra, *Soft Matter*, 2016, **12**, 3406–3411. Fabricating large two-dimensional single colloidal crystals by doping with active particles.

56 L. Abbaspour, R. Mandal, P. Sollich, and S. Klumpp, *Commun. Phys.*, 2024, **7**, 289. Long-range velocity correlations from active dopants.

57 M. E. Szakasits, W. Zhang, and M. J. Solomon, *Phys. Rev. Lett.*, 2017, **119**, 058001. Dynamics of fractal cluster gels with embedded active colloids.

58 L. Hecht, I. Dong, and B. Liebchen, *Nat. Commun.*, 2024, **15**, 3206. Motility-induced coexistence of a hot liquid and a cold gas.

59 J. Stenhammar, R. Wittkowski, D. Marenduzzo, and M. E. Cates, *Phys. Rev. Lett.*, 2015, **114**, 018301. Activity-induced phase separation and self-assembly in mixtures of active and passive particles.

60 P. Dolai, A. Simha, and S. Mishra, *Soft Matter*, 2018, **14**, 6137–6145. Phase separation in binary mixtures of active and passive particles.

61 C. S. Dias, M. Trivedi, G. Volpe, N. A. Araújo, and G. Volpe, *Nat. Commun.*, 2023, **14**, 7324. Environmental memory boosts group formation of clueless individuals.

62 G. Jacucci, D. Breoni, S. Heijnen, J. Palomo, P. Jones, H. Löwen, G. Volpe, and S. Gigan, *Commun. Phys.*, 2024, **7**, 245. Patchy energy landscapes promote stability of small groups of active particles.

63 J. L. Aragones, J. P. Steimel and A. Alexander-Katz, Nat. Commun., 2016, 7, 11325. Elasticity-induced force reversal between active spinning particles in dense passive media.

64 J. P. Steimel, J. L. Aragones, H. Hu, N. Qureshi, and A. Alexander-Katz, *Proc. Natl. Acad. Sci. U.S.A.*, 2016, **113**, 4652–4657. Emergent ultra–long-range interactions between active particles in hybrid active–inactive systems.

65 C. Lozano, J. R. Gomez-Solano, and C. Bechinger, *Nat. Mater.*, 2019, **18**, 1118–1123. Active particles sense micromechanical properties of glasses.

66 C. Abaurrea-Velasco, C. Lozano, C. Bechinger, and J. de Graaf, *Phys. Rev. Lett.*, 2020, **125**, 258002. Autonomously probing viscoelasticity in disordered suspensions.

67 A. H. B. Dourado, Electrochem, 2022, 3, 789–808. Electric double layer: the good, the bad, and the beauty.

68 S.-J. Park and M.-K. Seo, Interface science and composites, Academic Press, 2011, vol. 18.

69 R. Burt, G. Birkett and X. S. Zhao, Phys. Chem. Chem. Phys., 2014, 16, 6519–6538. A review of molecular modelling of electric double layer capacitors.

70 P. Wette, H. J. Schöpe, and T. Palberg, *Colloids Surf. A*, 2003, **222**, 311–321. Experimental determination of effective charges in aqueous suspensions of colloidal spheres.

71 D. C. Henry, *Proc. R. Soc. Lond.*, 1931, **133**, 106–129. The cataphoresis of suspended particles.

72 R. J. Hunter, *Zeta Potential in Colloid Science: Principles and Applications*, Academic Press, London, 2013.

73 J. G. Lauth and J. Kowalczyk, *Einführung in die Physik und Chemie der Grenzflächen und Kolloide*, Springer Spektrum, Berlin, 2016.

74 A. Sharma and J. Y. Walz, *J. Chem. Soc., Faraday Trans.*, 1996, **92**, 4997–5004. Direct measurement of the depletion interaction in a charged colloidal dispersion.

75 V. Norn, *Emulsifiers in Food Technology*, 2014, pp. 1–20. Introduction to food emulsifiers and colloidal systems.

76 M. A. Hughes, *Coagulation and Flocculation*, Butterworths, 1981.

77 D. Ghernaout, A. I. Al-Ghonamy, A. Boucherit, B. Ghernaout, M. W. Naceur, N. A. Messaoudene, M. Aichouni, A. A. Mahjoubi, and N. A. Elboughdiri, *Am. J. Environ. Prot.*, 2015, **4**, 1–15. Brownian motion and coagulation process.

78 B. W. Ninham, *Adv. Colloid Interface Sci.*, 1999, **83**, 1–17. On progress in forces since the DLVO theory.

79 V. Sharma, Z. Xiao, and J. Simmchen, *Introduction to colloidal particles*, 2024.

80 A. Cavagna, *Phys. Rep.*, 2009, **476**, 51–124. Supercooled liquids for pedestrians.

81 W. C. K. Poon, P. N. Pusey, and H. N. W. Lekkerkerker, *Phys. World*, 1996, **9**, 27–34. Colloids in suspense.

82 T. Palberg, R. Simon, M. Würth, and P. Leiderer, in *Transitions in Oligomer and Polymer Systems*, Steinkopff, Darmstadt, 2007, pp. 62–71. Colloidal suspensions as model liquids and solids.

83 R. Beyer, M. Franke, H. J. Schöpe, E. Bartsch, and T. Palberg, *J. Chem. Phys.*, 2015, **143**, 064505. From nuclei to microstructure in colloidal crystallization: investigating intermediate length scales by small-angle laser light scattering.

84 V. Prasad, D. Semwogerere, and E. R. Weeks, *J. Phys.: Condens. Matter*, 2007, **19**, 113102. Confocal microscopy of colloids.

85 P. Laermann, H. Diamant, Y. Roichman, I. Buttinoni, M. A. Escobedo-Sánchez, and S. U. Egelhaaf, *Nat. Phys.*, 2026, 1–10. Emergent signatures of the glass transition in colloidal suspensions.

86 R. Cerbino, *Curr. Opin. Colloid Interface Sci.*, 2018, **34**, 47–58. Quantitative optical microscopy of colloids: the legacy of Jean Perrin.

87 P. Habdas and E. R. Weeks, *Curr. Opin. Colloid Interface Sci.*, 2002, **7**, 196–203. Video microscopy of colloidal suspensions and colloidal crystals.

88 F. Simon, L. E. Weiss, and S. van Teeffelen, *Nat. Rev. Methods Primers*, 2024, **4**, 66. A guide to single-particle tracking.

89 J. C. Crocker and D. G. Grier, *MRS Bull.*, 1998, **23**, 24–31. Interactions and dynamics in charge-stabilized colloids.

90 P. N. Pusey and W. van Megen, *Nature*, 1986, **320**, 340–342. Phase behaviour of concentrated suspensions of nearly hard colloidal spheres.

91 P. N. Pusey, E. Zaccarelli, C. Valeriani, E. Sanz, W. C. K. Poon, and M. E. Cates, *Phil. Trans. R. Soc. A*, 2009, **367**, 4993–5011. Hard spheres: crystallization and glass formation.

92 B. J. Alder and T. E. Wainwright, *J. Chem. Phys.*, 1957, **27**, 1208. Phase transition for a hard sphere system.

93 W. G. Hoover and F. H. Ree, *J. Chem. Phys.*, 1968, **49**, 3609–3617. Melting transition and communal entropy for hard spheres.

94 S.-C. Mau and D. A. Huse, Phys. Rev. E, 1999, 59, 4396. Stacking entropy of hard-sphere crystals.

95 S. Pronk and D. Frenkel, J. Chem. Phys., 1999, 110, 4589–4592. Can stacking faults in hard-sphere crystals anneal out spontaneously?

96 N. D. Mermin and H. Wagner, *Phys. Rev. Lett.*, 1966, **17**, 1133–1136. Absence of ferromagnetism or antiferromagnetism in one- or two-dimensional isotropic Heisenberg models.

97 K. J. Strandburg, *Rev. Mod. Phys.*, 1988, **60**, 161–207. Two-dimensional melting.

98 J. M. Kosterlitz and D. J. Thouless, *J. Phys. C: Solid State Phys.*, 1973, **6**, 1181–1203. Ordering, metastability and phase transitions in two-dimensional systems.

99 B. I. Halperin and D. R. Nelson, *Phys. Rev. Lett.*, 1978, **41**, 121–124. Theory of two-dimensional melting.

100 A. P. Young, *Phys. Rev. B*, 1979, **19**, 1855–1866. Melting and the vector Coulomb gas in two dimensions.

101 E. P. Bernard and W. Krauth, *Phys. Rev. Lett.*, 2011, **107**, 155704. Two-step melting in two dimensions: first-order liquid–hexatic transition.

102 S. T. Chui, *Phys. Rev. Lett.*, 1982, **48**, 933–937. Grain-boundary theory of melting in two dimensions.

103 N. W. Ashcroft and N. D. Mermin, *Solid State Physics*, Holt, Rinehart and Winston, New York, 1976.

104 A. Pal, M. A. Kamal, and V. A. Raghunathan, *Sci. Rep.*, 2016, **6**, 32313. Observation of the chiral and achiral hexatic phases of self-assembled micellar polymers.

105 M. A. Meyers, A. Mishra, and D. J. Benson, *Prog. Mater. Sci.*, 2006, **51**, 427–556. Mechanical properties of nanocrystalline materials.

106 Royall, C. Patrick, Patrick Charbonneau, Marjolein Dijkstra, John Russo, Frank Smallenburg, Thomas Speck, and Chantal Valeriani. "Colloidal hard spheres: Triumphs, challenges, and mysteries." Reviews of Modern Physics 96, no. 4 (2024): 045003.

107 E. M. Purcell, Physics and our world: reissue of the proceedings of a symposium in honor of Victor F. Weisskopf, 2014, 47–67. Life at low Reynolds number.

108 R. H. Davis and A. Acrivos, Annu. Rev. Fluid Mech., 1985, 17, 91–118. Sedimentation of noncolloidal particles at low Reynolds numbers.

109 J. L. Anderson, Annu. Rev. Fluid Mech., 1989, 21, 61–99. Colloid transport by interfacial forces.

110 A. J. C. Ladd, J. Chem. Phys., 1988, 88, 5051–5063. Hydrodynamic interactions in a suspension of spherical particles.

111 A. Reinmüller, H. J. Schöpe and T. Palberg, Langmuir, 2013, 29, 1738–1742. Self-organized cooperative swimming at low Reynolds numbers.

112 A. Einstein, *Ann. Phys.*, 1905, **17**, 549–560. Über die von der molekularkinetischen Theorie der Wärme geforderte Bewegung von in ruhenden Flüssigkeiten suspendierten Teilchen.

113 H. A. Lorentz, *Abhandlungen über theoretische Physik*, Vol. 2, Teubner, 1907.

114 J. N. Israelachvili, *Intermolecular and Surface Forces*, Academic Press, 2011.

115 L. P. Faucheux and A. J. Libchaber, *Phys. Rev. E*, 1994, **49**, 5158–5163. Confined Brownian motion.

116 G. Nägele, *Dynamics of dispersion colloids*, Lecture notes, International Research Training Group Soft Condensed Matter Physics of Model Systems, University of Konstanz, 2005.

117 G. Nägele, *Phys. Rep.*, 1996, **272**, 215–372. On the dynamics and structure of charge-stabilized suspensions.

118 J. Perrin, *Mouvement brownien et réalité moléculaire*, 1909, pp. 5–104.

119 R. Piazza, T. Bellini, and V. Degiorgio, *Phys. Rev. Lett.*, 1993, **71**, 4267–4270. Equilibrium sedimentation profiles of screened charged colloids: a test of the hard-sphere equation of state.

120 J. C. Crocker and D. G. Grier, *J. Colloid Interface Sci.*, 1996, **179**, 298–310. Methods of digital video microscopy for colloidal studies.

121 M. Mittal, P. P. Lele, E. W. Kaler, and E. M. Furst, *J. Chem. Phys.*, 2008, **129**, 064513. Polarization and interactions of colloidal particles in AC electric fields.

122 C. T. O'Konski, *J. Phys. Chem.*, 1960, **64**, 605–619. Electric properties of macromolecules. V. Theory of ionic polarization in polyelectrolytes.

123 R. W. O'Brien, *J. Colloid Interface Sci.*, 1986, **113**, 81–93. The high-frequency dielectric dispersion of a colloid.

124 T. B. Jones, *Electromechanics of Particles*, Cambridge University Press, Cambridge, 1995, pp. 227–230.

125 D. A. Saville, T. Bellini, V. Degiorgio, and F. Mantegazza, *J. Chem. Phys.*, 2000, **113**, 6974–6983. An extended Maxwell–Wagner theory for the electric birefringence of charged colloids.

126 S. S. Dukhin, V. N. Shilov, and J. J. Bikerman, J. Electrochem. Soc., 1974, 121, 154C–160C. Dielectric phenomena and double layer in disperse systems and polyelectrolytes.

127 W. B. Russel, D. A. Saville, and W. R. Schowalter, Colloidal Dispersions, Cambridge University Press, Cambridge, 1991.

128 H. Zhao, Electrophoresis, 2011, 32, 2232–2244. Double-layer polarization of a non-conducting particle in an alternating current field with applications to dielectrophoresis.

129 M. Parthasarathy and D. J. Klingenberg, Mater. Sci. Eng. R, 1996, 17, 57–103. Electrorheology: mechanisms and models.

130 A. Yethiraj, Soft Matter, 2007, 3, 1099–1115. Tunable colloids: control of colloidal phase transitions with tunable interactions.

131 R. Tao and Q. Jiang, Phys. Rev. Lett., 1994, 73, 205–208. Simulation of structure formation in an electrorheological fluid.

132 M. M. Panczyk, J.-G. Park, N. J. Wagner, and E. M. Furst, Langmuir, 2013, 29, 75–81. Two-dimensional directed assembly of dicolloids.

133 K. Chaudhary, J. J. Juárez, Q. Chen, S. Granick, and J. A. Lewis, *Soft Matter*, 2014, **10**, 1320–1324. Reconfigurable assemblies of Janus rods in AC electric fields.

134 H. R. Vutukuri, A. F. Demirörs, B. Peng, P. D. J. van Oostrum, A. Imhof, and A. van Blaaderen, *Angew. Chem. Int. Ed.*, 2012, **51**, 11249–11253. Colloidal analogues of charged and uncharged polymer chains with tunable stiffness.

135 A. Yethiraj and A. van Blaaderen, *Nature*, 2003, **421**, 513–517. A colloidal model system with an interaction tunable from hard sphere to soft and dipolar.

136 S. O. Lumsdon, E. W. Kaler, J. P. Williams, and O. D. Velev, *Appl. Phys. Lett.*, 2003, **82**, 949–951. Dielectrophoretic assembly of oriented and switchable two-dimensional photonic crystals.

137 M. Grzelczak, J. Vermant, E. M. Furst, and L. M. Liz-Marzán, *ACS Nano*, 2010, **4**, 3591–3605. Directed self-assembly of nanoparticles.

138 T. Gong, D. T. Wu, and D. W. M. Marr, *Langmuir*, 2002, **18**, 10064–10067. Two-dimensional electrohydrodynamically induced colloidal phases.

139 W. D. Ristenpart, I. A. Aksay, and D. A. Saville, *Phys. Rev. Lett.*, 2003, **90**, 128303. Electrically guided assembly of planar superlattices in binary colloidal suspensions.

140 J. P. Huang, M. Karttunen, K. W. Yu and L. Dong, Phys. Rev. E, 2003, 67, 021403. Dielectrophoresis of charged colloidal suspensions.

141 R. Pethig, J. Electrochem. Soc., 2017, 164, B3049–B3055. Where is dielectrophoresis (DEP) going?

142 B. Sarno, D. Heineck, M. J. Heller and S. D. Ibsen, Electrophoresis, 2021, 42, 539–564. Dielectrophoresis: Developments and applications from 2010 to 2020.

143 Y. Demircan, E. Özgür and H. Külah, Electrophoresis, 2013, 34, 1008–1027. Dielectrophoresis: Applications and future outlook in point of care.

144 T. Honegger, K. Berton, E. Picard and D. Peyrade, Appl. Phys. Lett., 2011, 98, 181906. Determination of Clausius–Mossotti factors and surface capacitances for colloidal particles.

145 A. Jain, B. Dünweg, and J. R. Prakash, *Phys. Rev. Lett.*, 2012, **109**, 088302. Dynamic crossover scaling in polymer solutions.

146 R. P. Chhabra, in *Rheology of Complex Fluids*, Springer, New York, 2010, pp. 3–34. Non-Newtonian fluids: an introduction.

147 A. B. Metzner, R. H. Feehs, H. L. Ramos, R. E. Otto, and J. D. Tuthill, *AIChE J.*, 1961, **7**, 3–9. Agitation of viscous Newtonian and non-Newtonian fluids.

148 J. L. Moran and J. D. Posner, Annu. Rev. Fluid Mech., 2017, 49, 511–540. Phoretic self-propulsion.

149 R. Golestanian, T. B. Liverpool, and A. Ajdari, *Phys. Rev. Lett.*, 2005, **94**, 220801. Propulsion of a molecular machine by asymmetric distribution of reaction products.

150 W. F. Paxton, K. C. Kistler, C. C. Olmeda, A. Sen, S. K. St. Angelo, Y. Cao, T. E. Mallouk, P. E. Lammert, and V. H. Crespi, *J. Am. Chem. Soc.*, 2004, **126**, 13424–13431. Catalytic nanomotors: autonomous movement of striped nanorods.

151 S. Fournier-Bidoz, A. C. Arsenault, I. Manners, and G. A. Ozin, *Chem. Commun.*, 2005, 441–443. Synthetic self-propelled nanorotors.

152 P. M. Wheat, N. A. Marine, J. L. Moran, and J. D. Posner, *Langmuir*, 2010, **26**, 13052–13055. Rapid fabrication of bimetallic spherical motors.

153 Y. Wang, R. M. Hernandez, D. J. Bartlett, J. M. Bingham, T. R. Kline, A. Sen, and T. E. Mallouk, *Langmuir*, 2006, **22**, 10451–10456. Bipolar electrochemical mechanism for the propulsion of catalytic nanomotors in hydrogen peroxide solutions.

154 T. Liu, L. Xie, C. A. H. Price, J. Liu, Q. He, and B. Kong, *Chem. Soc. Rev.*, 2022, **51**, 10083–10119. Controlled propulsion of micro/nanomotors: operational mechanisms, motion manipulation and potential biomedical applications.

155 J. L. Moran and J. D. Posner, *J. Fluid Mech.*, 2011, **680**, 31–66. Electrokinetic locomotion due to reaction-induced charge auto-electrophoresis.

156 W. F. Paxton, P. T. Baker, T. R. Kline, Y. Wang, T. E. Mallouk, and A. Sen, *J. Am. Chem. Soc.*, 2006, **128**, 14881–14888. Catalytically induced electrokinetics for motors and micropumps.

157 W. F. Paxton, A. Sen, and T. E. Mallouk, *Chem. Eur. J.*, 2005, **11**, 6462–6470. Motility of catalytic nanoparticles through self-generated forces.

158 R. Niu and T. Palberg, *Soft Matter*, 2018, **14**, 7554–7568. Modular approach to microswimming.

159 B. Jang, W. Wang, S. Wiget, A. J. Petruska, X. Chen, C. Hu, A. Hong *et al.*, *ACS Nano*, 2016, **10**, 9983–9991. Catalytic locomotion of core–shell nanowire motors.

160 M. J. Esplandiu, K. Zhang, J. Fraxedas, B. Sepúlveda, and D. Reguera, *Acc. Chem. Res.*, 2018, **51**, 1921–1930. Unraveling the operational mechanisms of chemically propelled motors with micropumps.

161 W. Gao, A. Pei, R. Dong, and J. Wang, *J. Am. Chem. Soc.*, 2014, **136**, 2276–2279. Catalytic iridium-based Janus micromotors powered by ultralow levels of chemical fuels.

162 X. Shi, S. Back, T. M. Gill, S. Siahrostami, and X. Zheng, *Chem*, 2021, **7**, 38–63. Electrochemical synthesis of H_2O_2 by two-electron water oxidation reaction.

163 A. B. Laursen, I. C. Man, O. L. Trinhammer, J. Rossmeisl, and S. Dahl, *J. Chem. Educ.*, 2011, **88**, 1711–1715. The Sabatier principle illustrated by catalytic H_2O_2 decomposition on metal surfaces.

164 J. R. Howse, R. A. L. Jones, A. J. Ryan, T. Gough, R. Vafabakhsh, and R. Golestanian, *Phys. Rev. Lett.*, 2007, **99**, 048102. Self-motile colloidal particles: from directed propulsion to random walk.

165 J. P. Ebel, J. L. Anderson, and D. C. Prieve, *Langmuir*, 1988, **4**, 396–406. Diffusiophoresis of latex particles in electrolyte gradients.

166 A. I. Campbell, S. J. Ebbens, P. Illien, and R. Golestanian, Nat. Commun., 2019, 10, 3952. *Experimental observation of flow fields around active Janus spheres.*

167 J. Palacci, S. Sacanna, A. P. Steinberg, D. J. Pine, and P. M. Chaikin, *Science*, 2013, **339**, 936–940. Living crystals of light-activated colloidal surfers.

168 J. Palacci, S. Sacanna, S.-H. Kim, G.-R. Yi, D. J. Pine, and P. M. Chaikin, *Phil. Trans. R. Soc. A*, 2014, **372**, 20130372. Light-activated self-propelled colloids.

169 D. P. Singh, U. Choudhury, P. Fischer, and A. G. Mark, *Adv. Mater.*, 2017, **29**, 1701328. Non-equilibrium assembly of light-activated colloidal mixtures.

170 S. Ebbens, J. Howse, R. Archer, D. Gregory, A. Campbell, and G. Dunderdale, in *Soft, Hard, and Hybrid Janus Structures: Synthesis, Self-Assembly, and Applications*, 2018, pp. 315–403. Catalytic Janus swimmers.

171 S. Wang and N. Wu, *Langmuir*, 2014, **30**, 3477–3486. Selecting the swimming mechanisms of colloidal particles: bubble propulsion versus self-diffusiophoresis.

172 G. Volpe, I. Buttinoni, D. Vogt, H.-J. Kümmerer, and C. Bechinger, *Soft Matter*, 2011, **7**, 8810–8815. Microswimmers in patterned environments.

173 I. Buttinoni, G. Volpe, F. Kümmel, G. Volpe, and C. Bechinger, *J. Phys.: Condens. Matter*, 2012, **24**, 284129. Active Brownian motion tunable by light.

174 H.-R. Jiang, N. Yoshinaga, and M. Sano, *Phys. Rev. Lett.*, 2010, **105**, 268302. Active motion of a Janus particle by self-thermophoresis in a defocused laser beam.

175 W. Wang, X. Lv, J. L. Moran, S. Duan, and C. Zhou, Soft Matter, 2020, 16, 3846–3868. *A practical guide to active colloids: choosing synthetic model systems for soft matter physics research*

176 G. Quincke, *Ann. Phys.*, 1896, **295**, 417–486. Ueber rotationen im constanten electrischen felde.

177 A. Bricard, J.-B. Caussin, N. Desreumaux, O. Dauchot, and D. Bartolo, *Nature*, 2013, **503**, 95–98. Emergence of macroscopic directed motion in populations of motile colloids.

178 A. Bricard, J.-B. Caussin, D. Das, C. Savoie, V. Chikkadi, K. Shitara, O. Chepizhko, F. Peruani, D. Saintillan, and D. Bartolo, *Nat. Commun.*, 2015, **6**, 7470. Emergent vortices in populations of colloidal rollers.

179 G. E. Pradillo, H. Karani, and P. M. Vlahovska, Soft Matter, 2019, 15, 6564–6570. *Quincke rotor dynamics in confinement: rolling and hovering*

180 D. Geyer, D. Martin, J. Tailleur, and D. Bartolo, *Phys. Rev. X*, 2019, **9**, 031043. Freezing a flock: motility-induced phase separation in polar active liquids.

181 D. Geyer, A. Morin, and D. Bartolo, *Nat. Mater.*, 2018, **17**, 789–793. Sounds and hydrodynamics of polar active fluids.

182 A. Ramos, H. Morgan, N. G. Green, and A. Castellanos, *J. Phys. D: Appl. Phys.*, 1998, **31**, 2338–2353. AC electrokinetics: a review of forces in microelectrode structures.

183 N. G. Green, A. Ramos, A. González, H. Morgan, and A. Castellanos, *Phys. Rev. E*, 2000, **61**, 4011–4018. Fluid flow induced by nonuniform AC electric fields in electrolytes on microelectrodes. I. Experimental measurements.

184 T. M. Squires and M. Z. Bazant, *J. Fluid Mech.*, 2004, **509**, 217–252. Induced-charge electro-osmosis.

185 M. Z. Bazant and T. M. Squires, *Phys. Rev. Lett.*, 2004, **92**, 066101. Induced-charge electrokinetic phenomena: theory and microfluidic applications.

186 S. Gangwal, O. J. Cayre, M. Z. Bazant, and O. D. Velev, *Phys. Rev. Lett.*, 2008, **100**, 058302. Induced-charge electrophoresis of metallodielectric particles.

187 A. M. Boymelgreen and T. Miloh, Electrophoresis, 2012, 33, 870–879. Induced-charge electrophoresis of uncharged dielectric spherical Janus particles.

188 A. Boymelgreen, G. Yossifon and T. Miloh, 2016. Propulsion of Active Colloids by Self-Induced Field Gradients.

189 N. M. Diwakar, G. Kunti, T. Miloh, G. Yossifon and O. D. Velev, Curr. Opin. Colloid Interface Sci., 2022, 59, 101586. AC electrohydrodynamic propulsion and rotation of active particles of engineered shape and asymmetry.

190 A. E. Patteson, A. Gopinath, M. Goulian, and P. E. Arratia, *Sci. Rep.*, 2015, **5**, 15761. Running and tumbling with *E. coli* in polymeric solutions.

191 P. Chatterjee, E. M. Tang, P. Karande, and P. T. Underhill, *Phys. Rev. Fluids*, 2018, **3**, 014101. Propulsion of catalytic Janus spheres in viscosified Newtonian solutions.

192 N. Narinder, C. Bechinger, and J. R. Gomez-Solano, *Phys. Rev. Lett.*, 2018, **121**, 078003. Memory-induced transition from a persistent random walk to circular motion for achiral microswimmers.

193 F. Kümmel, P. Shabestari, C. Lozano, G. Volpe, and C. Bechinger, *Soft Matter*, 2015, **11**, 6187–6191. Formation, compression and surface melting of colloidal clusters by active particles.

194 S. Ramananarivo, E. Ducrot, and J. Palacci, *Nat. Commun.*, 2019, **10**, 3380. Activity-controlled annealing of colloidal monolayers.

195 K. Dietrich, G. Volpe, M. N. Sulaiman, D. Renggli, I. Buttinoni, and L. Isa, *Phys. Rev. Lett.*, 2018, **120**, 268004. Active atoms and interstitials in two-dimensional colloidal crystals.

196 C. S. Dias, M. Trivedi, G. Volpe, N. A. M. Araújo, and G. Volpe, *Nat. Commun.*, 2023, **14**, 7324. Environmental memory boosts group formation of clueless individuals.

197 Z. Wang, Z. Wang, J. Li, C. Tian and Y. Wang, Nat. Commun., 2020, 11, 2670. Active colloidal molecules assembled via selective and directional bonds.

198 W. Gao, A. Pei, X. Feng, C. Hennessy, and J. Wang, *J. Am. Chem. Soc.*, 2013, **135**, 998–1001. Organized self-assembly of Janus micromotors with hydrophobic hemispheres.

199 A. F. Demirörs, M. T. Akan, E. Poloni, and A. R. Studart, *Soft Matter*, 2018, **14**, 4741–4749. Active cargo transport with Janus colloidal shuttles using electric and magnetic fields.

200 P. Richetti, J. Prost and P. Barois, J. Phys. Lett., 1984, 45, 1137–1143. Two-dimensional aggregation and crystallization of a colloidal suspension of latex spheres.

201 W. D. Ristenpart, I. A. Aksay and D. A. Saville, Phys. Rev. Lett., 2003, 90, 128303. Electrically guided assembly of planar superlattices in binary colloidal suspensions.

202 M. Trau, D. A. Saville and I. A. Aksay, Science, 1996, 272, 706–709. Field-induced layering of colloidal crystals.

203 T. Gong and D. W. M. Marr, Langmuir, 2001, 17, 2301–2304. Electrically switchable colloidal ordering in confined geometries.

204 Trackpy, *Trackpy v0.5.0*, available at: http://soft-matter.github.io/trackpy/v0.5.0/

205 G. Bradski, Dr. Dobb's J. Softw. Tools, 2000, 25, 120–125. The OpenCV Library. available at: https://opencv.org/

206 X. Wang, M. In, C. Blanc, M. Nobili and A. Stocco, Soft Matter, 2015, 11, 7376–7384. Enhanced active motion of Janus colloids at the water surface.

207 A. E. Stones, R. P. A. Dullens, and D. G. A. L. Aarts, Phys. Rev. Lett., 2019, 123, 098002. *Model-free measurement of the pair potential in colloidal fluids using optical microscopy.*

208 I. Buttinoni, M. Steinacher, H. T. Spanke, J. Pokki, S. Bahmann, B. Nelson, G. Foffi, and L. Isa, Phys. Rev. E, 2017, 95, 012610. *Colloidal polycrystalline monolayers under oscillatory shear.*

209 A. L. Thorneywork, J. L. Abbott, D. G. A. L. Aarts, and R. P. A. Dullens, Phys. Rev. Lett., 2017, 118, 158001. *Two-dimensional melting of colloidal hard spheres.*

210 A. M. Boymelgreen and T. Miloh, Phys. Fluids, 2011, 23, 072004. A theoretical study of induced-charge dipolophoresis of ideally polarizable asymmetrically slipping Janus particles.

211 A. Boymelgreen and G. Yossifon, *Langmuir*, 2015, **31**, 8243–8250. Observing electrokinetic Janus particle channel wall interaction using microparticle image velocimetry.

212 S. Hou, N. Ziebacz, T. Kalwarczyk, T. S. Kaminski, S. A. Wieczorek and R. Holyst, Soft Matter, 2011, 7, 3092–3099. Influence of nano-viscosity and depletion interactions on cleavage of DNA by enzymes in glycerol and poly(ethylene glycol) solutions: qualitative analysis.

213 N. M. Diwakar, G. Kunti, T. Miloh, G. Yossifon, and O. D. Velev, *Curr. Opin. Colloid Interface Sci.*, 2022, **59**, 101586. AC electrohydrodynamic propulsion and rotation of active particles of engineered shape and asymmetry.

214 S. K. Panda, S. Debata, and D. P. Singh, *Chem. Phys. Impact*, 2024, **8**, 100588. Characterizing Janus colloidal particles in AC electric field and a step towards label-free cargo manipulation.

215 J. L. Anderson, *Annu. Rev. Fluid Mech.*, 1989, **21**, 61–99. Colloid transport by interfacial forces.

216 S. S. Dukhin, *Adv. Colloid Interface Sci.*, 1993, **44**, 1–134. Non-equilibrium electric surface phenomena.

217 W. D. Ristenpart, O. Vincent, S. Lecuyer, and H. A. Stone, *Langmuir*, 2010, **26**, 9429–9436. Dynamic angular segregation of vesicles in electrohydrodynamic flows.

218 N. G. Green, A. Ramos, A. González, H. Morgan, and A. Castellanos, *Phys. Rev. E*, 2000, **61**, 4011–4018. Fluid flow induced by nonuniform AC electric fields in electrolytes on microelectrodes. I. Experimental measurements.

219 K. Schaar, A. Zöttl, and H. Stark, Phys. Rev. Lett., 2015, 115, 038101. Detention times of microswimmers close to surfaces: influence of hydrodynamic interactions and noise.

220 A. P. Solon, M. E. Cates, and J. Tailleur, Eur. Phys. J. Spec. Top., 2015, 224, 1231–1262. *Active Brownian particles and run-and-tumble particles: a comparative study.*

221 C. Lozano, J. R. Gomez-Solano and C. Bechinger, Nat. Mater., 2019, 18, 1118–1123. Active particles sense micromechanical properties of glasses.

222 C. Abaurrea-Velasco, C. Lozano, C. Bechinger and J. de Graaf, Phys. Rev. Lett., 2020, 125, 258002. Autonomously probing viscoelasticity in disordered suspensions.

223 F. Kümmel, B. ten Hagen, R. Wittkowski **et al.**, Phys. Rev. Lett., 2013, 110, 198302. Circular motion of asymmetric self-propelling particles.

224 M. De Corato and P. Martínez-Lera, Soft Matter, 2025, 21, 186–197. Enhanced rotational diffusion and spontaneous rotation of an active Janus disk in a complex fluid.

225 M. De Corato, I. Pagonabarraga and G. Natale, Phys. Rev. E, 2021, 104, 044607. Spontaneous chiralization of polar active particles.